

A NUMERICAL SOLUTION FOR THE FLOW
FIELD SURROUNDING A SUPERSONIC
CONE AT AN ANGLE OF ATTACK

By

JOHN JOSEPH PRENTICE

Bachelor of Aeronautical Engineering
University of Minnesota
Minneapolis, Minnesota
1956

Master of Science
Air Force Institute of Technology
Wright-Patterson AFB, Ohio
1961

Submitted to the Faculty of the Graduate College
of the Oklahoma State University
in partial fulfillment of the requirements
for the Degree of
DOCTOR OF PHILOSOPHY
May, 1971

OKLAHOMA
STATE UNIVERSITY
LIBRARY
AUG 12 1971

A NUMERICAL SOLUTION FOR THE FLOW
FIELD SURROUNDING A SUPERSONIC
CONE AT AN ANGLE OF ATTACK

Thesis Approved:

Ladislav J. Fila

Thesis Adviser

W. B. Brooks

J. A. Wheelert

J. Paul C. McCallum

D. D. Durham

Dean of the Graduate College

788728

PREFACE

A study was undertaken in which the flow properties about a cone at an angle of attack were approximated for four representative angles of attack and at a single supersonic freestream Mach number.

This work was begun under the sponsorship of the Sandia Corporation, Albuquerque, New Mexico, and concluded with the assistance of the Air Force Weapons Laboratory, Kirtland AFB, New Mexico. The work represents an element of a program of developing the capability to predict the behavior of a re-entry vehicle when it encounters a blast wave. Four numerical studies preceded this effort. Dr. L. D. Tyler investigated the propagation of plane shock waves emerging into both still and supersonic transverse streams. Dr. W. N. Jackomis studied the transient flow field resulting from the interaction of a moving blast wave with a stationary cone; Dr. W. F. Walker developed a technique for the study of the interaction of a moving shock and a turbulent mixing region; and Dr. R. R. Eaton investigated the flow field surrounding a cone-cylinder when entering and leaving a blast sphere diametrically. Dr. R. J. Damkevala developed an experimental technique for studying the interaction between a supersonic body and an obliquely approaching shock wave.

My sincere appreciation is tendered to the following individuals: Dr. G. W. Zumwalt, who served as my major thesis adviser and graduate committee chairman until his departure from Oklahoma State University: His encouragement, guidance, and patience were invaluable to me during

my study; Professor L. J. Fila, who also served as thesis adviser: Professor Fila's availability for comment and discussion was of tremendous assistance to me during my course of graduate study; Dr. J. A. Wiebelt, my graduate committee chairman during the final year of my course of study; Dr. W. D. Grosvenor, Dr. W. B. Brooks, Dr. P. A. McCollum for serving on my graduate committee.

I would also like to thank the Sandia Corporation and Colonel R. W. Rowden, of the Air Force Weapons Laboratory, for their financial assistance. The computer time they made available to me was a prerequisite to the completion of this study. Finally, I wish to thank Mrs. Esther Caster, for her typing assistance; and Miss Velda Davis and Mrs. Marilyn Bond, for the final preparation and handling the submission of this thesis, and my wife Loretta for suffering through these years with a part-time husband.

TABLE OF CONTENTS

Chapter	Page
I. INTRODUCTION.	1
II. LITERATURE SURVEY	3
III. DEVELOPMENT OF FINITE-DIFFERENCE TECHNIQUES	6
Applicable Differential Equations.	6
Non-Dimensionalizing the Dependent Variables	8
Finite-Difference Representation of the Differential Equations.	10
IV. BOUNDARY INVESTIGATION.	20
Axis of Field.	21
Stagnation Point	24
Cone Surface	26
Cone Base.	29
Upstream Field Boundary.	30
Downstream Field Boundary.	31
Outer Field Boundary	31
Plane of Symmetry.	33
V. RESULTS	34
Zero Angle of Attack Solution.	35
NonZero Angle of Attack Solutions.	43
VI. COMPARISON OF RESULTS WITH THEORY AND EXPERIMENT.	81
Stagnation Point Pressures	81
Cone Surface Pressure Distribution	82
Shock Wave Position and Downstream Pressures	86
VII. CONCLUSIONS AND RECOMMENDATIONS	89
Conclusions.	89
Recommendations.	90
A SELECTED BIBLIOGRAPHY.	91

LIST OF TABLES

Table	Page
I. Relation Between Variables in Cylindrical and Cartesian Coordinates.	25
II. Comparison of Stagnation Point Pressures	81

List of Figures

Figure	Page
1. Relationship of Mesh Points to Field and Body Boundaries . .	13
2. Nomenclature for an r-z Plane of Mesh Points	14
3. Nomenclature for an r- θ Plane of Mesh Points	14
4. Exterior View of Flow Field	20
5. Interior View of A Plane of Mesh Points Showing All Boundaries	21
6. Mesh Point Arrangement for Off-Axis Technique	24
7. Blunt-Nose Configuration	26
8. Mesh Point Configuration in Base Corner Region	27
9. Cone Base Corner Configuration	31
10. Windward/Leeward Velocity Vector Map, $M_\infty = 3.0$, $\alpha = 0^\circ$. . .	36
11. Windward/Leeward Velocity Vector Map, $M_\infty = 3.0$, $\alpha = 0^\circ$. . .	37
12. Windward/Leeward Velocity Vector Map, $M_\infty = 3.0$, $\alpha = 0^\circ$. . .	38
13. Wave Position from Velocity Map Microfilm, $\alpha = 0^\circ$	39
14. Pressure Profiles, $M_\infty = 3.0$, $\alpha = 0^\circ$	40
15. Pressure Profiles, $M_\infty = 3.0$, $\alpha = 0^\circ$	41
16. Pressure Profiles, $M_\infty = 3.0$, $\alpha = 0^\circ$	42
17. Windward/Leeward Velocity Vector Map, $M_\infty = 3.0$, $\alpha = 10^\circ$. .	44
18. Windward/Leeward Velocity Vector Map, $M_\infty = 3.0$, $\alpha = 10^\circ$. .	46
19. Windward/Leeward Velocity Vector Map, $M_\infty = 3.0$, $\alpha = 10^\circ$. .	47
20. Transverse Velocity Vector Map, $M = 3.0$, $\alpha = 10^\circ$, $m = 10$ (Midway on Cone Axis)	48

Figure	Page
21. Transverse Velocity Vector Map, $M = 3.0$, $\alpha = 10^\circ$, $m = 10$ (Midway on Cone Axis)	49
22. Transverse Velocity Vector Map, $M = 3.0$, $\alpha = 10^\circ$, $m = 10$ (Midway on Cone Axis)	50
23. Pressure Profiles, $M_\infty = 3.0$, $\alpha = 10^\circ$, $\theta = 0^\circ, 180^\circ$	51
24. Pressure Profiles, $M_\infty = 3.0$, $\alpha = 10^\circ$, $\theta = 90^\circ$	52
25. Pressure Profiles, $M_\infty = 3.0$, $\alpha = 10^\circ$, $\theta = 0^\circ, 180^\circ$	53
26. Pressure Profiles, $M_\infty = 3.0$, $\alpha = 10^\circ$, $\theta = 90^\circ$	54
27. Pressure Profiles, $M_\infty = 3.0$, $\alpha = 10^\circ$, $\theta = 0^\circ, 180^\circ$	55
28. Pressure Profiles, $M_\infty = 3.0$, $\alpha = 10^\circ$, $\theta = 90^\circ$	56
29. Windward/Leeward Velocity Vector Map, $M_\infty = 3.0$, $\alpha = 20^\circ$. .	57
30. Windward/Leeward Velocity Vector Map, $M_\infty = 3.0$, $\alpha = 20^\circ$. .	58
31. Windward/Leeward Velocity Vector Map, $M_\infty = 3.0$, $\alpha = 20^\circ$. .	59
32. Transverse Velocity Vector Map, $M = 3.0$, $\alpha = 20^\circ$, $m = 10$ (Midway on Cone Axis)	60
33. Transverse Velocity Vector Map, $M = 3.0$, $\alpha = 20^\circ$, $m = 10$ (Midway on Cone Axis)	61
34. Transverse Velocity Vector Map, $M = 3.0$, $\alpha = 20^\circ$, $m = 10$ (Midway on Cone Axis)	62
35. Pressure Profiles, $M_\infty = 3.0$, $\alpha = 20^\circ$, $\theta = 0^\circ, 180^\circ$	63
36. Pressure Profiles, $M_\infty = 3.0$, $\alpha = 20^\circ$, $\theta = 90^\circ$	64
37. Pressure Profiles, $M_\infty = 3.0$, $\alpha = 20^\circ$, $\theta = 0^\circ, 180^\circ$	65
38. Pressure Profiles, $M_\infty = 3.0$, $\alpha = 20^\circ$, $\theta = 0^\circ, 180^\circ$	66
39. Pressure Profiles, $M_\infty = 3.0$, $\alpha = 20^\circ$, $\theta = 0^\circ, 180^\circ$	67
40. Pressure Profiles, $M_\infty = 3.0$, $\alpha = 20^\circ$, $\theta = 90^\circ$	68
41. Windward/Leeward Velocity Vector Map, $M_\infty = 3.0$, $\alpha = 30^\circ$. .	69
42. Windward/Leeward Velocity Vector Map, $M_\infty = 3.0$, $\alpha = 30^\circ$. .	70
43. Windward/Leeward Velocity Vector Map, $M_\infty = 3.0$, $\alpha = 30^\circ$. .	71

Figure	Page
44. Transverse Velocity Vector Map, $M = 3.0$, $\alpha = 30^\circ$, $m = 10$ (Midway on Cone Axis)	72
45. Transverse Velocity Vector Map, $M = 3.0$, $\alpha = 30^\circ$, $m = 10$ (Midway on Cone Axis)	73
46. Transverse Velocity Vector Map, $M = 3.0$, $\alpha = 30^\circ$, $m = 10$ (Midway on Cone Axis)	74
47. Pressure Profiles, $M_\infty = 3.0$, $\alpha = 30^\circ$, $\theta = 0^\circ, 180^\circ$	75
48. Pressure Profiles, $M_\infty = 3.0$, $\alpha = 30^\circ$, $\theta = 90^\circ$	76
49. Pressure Profiles, $M_\infty = 3.0$, $\alpha = 30^\circ$, $\theta = 0^\circ, 180^\circ$	77
50. Pressure Profiles, $M_\infty = 3.0$, $\alpha = 30^\circ$, $\theta = 90^\circ$	78
51. Pressure Profiles, $M_\infty = 3.0$, $\alpha = 30^\circ$, $\theta = 0^\circ, 180^\circ$	79
52. Pressure Profiles, $M_\infty = 3.0$, $\alpha = 30^\circ$, $\theta = 90^\circ$	80
53. Cone Surface Pressure Distribution, $M_\infty = 3.0$, $\alpha = 0^\circ$	83
54. Cone Surface Pressure Distribution, Windward/Leeward Plane, $M_\infty = 3.0$, $\alpha = 10^\circ$	84
55. Cone Surface Pressure Distribution, Windward/Leeward Plane, $M_\infty = 3.0$, $\alpha = 20^\circ$	85
56. Comparison Between Computed Pressure Profiles and Theoretical Shock Wave Position and Downstream Pressure, $\alpha = 0^\circ$	87
57. Comparison Between Computed Pressure Profiles and Theoretical Shock Wave Position and Downstream Pressure, $\alpha = 10^\circ$	88

NOMENCLATURE

A	blurring term coefficient for axial direction
B	blurring term coefficient for radial direction
C	blurring term coefficient for angular direction
e	fluid energy per unit volume
F	space sensitive function
f	space sensitive function
H	characteristic length
h	diagonal of finite mesh
K	specific heat ratio 1.4
k	mesh number in θ -coordinate direction
ℓ	mesh number in r-coordinate direction
m	mesh number in Z-coordinate direction
n	time plane number
p	static pressure
r	coordinate perpendicular to cone axis
t	time
u	velocity in axial (x) direction in Cartesian system
\bar{V}	total velocity vector
V	velocity component in a coordinate direction
v	velocity in y-direction in Cartesian system
w	velocity in z-direction in Cartesian system
Z	coordinate coinciding with cone axis (cylindrical)
z	coordinate coinciding with cone axis (Cartesian)

$[\overline{\mathbf{V}} \overline{\mathbf{V}}]$	dyadic product
α	coefficient of a dissipative difference term
β	coefficient of a dissipative difference term
γ	coefficient of a dissipative difference term
θ	angular coordinate in cylindrical system
ρ	density
τ	time increment
φ	cone half angle
ψ	defined on page 11
$\overline{\nabla}$	del operator

Superscripts

'	denotes a dimensionless variable
n	time plane number
r	denotes a variable varying with r
x	denotes a variable varying with x
y	denotes a variable varying with y
z	denotes a variable varying with z
Z	denotes a variable varying with Z
θ	denotes a variable varying with θ

Subscripts

k	θ mesh point location
ℓ	r mesh point location
m	Z mesh point location
r	radial component of a variable
Z	axial component of a variable

θ angular component of a variable

∞ free stream variable value

CHAPTER I

INTRODUCTION

The aerodynamic and structural design of aerospace vehicles, particularly re-entry shapes, requires the availability of three-dimensional flow field data for the configuration in design. The designer of such high speed aerospace vehicles must be able to determine the surface flow property values, which influence his design, for steady-state supersonic flight and for the transient case when the vehicle is perturbed by the large overpressures and gust loads imposed by blast waves of nearby nuclear detonations.

This study provides the designer with a technique for determining the steady-state flow conditions around a proposed design. In addition, the techniques of this study can be used as a basis for the solution of the transient problem, requiring only the insertion of routines for superposition of blast waves over the steady-state solution.

The method put forward in this study represents an extension of the technique developed by V. V. Rusanov (26). The Rusanov technique employs a finite difference solution of the quasi-linear partial differential flow equations which makes use of a mathematical "viscosity". The "viscosity," or blurring term, allows the calculational scheme to proceed through discontinuities like shock waves by treating them as steep gradients. This technique has been applied to other aspects of the over-all problem of flow field determination. Tyler (30) applied

it to a shock propagating through a cross flow; Jackomis (15) described the axisymmetric flow in the wake of a cone by the same technique; Walker (32) used it to describe a turbulent mixing region; and Eaton (13) employed it to determine the flow field in the neighborhood of a cone-cylinder when entering and leaving a blast sphere diametrically.

This study was undertaken to determine the feasibility of using a Rusanov based technique for the determination of a three-dimensional flow field in the neighborhood of a cone. Four angles of attack solutions were generated; 0, 10, 20, and 30 degrees.

CHAPTER II

LITERATURE SURVEY

The analysis of the aerodynamic behavior of a re-entry vehicle when in free flight and exposed to the gust and overpressure effects of nearby nuclear detonations requires, ultimately, the solution of the three-dimensional, unsteady, fluid dynamical flow equations. Earlier researchers; particularly Tyler and Walker (31), Tyler (30), Walker (32), Jackomis (15), and Eaton (13) have approached such a solution in an orderly step-by-step procedure. A thorough review of the history of the development of numerical techniques for the solution of one- and two-dimensional hydrodynamics problems can be found in works published by these men.

The reference material analyzed herein will be limited to those works dealing with the three-dimensional problem. Sims (28) (29) calculated and tabulated the flow parameters for both zero and small angles of attack utilizing the theory as presented by Taylor and Macoll, Runge-Kutta, and Stone. Sims' results are similar to the work of Kopal, but he has corrected an inconsistency in the Kopal work and given his results in the more usable body-fixed coordinate system. Weilerstein, Sanlorenzo, and Petri (33) developed a three-dimensional characteristics solution for the flow field surrounding a spherically-capped cone. A method of characteristics solution such as that above provides a solution for the flow between the shock and the body.

Bohachevsky, Rubin, and Mates (7) solved the three-dimensional problem with a finite-difference scheme proposed by Lax which stabilizes the numerical procedure by introducing an average value into the forward time difference. They also used an ideal dissociating diatomic gas as the medium through which the vehicle under study is moving. Foster (14) compiled the experimental data for sharp and blunt nosed cones, both classified and unclassified, into a single two-volume source document. Experimental values of aerodynamic characteristics and pressure information for a very wide range of conditions are available in this reference. Babenko (4) solved the three-dimensional problem and tabulated his extensive results for the flow between body and its bow wave. The calculations were terminated when any discontinuity (such as a tail wave, or second shock) presented itself. Moretti and Bleich (20) solved for the three-dimensional flow around blunt bodies using a time-dependent numerical technique closely related to the Lax-Wendroff scheme. The shock wave, however, was considered to be a moving discontinuity and the Rankine-Hugoniot equations were applied across the shock. Jenkins (16) has surveyed the various numerical techniques of solving partial differential equations. He has reviewed and encapsulated the concept of stability and the criteria for assuring stability. He has paid particular attention to the development of finite difference solutions of fluid mechanical problems. Benokraitis (5) presents a technique of solution of the three-dimensional problem in Cartesian coordinates. In this method, density, velocity components, and specific energy are known in the center of a cell at time n . Subsequently, pressure and intermediate velocity component values are determined at time n . Mass outflow from each cell is next computed, then the mass in

the cell of time $(n + 1)$ is determined. Finally, velocity components and specific energy at time $(n + 1)$ are computed. Xerikos and Anderson (35) applied time-dependent finite difference techniques to the solution of the steady-state inviscid three-dimensional flow field by means of a floating mesh approach. In this technique, discontinuities such as shocks appear as discrete surfaces across which flow property discontinuities are specified by exact moving shock relations. Rusanov (27) developed a finite difference scheme for the solution of the three-dimensional problem not unlike that of Babenko (4). He has solved for the flow in the region bounded by the bow wave, the body, and any downstream discontinuity. Jones (17) tabulated results of calculations based on (a) an initial estimate of the position of the attached shock, and (b) iterating the solution to improve the shock shape until the normal velocity on the body surface approaches zero. He has compared his results with those of Babenko (4) and by solving test problems using a varying step size in both Mach number and cone half angle. Mosely and Wells (22) have tested an Apollo Command Module Configuration (33° half angle cone) at several Mach numbers and orientations and have reported the surface pressures which resulted.

Previous investigators have developed excellent techniques of determining the steady-state flow property values. This study will undertake to develop a technique to determine not only the steady-state flow solution but, more importantly, the transient flow conditions. Any technique to determine the transient solution must be a time dependent technique; and must be the simplest possible, so that computer costs do not become excessive. Consequently, the technique developed herein will be an explicit, first-order finite-difference scheme.

CHAPTER III

DEVELOPMENT OF FINITE-DIFFERENCE TECHNIQUES

Applicable Differential Equations

The differential equations which apply to the system under investigation are, in conservation form:

Continuity,

$$\frac{\partial \rho}{\partial t} + \bar{\nabla} \cdot \rho \bar{V} = 0 \quad ; \quad (3-1)$$

Momentum,

$$\frac{\partial(\rho \bar{V})}{\partial t} + (\bar{V} \cdot \rho [\bar{V} \bar{V}]) + \bar{\nabla} p = 0 \quad ; \quad (3-2)$$

Energy,

$$\frac{\partial e}{\partial t} + \bar{\nabla} \cdot (\{e + p\} \bar{V}) = 0 \quad . \quad (3-3)$$

In addition to the above set of equations, a relation between energy and pressure is required. The energy per unit volume of the fluid may be expressed as:

$$e = \frac{\rho |\bar{V}|^2}{2} + \frac{p}{K-1} \quad (3-4)$$

Equations (3-1) through (3-4) become, upon completion of the indicated operations, for cylindrical coordinates:

Continuity,

$$\frac{\partial \rho}{\partial t} + \frac{\partial(\rho v_z)}{\partial z} + \frac{1}{r} \frac{\partial(\rho v_\theta)}{\partial r} + \frac{\partial(\rho v_r)}{\partial r} + \frac{\rho v_r}{r} = 0 ; \quad (3-5)$$

r-momentum,

$$\frac{\partial(\rho v_r)}{\partial t} + \frac{\partial[(\rho v_r)v_r]}{\partial r} + \frac{\partial[(\rho v_r)v_z]}{\partial z} + \frac{1}{r} \frac{\partial[(\rho v_r)v_\theta]}{\partial \theta} + \frac{\rho v_r^2}{r} - \frac{\rho v_\theta^2}{r} + \frac{\partial p}{\partial r} = 0 ; \quad (3-6)$$

Z-momentum,

$$\frac{\partial(\rho v_z)}{\partial t} + \frac{\partial[(\rho v_z)v_r]}{\partial r} + \frac{\partial[(\rho v_z)v_z]}{\partial z} + \frac{1}{r} \frac{\partial[(\rho v_z)v_\theta]}{\partial \theta} + \frac{\rho v_z v_r}{r} + \frac{\partial p}{\partial z} = 0 ; \quad (3-7)$$

θ -momentum,

$$\frac{\partial(\rho v_\theta)}{\partial t} + \frac{\partial[(\rho v_\theta)v_r]}{\partial r} + \frac{\partial[(\rho v_\theta)v_z]}{\partial z} + \frac{1}{r} \frac{\partial[(\rho v_\theta)v_\theta]}{\partial \theta} + \frac{2\rho v_\theta v_r}{r} + \frac{1}{r} \frac{\partial p}{\partial \theta} = 0 ; \quad (3-8)$$

Energy,

$$\frac{\partial e}{\partial t} + \frac{\partial[(e + p)v_r]}{\partial r} + \frac{\partial[(e + p)v_z]}{\partial z} + \frac{1}{r} \frac{\partial[(e + p)v_\theta]}{\partial \theta} + \frac{v_r}{r} (e + p) = 0 ; \quad (3-9)$$

and, finally, the relationship which permits the determination of pressure,

$$P = (K - 1) \left[e - \frac{\rho}{2} (v_z^2 + v_\theta^2 + v_r^2) \right] \quad (3-10)$$

Non-Dimensionalizing the Dependent Variables

The dependent variables ρ , p , V_z , V_θ , V_r , and e have been non-dimensionalized with the following techniques:

$$\text{non-dimensional density, } \rho' = \frac{\rho}{\rho_\infty} ; \quad (3-11)$$

$$\text{non-dimensional pressure, } p' = \frac{p}{p_\infty} ; \quad (3-12)$$

$$\text{non-dimensional velocities, } V'_z = \frac{V_z}{\sqrt{\frac{p_\infty}{\rho_\infty}}} , \quad (3-13)$$

$$V'_\theta = \frac{V_\theta}{\sqrt{\frac{p_\infty}{\rho_\infty}}} , \quad (3-14)$$

$$V'_r = \frac{V_r}{\sqrt{\frac{p_\infty}{\rho_\infty}}} ; \quad (3-15)$$

$$\text{non-dimensional distance, } r' = \frac{r}{H} \quad (3-16)$$

$$\text{where } H \text{ is a characteristic length, } z' = \frac{z}{H} ; \quad (3-17)$$

$$\text{non-dimensional time, } t' = \frac{t}{H} \sqrt{\frac{p_\infty}{\rho_\infty}} ; \quad (3-18)$$

$$\text{and non-dimensional energy, } e' = \frac{e}{p_\infty} . \quad (3-19)$$

Substitution of Equations (3-11) through (3-19) into the set of flow Equations (3-5) through (3-10) results in a dimensionless set of flow equations identical in form to the original set (3-5) through (3-10); with the single exception that all previously dimensioned

variables have acquired a prime ('), indicating they have become dimensionless. The procedure has been carried through below for the continuity equation.

Equation (3-5), the continuity equation, was non-dimensionalized in the following manner. Density (ρ) was replaced by its equivalent $\rho' \rho_\infty$ from Equation (3-11). Similarly, other equivalents are: time (t) replaced by its equivalent $\frac{t'H}{\sqrt{\frac{p_\infty}{\rho_\infty}}}$; axial velocity (V_z) by $V'_z \sqrt{\frac{p_\infty}{\rho_\infty}}$; crossflow velocity (V_θ) by $V'_\theta \sqrt{\frac{p_\infty}{\rho_\infty}}$; radial velocity (V_r) by $V'_r \sqrt{\frac{p_\infty}{\rho_\infty}}$;

and radius (r) by $r'H$. The resultant equation is:

$$\frac{\partial(\rho' \rho_\infty)}{\partial \left(\frac{t'H}{\sqrt{\frac{p_\infty}{\rho_\infty}}} \right)} + \frac{\partial \left(V'_z \sqrt{\frac{p_\infty}{\rho_\infty}} \rho' \rho_\infty \right)}{\partial (Z'H)} + \frac{1}{r'H} \frac{\partial \left(\rho' \rho_\infty V'_\theta \sqrt{\frac{p_\infty}{\rho_\infty}} \right)}{\partial \theta} + \frac{\partial \left(\rho' \rho_\infty V'_r \sqrt{\frac{p_\infty}{\rho_\infty}} \right)}{\partial (r'H)} + \frac{\rho' \rho_\infty V'_r \sqrt{\frac{p_\infty}{\rho_\infty}}}{r'H} = 0 ; \quad (3-20)$$

or,

$$\begin{aligned}
\rho_{\infty} = & \frac{\sqrt{\frac{p_{\infty}}{\rho_{\infty}}}}{H} \frac{\partial \rho'}{\partial t'} + \frac{\rho_{\infty} \sqrt{\frac{p_{\infty}}{\rho_{\infty}}}}{H} \frac{\partial (\rho' v_z')}{\partial z'} + \frac{\rho_{\infty} \sqrt{\frac{p_{\infty}}{\rho_{\infty}}}}{H} \left[\frac{1}{r'} \frac{\partial (\rho' v_{\theta}')}{\partial \theta} \right] \\
& + \frac{\rho_{\infty} \sqrt{\frac{p_{\infty}}{\rho_{\infty}}}}{H} \frac{\partial (\rho' v_r')}{\partial r'} + \frac{\rho_{\infty} \sqrt{\frac{p_{\infty}}{\rho_{\infty}}}}{H} \frac{\rho' v_r'}{r'} = 0. \quad (3-21)
\end{aligned}$$

When the constant multiplier $\frac{\rho_{\infty} \sqrt{\frac{p_{\infty}}{\rho_{\infty}}}}{H}$ has been divided out of each term of Equation (3-21), the resultant non-dimensionalized continuity equation is identical in form to Equation (3-5), except for the appearance of primes (') over all previously dimensioned variables,

$$\frac{\partial \rho'}{\partial t} + \frac{\partial (\rho' v_z')}{\partial z'} + \frac{1}{r'} \frac{\partial (\rho' v_{\theta}')}{\partial \theta} + \frac{\partial (\rho' v_r')}{\partial r'} + \frac{\rho' v_r'}{r'} = 0. \quad (3-22)$$

The set of Equations (3-5) through (3-10) are the basis for the investigation to be undertaken, and are correct either in dimensioned or dimensionless form. Throughout the remainder of this study the variables under investigation will be dimensionless but the primes have been dropped for the sake of simplicity.

Finite-Difference Representation of the Differential Equations

The five differential Equations (3-5) through (3-9) can be seen to be of the same form, i.e.,

$$\frac{\partial f}{\partial t} + \frac{\partial F^z}{\partial z} + \frac{1}{r} \frac{\partial F^\theta}{\partial \theta} + \frac{\partial F^r}{\partial r} + \psi = 0, \quad (3-23)$$

where f , F^z , F^θ , F^r , ψ for the set of flow equations are

$$f = \begin{Bmatrix} \rho \\ \rho V_r \\ \rho V_z \\ \rho V_\theta \\ e \end{Bmatrix}, \quad F^z = \begin{Bmatrix} \rho V_z \\ V_z (\rho V_r) \\ V_z (\rho V_z) + p \\ V_z (\rho V_\theta) \\ V_z (e + p) \end{Bmatrix},$$

$$F^\theta = \begin{Bmatrix} \rho V_\theta \\ V_\theta (\rho V_r) \\ V_\theta (\rho V_z) \\ V_\theta (\rho V_\theta) + p \\ V_\theta (e + p) \end{Bmatrix}, \quad F^r = \begin{Bmatrix} \rho V_r \\ V_r (\rho V_r) + p \\ V_r (\rho V_z) \\ V_r (\rho V_\theta) \\ V_r (e + p) \end{Bmatrix}$$

$$\text{and } \psi = \left\{ \begin{array}{l} \frac{\rho V_r}{r} \\ \frac{\rho V_r^2}{r} - \frac{\rho V_\theta^2}{r} \\ \frac{\rho V_z V_r}{r} \\ \frac{2\rho V_\theta V_r}{r} \\ \frac{V_r}{r} (e + p) \end{array} \right\} \quad (3-24)$$

The determination of the salient properties of a three-dimensional flow field $(\rho, V_z, V_r, V_\theta, e, p)$ requires the simultaneous solution of the six Equations (3-5) through (3-10). The method used in this study was originated by Rusanov for two-dimensional problems. The Rusanov technique makes use of artificial second order blurring or dissipative terms which permit calculations to be made through strong gradients such as shock waves. The effect of the added dissipative terms is to diffuse strong gradients such as shocks over distances sufficient to permit the use of classical finite-difference methods. The result of this addition is to cause shock waves to become shock "bands" with widths of a few mesh spacings. In addition, judicious selection of the size of the dissipative terms is designed to: (1) accomplish the diffusion of strong gradients while causing a negligible effect in regions without such gradients; and, (2) stabilize the calculations so that the final solutions asymptotically approach a steady-state conditions.

The general form of the flow Equation (3-23), with dissipative terms added, in three-dimensional cylindrical coordinates, is:

$$\begin{aligned} \frac{\partial f}{\partial t} + \frac{\partial F^z}{\partial Z} + \frac{1}{r} \frac{\partial F^\theta}{\partial \theta} + \frac{\partial F^r}{\partial r} + \psi = & \frac{\partial}{\partial Z} \left[A(Z, \theta, r, t) \frac{\partial f}{\partial Z} \right] + \frac{1}{r} \frac{\partial}{\partial r} \left[r B(Z, \theta, r, t) \frac{\partial f}{\partial r} \right] \\ & + \frac{1}{r} \frac{\partial}{\partial \theta} \left[C(Z, \theta, r, t) \frac{1}{r} \frac{\partial f}{\partial \theta} \right]. \end{aligned} \quad (3-25)$$

The field to be investigated is made up of a series of discrete mesh points within which is imbedded the body. The body in the flow in this study was a 30° half-angle right circular cone. Figure 1 shows the mesh point relationship to field and body boundaries for one plane of mesh points. The entire field was composed of 21 such planes, oriented on radii emanating from the cone axis at 9° angles from each other. Figures 2 and 3 show the details of the mesh and the nomenclature associated with determining a particular mesh points location.

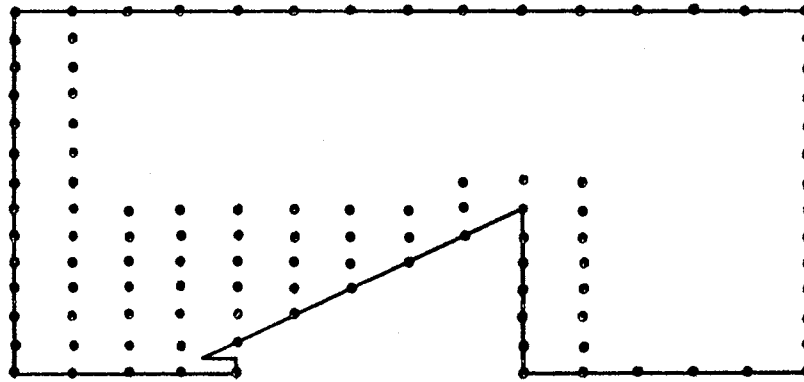


Figure 1. Relationship of Mesh Points to Field and Body Boundaries

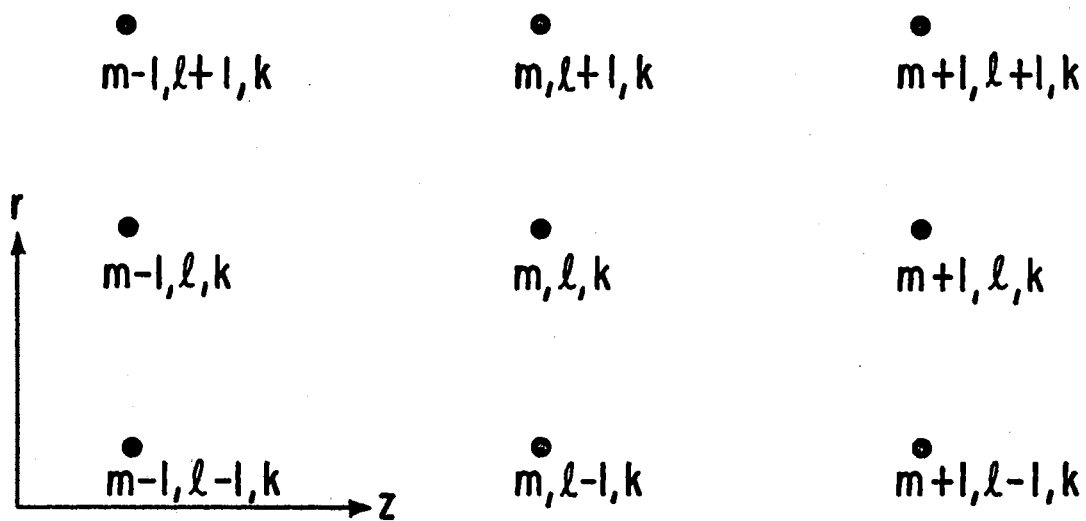


Figure 2. Nomenclature for an r - z Plane of Mesh Points

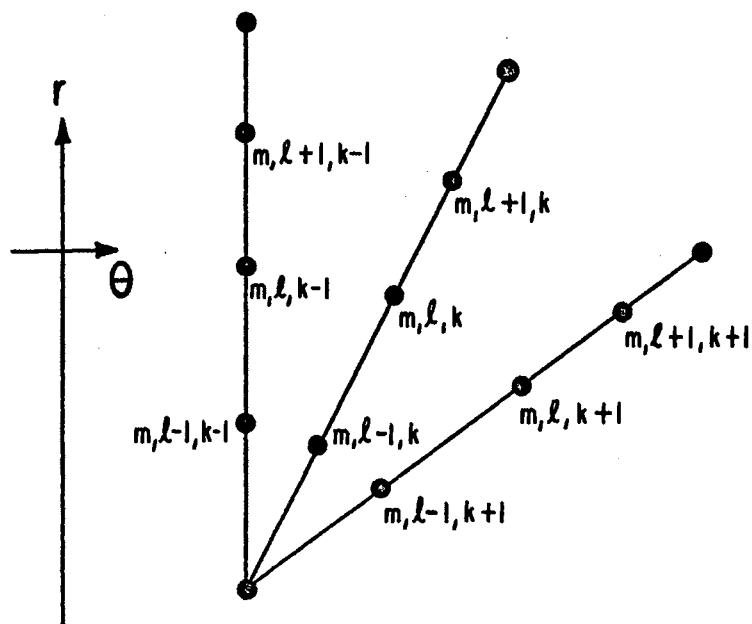


Figure 3. Nomenclature for an r - θ Plane of Mesh Points

The distance between mesh points in the Z -coordinate direction is $h_1 = 1$; and the distance between points in the r -coordinate direction is h_2 , where h_2 is determined by the relation $\tan \varphi = h_2/h_1$. The angle φ is the cone half angle. The result of this relationship between h_1 and h_2 is that in any r - Z plane of mesh points the cone surface is parallel to right-running diagonals of the mesh, and coincides with one of those diagonals. The distance between mesh points in the θ coordinate direction is $r\Delta\theta$. The expression $r\Delta\theta$ can be expressed as $(\ell - 1)h_2\frac{\pi}{20}$.

Truncated Taylor series expansions will be used to approximate the derivatives of Equation (3-25). Centered differences will be used for spatial derivatives at the most general type of mesh point; i.e., one which is not on any boundary; and forward differences will be applied to time derivatives. Special techniques will be required for mesh points located on boundaries and a discussion of these will be found in Chapter IV. Examples of the forms of expansion to be used are:

$$\frac{\partial f}{\partial t} = \frac{f_{m,1,k}^{n+1} - f_{m,1,k}^n}{\tau} \quad (3-26)$$

$$\frac{\partial F^Z}{\partial Z} = \frac{F_{m+1,1,k}^Z - F_{m-1,1,k}^Z}{2h_1} \quad (3-27)$$

$$\begin{aligned} \frac{\partial}{\partial Z} \left[A(Z, \theta, r, t) \frac{\partial f}{\partial Z} \right] = & \frac{1}{h_1^2} \left[A_{m+1/2,1,k}^n (f_{m+1,1,k}^n - f_{m,1,k}^n) \right. \\ & \left. - A_{m-1/2,1,k}^n (f_{m,1,k}^n - f_{m-1,1,k}^n) \right] \end{aligned} \quad (3-28)$$

Equation (3-25) can now be expressed in finite difference form, with forms as shown by Equations (3-26) through (3-28), as:

$$\begin{aligned}
& \frac{f_{m,1,k}^{n+1} - f_{m,1,k}^n}{\tau} + \frac{(F_{m+1,1,k}^z - F_{m-1,1,k}^z)^n}{2h_1} + \frac{(F_{m,1+1,k}^r - F_{m,1-1,k}^r)^n}{2h_2} \\
& + \frac{(F_{m,1,k+1}^\theta - F_{m,1,k-1}^\theta)^n}{2h_3} + \psi_{m,1,k}^n = \frac{1}{h_1^2} \left[A_{m+1/2,1,k}^n \right. \\
& \left. (f_{m+1,1,k}^n - f_{m,1,k}^n) - A_{m-1/2,1,k}^n (f_{m,1,k}^n - f_{m-1,1,k}^n) \right] + \\
& \frac{1}{r h_2^2} \left[(rB)_{m,1+1/2,k}^n (f_{m,1+1,k}^n - f_{m,1,k}^n) - (rB)_{m,1-1/2,k}^n \right. \\
& \left. (f_{m,1,k}^n - f_{m,1-1,k}^n) \right] + \frac{1}{r^2 h_3^2} \left[C_{m,1,k+1/2}^n (f_{m,1,k+1}^n - f_{m,1,k}^n) \right. \\
& \left. - C_{m,1,k-1/2}^n (f_{m,1,k}^n - f_{m,1,k-1}^n) \right]. \quad (3-29)
\end{aligned}$$

The following relations are defined:

$$A_{m,1,k}^n \equiv \frac{h_1^2}{2\tau} \alpha_{m,1,k}^n, \quad (3-30)$$

$$(rB)_{m,1,k}^n \equiv \frac{r_2^2}{2\tau} \beta_{m,1,k}^n, \quad (3-31)$$

$$C_{m,1,k}^n \equiv \frac{r^2 h_3^2}{2\tau} \gamma_{m,1,k}^n, \quad (3-32)$$

$$k_1 \equiv \frac{\tau}{h_1}, \quad (3-33)$$

$$k_2 \equiv \frac{\tau}{h_2}, \quad (3-34)$$

$$k_3 \equiv \frac{\tau}{h_3}, \quad (3-35)$$

$$A_{m+1/2,1,k}^n = \frac{1}{2}(A_{m+1,1,k}^n + A_{m,1,k}^n), \quad (3-36)$$

$$B_{m,1+1/2,k}^n = \frac{1}{2}(B_{m,1+1,k}^n + B_{m,1,k}^n), \quad (3-37)$$

$$C_{m,1,k+1/2}^n = \frac{1}{2}(C_{m,1,k+1}^n + C_{m,1,k}^n). \quad (3-38)$$

Simultaneous substitution of Equations (3-30) through (3-38), collection of terms where possible, and solution for $f_{m,1,k}^{n+1}$ results in the following:

$$\begin{aligned} f_{m,1,k}^{n+1} = & f_{m,1,k}^n - \frac{k_1}{2} (F_{m+1,1,k}^z - F_{m-1,1,k}^z)^n \\ & - \frac{k_2}{2} (F_{m,1+1,k}^r + F_{m,1-1,k}^r)^n - \frac{k_3}{2} (F_{m,1,k+1}^\theta - F_{m,1,k-1}^\theta)^n \\ & - \tau \psi_{m,1,k}^n + \frac{1}{4} \left[(\alpha_{m+1,1,k}^n + \alpha_{m,1,k}^n) (f_{m+1,1,k}^n - f_{m,1,k}^n) \right. \end{aligned}$$

$$\begin{aligned}
& - (\alpha_{m,1,k}^n + \alpha_{m-1,1,k}^n)(f_{m,1,k}^n - f_{m-1,1,k}^n) + \\
& (\beta_{m,1+1,k}^n + \beta_{m,1,k}^n)(f_{m,1+1,k}^n - f_{m,1,k}^n) - \\
& (\beta_{m,1,k}^n + \beta_{m,1-1,k}^n)(f_{m,1,k}^n - f_{m,1-1,k}^n) + \\
& (\gamma_{m,1,k+1}^n - \gamma_{m,1,k}^n)(f_{m,1,k+1}^n - f_{m,1,k}^n) - \\
& (\gamma_{m,1,k}^n + \gamma_{m,1,k-1}^n)(f_{m,1,k}^n - f_{m,1,k-1}^n) \Big] . \quad (3-39)
\end{aligned}$$

The stability coefficients α , β , and γ were determined through the use of the standard Rusanov technique as documented in reference (30), and modified for a three-dimensional problem in accordance with suggestions put forward in reference (36). Further modifications were required in order to stabilize the entire flow field, especially the base corner region. The equation for the three coefficients can be represented by the following:

$$\alpha_{m,1,k} = \frac{|\bar{V}| \cdot \sigma_0 \cdot (|\bar{V}| + c)_{m,1,k}}{2(|\bar{V}| + c)_{\max}} \cdot \left(\frac{L}{1}\right)^3 ; \quad (3-40)$$

where

σ_0 is the assigned Courant number,

c is the local sonic velocity, and

L is the diagonal of a chosen mesh volume given by;

$$L = \frac{\tan \varphi \cdot (\tan \varphi \times .15708) \times 9}{[(\tan \varphi)^2 + (\tan \varphi \times .15708 \times 9)^2 + (\tan^2 \varphi \times .15708 \times 9)^2]^{1/2}}$$

The mesh volume chosen for the evaluation of the term L was located at $l = 10$ in order to provide stable solutions for the entire flow field throughout the interval of time under investigation. A constant value of L was chosen to avoid problems associated with terms involving $\frac{1}{r}$ when r becomes small. The determination of β and γ was identical to that for α with the exception that for β , 1 is replaced by $\tan\varphi$; and for γ , 1 is replaced by $(l-1)\frac{\pi}{20} \tan\varphi$.

CHAPTER IV

BOUNDARY INVESTIGATION

The characteristics of the field solution may be profoundly affected by the manner in which boundaries are handled. Several different boundary techniques were attempted in order to obtain a proper solution for the flow field under investigation. The boundaries of the flow field in this study are shown in Figures 4 and 5. They are the upstream, downstream, outer, and plane of symmetry boundaries; and, in addition, the boundaries of the body itself.

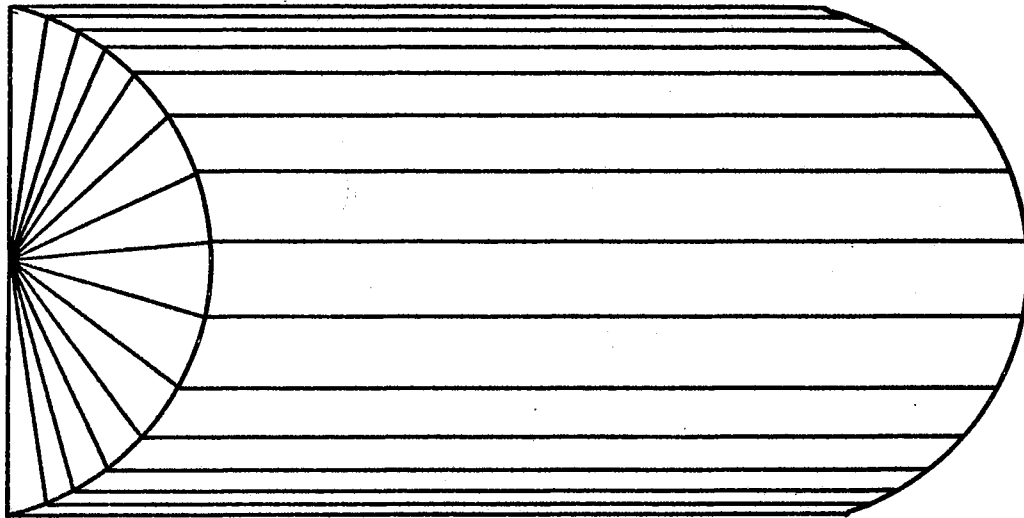


Figure 4. Exterior View of Flow Field

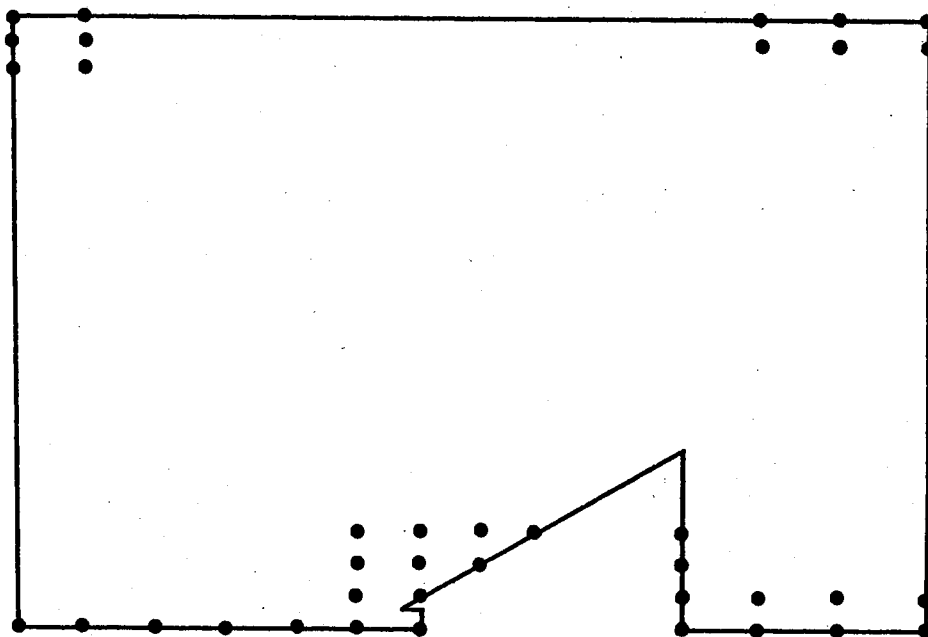


Figure 5. Interior View of A Plane of Mesh Points
Showing All Boundaries

Although not a true boundary, the axis of the body-fixed cylindrical coordinate system is an area which requires special consideration, so will be discussed in this chapter.

Axis of the Field

The axis presents a problem because of the appearance of terms involving the radius, r , and its inverse. In either case, as r approaches zero the solution of any equation such as (3-39) is impossible. Initially, to circumvent the problem, all terms involving r or $\frac{1}{r}$ were evaluated at the next row of mesh points, i.e., $\ell = 2$. At the same time, terms involving the angular coordinate θ were appearing but had no meaning since a point on the axis $(m, 1, k)$ is no different

from the point in the neighboring theta-plane $(m, 1, k+1)$. Preliminary results appeared to be adequate, but without basis in fact, and this technique was abandoned. The second technique for handling the area where the radius becomes small was to arrange the field of mesh points so that the first row did not coincide with the axis, but rather occupied the position of $\ell = \frac{1}{2}$, or $r = h_2/2$. Figure 6 shows the mesh point arrangement used for this technique. Use of the off-axis technique removes both objections to the first method discussed; i.e., the radius never reaches zero, and the point in a neighboring theta-plane has usable values for incorporation into the finite difference equation. The results achieved with the off-axis technique were unstable, however, and the method was abandoned. It is possible that useful results with this method could be achieved when all other difficulties with the computer code have been eliminated. The third technique attempted and the method finally adopted, was to consider a row of mesh points coincident with the coordinate axis, the row above ($k=1$), the row below ($k=21$), and the row at 90° to the plane of the first three rows ($k=11$), together with its reflection, as being in a Cartesian coordinate system. This method required the rederivation of the basic finite-difference equation, and of the conservation Equations (3-5) through (3-10). The finite difference equation which applies is

$$f_{m,1,k}^{n+1} = f_{m,1,k}^n - \frac{K_1}{2} (F_{m+1,1,k}^x - F_{m-1,1,k}^x)^n - \frac{K_2}{2} (F_{m,1+1,k}^y - F_{m,1-1,k}^y)^n - \frac{K_3}{2} (F_{m,1,k+1}^z - F_{m,1,k-1}^z)^n$$

$$\begin{aligned}
& + \frac{1}{4} [(\alpha_{m+1,1,k}^n + \alpha_{m,1,k}^n) (f_{m+1,1,k}^n - f_{m,1,k}^n) \\
& - (\alpha_{m,1,k}^n + \alpha_{m-1,1,k}^n) (f_{m,1,k}^n - f_{m-1,1,k}^n) \\
& + (\beta_{m,1+1,k}^n + \beta_{m,1,k}^n) (f_{m,1+1,k}^n - f_{m,1,k}^n) \\
& - (\beta_{m,1-1,k}^n + \beta_{m,1,k}^n) (f_{m,1,k}^n - f_{m,1-1,k}^n) \\
& + (\gamma_{m,1,k+1}^n + \gamma_{m,1,k}^n) (f_{m,1,k+1}^n - f_{m,1,k}^n) \\
& - (\gamma_{m,1,k}^n + \gamma_{m,1,k-1}^n) (f_{m,1,k}^n - f_{m,1,k-1}^n)] \quad (4-1)
\end{aligned}$$

where

$$\begin{aligned}
f &= \begin{pmatrix} \rho \\ \rho u \\ \rho v \\ \rho w \\ e \end{pmatrix} & F^x &= \begin{pmatrix} \rho u \\ (\rho u^2 + p) \\ \rho uv \\ \rho uw \\ (e + p)u \end{pmatrix} \\
F^y &= \begin{pmatrix} \rho v \\ \rho uv \\ (\rho v^2 + p) \\ \rho vw \\ (e + p)v \end{pmatrix} & F^z &= \begin{pmatrix} \rho w \\ \rho uw \\ \rho vw \\ (\rho w^2 + p) \\ (e + p)w \end{pmatrix} . \quad (4-2)
\end{aligned}$$

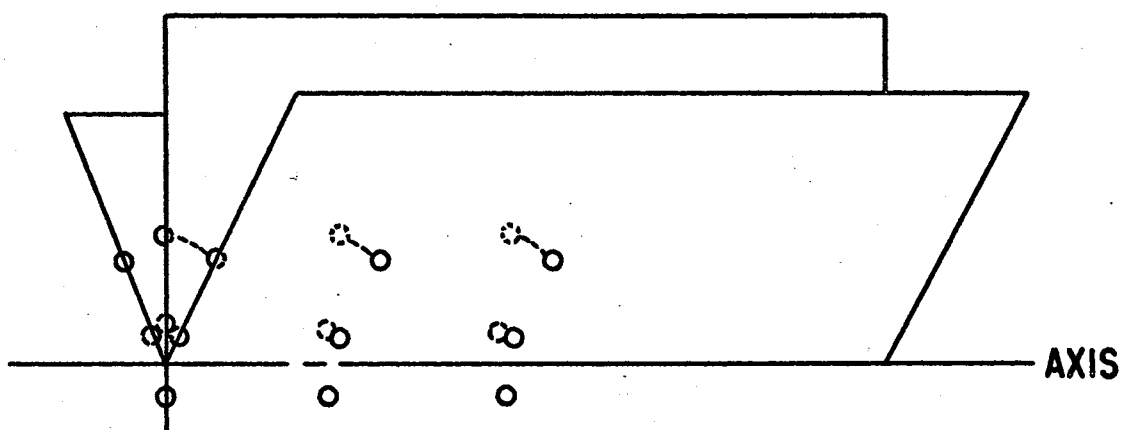


Figure 6. Mesh Point Arrangement for Off-Axis Technique

Table I relates variables and dimensions in the cylindrical coordinate system to those in the Cartesian system.

Stagnation Point

Initial flow field solutions were obtained incorporating a "sharp point" stagnation point technique. The sharp point technique utilized the flow conditions one mesh point upstream from the stagnation point as the input to an isentropic stagnation calculation. Stagnation pressure values from this method were sufficiently low to cause concern and initiation of the second method of determining stagnation point values, the "blunt-nose" method. The blunt-nose technique (13) was based on a cone configuration as shown in Figure 7. In this configuration, the stagnation point calculation, still isentropic, does not depend directly on the cone surface properties. Since the flow properties one mesh point upstream from the stagnation point are used in the isentropic calculation for stagnation point properties, it was necessary to

TABLE I
RELATION BETWEEN VARIABLES IN CYLINDRICAL
AND CARTESIAN COORDINATES

	Cylindrical Coordinates	Cartesian Coordinates
Axial velocity	V_z	u
Radial velocity	V_r	v
Crossflow velocity	V_θ	w
Axial dimension (m)	z	X
Radial dimension (ℓ)	r	Y
Crossflow dimension (k)	θ	Z
Mesh point nomenclature		
m	$m = 2$	$m = 2$
ℓ	$\ell = 2$	$\ell = 2$
k	$k = 11$	$k = 2$

include, in the computer code, the capability to decide what mesh point constitutes "one mesh point upstream". As the angle of attack increased, the point whose values are to be stagnated changes. For angles of attack from zero to 16° , the mesh point on the axis in front of the stagnation point was used for determination of stagnation point properties. At angles of attack between 16° and 41° , the point used was one column upstream and one row to windward of the stagnation point.

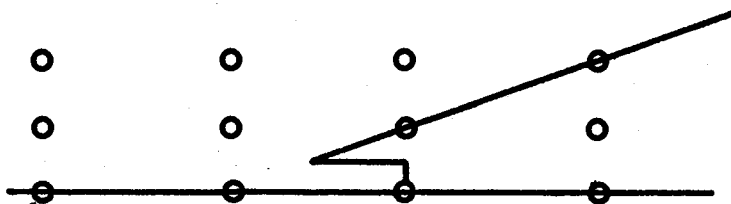


Figure 7. Blunt-Nose Configuration

Cone Surface

The flow property values at mesh points on the cone surface were determined using a rotated cylindrical coordinate system. The rotated system was aligned so that the Z -axis coincided with the cone surface and the r -axis was oriented perpendicular to and increasing away from the surface. Figure 8 shows the mesh point arrangement used to determine surface property values. The new flow property values at point (7)

were determined using values from mesh points (5'), (8'), (9), and points in the adjoining theta-planes. Property values at mesh point (8') were determined by interpolation between points (8), (11), (10), and (7). The boundary condition to be satisfied on the cone surface was that the radial velocity in the rotated coordinate system should be zero.

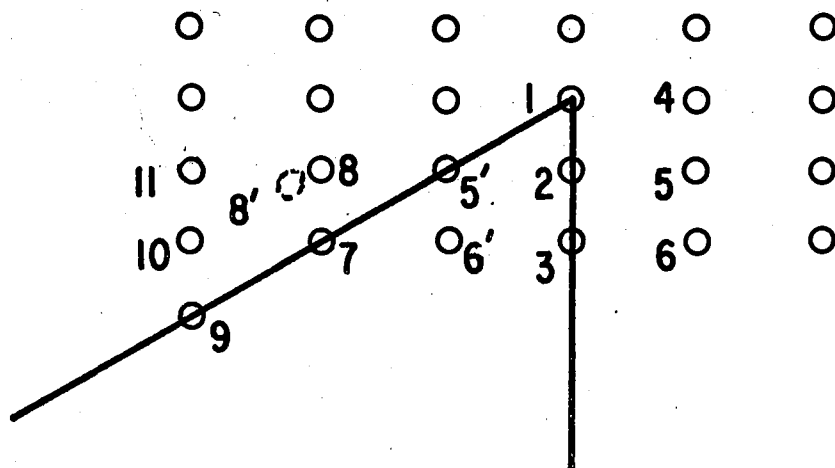


Figure 8. Mesh Point Configuration in Base Corner Region

The basic equation to be solved (3-39) assumes a slightly different form when the trigonometric relationships involved in the coordinate rotation are employed. On the surface, the equation to be solved is the following:

$$\begin{aligned}
\tilde{f}_{m,1,k}^{n+1} &= \tilde{f}_{m,1,k}^n - \frac{K_1}{2} \cos \varphi [\tilde{F}_{m+1,1+1,k}^z - \tilde{F}_{m-1,1-1,k}^z]^n \\
&- K_2 [\cos^2 \varphi \tilde{F}_{m,1+1,k}^r + \sin^2 \varphi \tilde{F}_{m-1,1,k}^r]^n \\
&- \frac{K_3}{2} [\tilde{F}_{m,1,k+1}^\theta - \tilde{F}_{m,1,k-1}^\theta]^n + \frac{\cos^2 \varphi}{4} \left[\frac{(\alpha_{m+1,1+1,k}^n + \alpha_{m+1,k}^n)}{k} \right. \\
&(\tilde{f}_{m+1,1+1,k}^n - \tilde{f}_{m,1,k}^n) + (\alpha_{m-1,1-1,k}^n + \alpha_{m,1,k}^n)(\tilde{f}_{m-1,1-1,k}^n - \\
&\tilde{f}_{m,1,k}^n) \left. \right] + \frac{1}{4} [(\gamma_{m,1,k+1}^n + \gamma_{m,1,k}^n)(\tilde{f}_{m,1,k+1}^n - \tilde{f}_{m,1,k}^n) \\
&- (\gamma_{m,1,k-1}^n + \gamma_{m,1,k}^n)(\tilde{f}_{m,1,k}^n - \tilde{f}_{m,1,k-1}^n)] \quad (4-3)
\end{aligned}$$

The repeated solution of Equation (4-3) for ρ , ρV_r , ρV_z , ρV_θ , and e on the surface requires terms for each of the items in Equation (4-3) that have a hat (\sim) over them. Specifically, they are:

$$\tilde{f} = \left\{ \begin{array}{l} \rho \\ \rho V_z \cos \varphi + \rho V_r \sin \varphi \\ \rho V_\theta \\ e \end{array} \right\} \quad \tilde{F}_z = \left\{ \begin{array}{l} \rho V_z \cos \varphi + \rho V_r \sin \varphi \\ \frac{(\rho V_z \cos \varphi + \rho V_r \sin \varphi)^2}{\rho} + p \\ \frac{\rho V_\theta (\rho V_z \cos \varphi + \rho V_r \sin \varphi)}{\rho} \\ \left[\frac{(\rho V_z \cos \varphi + \rho V_r \sin \varphi)}{\rho} \right] (e + p) \end{array} \right\}$$

$$\begin{aligned}
 \tilde{F}^{\theta} &= \left\{ \begin{aligned} &\rho V_{\theta} \\ &(\rho V_z \cos\varphi + \rho V_r \sin\varphi) \frac{\rho V_{\theta}}{\rho} \\ &\frac{(\rho V_{\theta})^2}{\rho} + p \\ &\frac{\rho V_{\theta}}{\rho} (e + p) \end{aligned} \right\} \\
 \tilde{F}^r &= \left\{ \begin{aligned} &\rho V_r \cos\varphi - \rho V_z \sin\varphi \\ &(\rho V_z \cos\varphi + \rho V_r \sin\varphi)(\rho V_r \cos\varphi - \rho V_z \sin\varphi)/\rho \\ &\frac{\rho V_{\theta}}{\rho} (\rho V_r \cos\varphi - \rho V_z \sin\varphi) \\ &(\rho V_r \cos\varphi - \rho V_z \sin\varphi) \left(\frac{e + p}{\rho} \right) . \end{aligned} \right\} \quad (4-4)
 \end{aligned}$$

Cone Base

The flow properties in the base region of the cone were determined using the principle of reflection. This technique assumes the presence of a "mirror image" inside the cone of the plane of mesh points one column downstream of the cone base. The axial velocity (V_z) was set equal to zero to enforce the "no-flow" requirement. Difficulty with the base region, particularly near the intersection of the cone surface and the base, caused several different techniques for handling the base corner points to be investigated. First, no special attention was paid to the area. The cone-surface techniques were utilized for the mesh point at the intersection of the cone surface and the base.

Straightforward use of the reflection principle described above for the mesh point on the base one row down from the corner resulted in an unstable solution. Figure 8 shows the points in the area where difficulty was encountered.

The second technique investigated was the insertion of a false wall midway between points 1 and 2 on Figures 8 and 9. Point 1 was determined as before, but point 2 properties were determined using the reflection principle as mentioned earlier, and in addition, to account for the presence of the false wall. Physically, point 2 properties were determined using, for terms requiring a value at $(m, \ell+1, k)$, mirror images of point 2 properties. Results with this technique also were unstable and the method was abandoned. The third approach investigated, and the one which was successful, was to consider point 1 double valued. In other words, property values at point 1 on the cone surface were determined using cone-surface techniques; while point 1 property values on the base, were determined using the reflection technique mentioned above twice, but with the false wall at a position coincident with point 1. Figure 9 shows the arrangement. With this method, the evaluation of property values at point 1 on the cone base involves the reflection of values at point 4 and the reflection of values at point 2. Results with this method were stable.

Upstream Field Boundary

Flow property values at the upstream boundary $(1, \ell, k)$ were specified at all times and, therefore, did not require any special numerical technique.

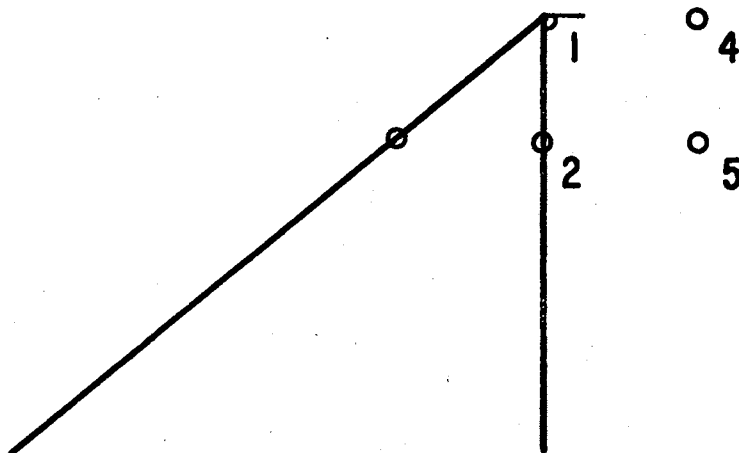


Figure 9. Cone Base Corner Configuration

Downstream Field Boundary

Flow property values for the downstream boundary (m_{\max} , l , k) were repeated from the first column upstream ($m_{\max}-1$, l , k). This technique ensured zero slope in property values at the downstream boundary.

Outer Field Boundary

The first technique applied to the outer boundary involved the use of flow property values within the flow one ($l_{\max}-1$) and two ($l_{\max}-2$) rows from the outer boundary for determination of first partials and rows l_{\max} , $l_{\max}-1$, and $l_{\max}-2$ for determination of second partials in the finite difference solution of the partial differential equations. The result of the application of this technique was that strong gradients (shocks) did not proceed downstream as quickly or as far as desired. Shock angles resulting from the use of this technique were significantly higher than theory (17) had predicted. The failure of

this method led to the adoption of a second technique based on a qualitative knowledge of the flow. Flow property values at the boundary at any given mesh point (m, ℓ_{\max}, k) were made equal to the property values at $(m-1, \ell_{\max}-1, k)$ since the desired shock angles, for this study, were of the order of φ ; the cone half-angle.

The rationale for the adoption of such a seemingly arbitrary scheme is as follows:

- (1) If the outermost edges of the mesh are sufficiently remote from the body, the body will not influence the outer flow except in the band of mesh points interior to the shock wave. In this instance, flow property values will be substantially identical at adjacent mesh points.
- (2) In the event that the mesh is not large enough to extend outside the shock-expansion fan interaction region, the region of flow upstream of the "shock band" is still amenable to treatment by this technique since property values are largely independent of position. Similar conditions exist downstream of the shock and upstream of the expansion fan when distances from the disturbing body are significant. The adoption of the technique discussed above does not tend to retard the shock waves downstream movement as significantly as the original back-differencing method. A calculation at a mesh point just upstream of the shock position will, for the back differencing method, be significantly effected by two mesh points immediately adjacent in a radial direction. These points will have property values reflecting the fact that they are in the shock. The result of such a calculation

will be to raise the property value being calculated above that desired. The use of the second technique, or "diagonal repeat," will alleviate such a problem so long as the shock wave angle is approximately the same as the diagonal angle of the mesh. When the shock angle is greater than the mesh diagonal angle the shock will tend to move downstream more than desired. When the shock angle is less than the mesh diagonal angle the shock will be somewhat retarded in its rearward movement, but considerably less than with back differencing as was originally attempted.

Plane of Symmetry

The plane of symmetry included the planes $(m, \ell, 1)$ and $(m, \ell, 21)$. Flow property values in the plane of symmetry were determined using the principle of reflection. An imaginary plane was visualized as existing to one side of the plane of symmetry with flow properties identical with the plane $(m, \ell, 2)$ or $(m, \ell, 20)$, as applicable. The flow properties of density (ρ), axial momentum (ρV_z), radial momentum (ρV_r), pressure (p), and energy (e) in such an imaginary plane were identical to the corresponding properties in the real plane; while the crossflow velocity (V_θ) had a change in sign in the imaginary plane compared to its value in the real plane. As a result of this change in sign, the crossflow momentum (ρV_θ) had a change in sign, as well as any other combination of terms involving the crossflow velocity raised to the first power.

CHAPTER V

RESULTS

The numerical technique described in Chapters III and IV was used, in its final form, to determine solutions for the flow field properties surrounding a 30° half angle cone in Mach 3.0 flight at angles of attack of 0, 10, 20, and 30 degrees. Although the study was conceived as an investigation of flow about a cone-cylinder, the effort was re-directed to the study of flow about the cone before usable results had been obtained. The prime purpose of investigating cone flow was to determine whether the techniques used herein were sufficient to provide an indication of wake flow properties while providing a stable solution. Since the wake extended less than one-half the body length of the cone, it was not expected that the wake flow conditions would be reliably accurate. Usable wake flow data presupposes the use of a field of mesh points which would extend on the order of one and one-half body lengths behind the cone.

Each angle of attack solution was carried through 1000 time planes. The rate of change of flow field properties had decreased to about five per cent per 100 time planes at 1000 time planes, therefore, the solutions were deemed to be "quasi-steady" at that point. A few test runs were carried to 2000 time planes to investigate stability and flow property values. In all these cases the flow remained stable and the

flow property values were not sufficiently different from those at 1000 time planes to warrant their inclusion herein.

Initial development of the computer code was accomplished using the Oklahoma State University IBM 7040. All production runs, micro-filming, and movie making was accomplished using the CDC 6600 facilities of the Air Force Weapons Laboratory. The movie making effort was limited to the production of a two-minute film of the windward/leeward velocity vector map depicting the change of velocity as a function of time plane beginning at time plane 100.

The CDC 6600 computer time required for the generation of any single solution from time plane 0 to time plane 1000 was 225 minutes. This amount of time is central processor time and does not include the time required for paper printout or microfilming. A paper printout of flow field property values (ρ , ρV_z , ρV_x , ρV_θ , e , p) was obtained for each mesh point every 100 time planes.

Zero Angle of Attack Solution

A solution for an angle of attack of zero ($\alpha = 0^\circ$) was determined because:

- (1) Theoretical and experimental data were more easily obtainable for comparison purposes
- (2) It is desired to test the applicability and symmetry of the computer program to such a special case of the general three-dimensional problem.

The data resulting from the solution for $\alpha = 0^\circ$ is presented in Figures 10 through 16 in summary form. Velocity vector maps and pressure profiles are included for time planes 100, 500, and 1000. The

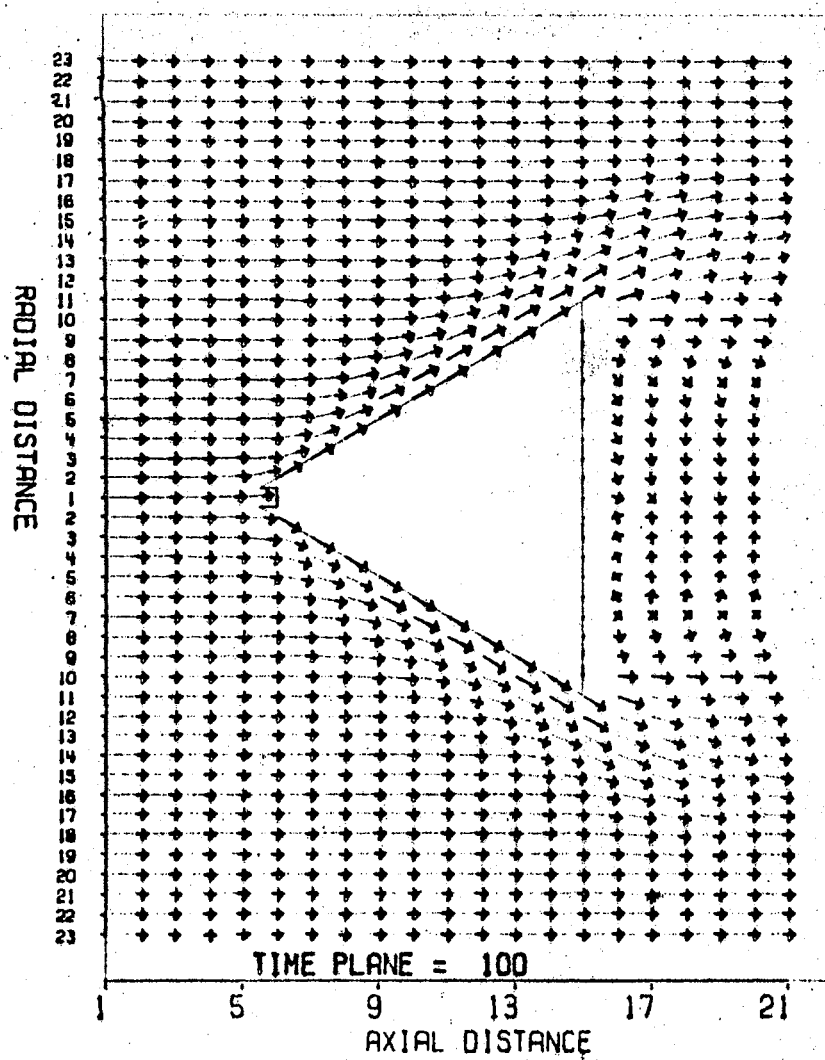


Figure 10. Windward/Leeward Velocity Vector Map,
 $M_{\infty} = 3.0$, $\alpha = 0^{\circ}$

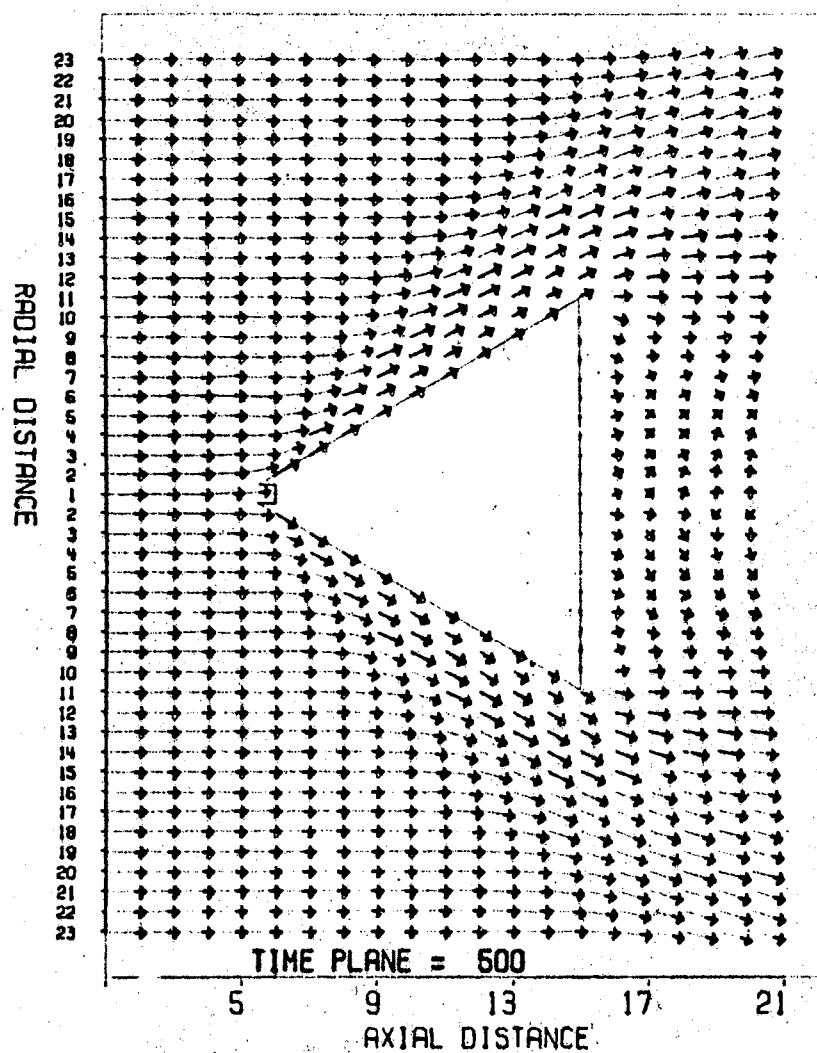


Figure 11. Windward/Leeward Velocity Vector Map,
 $M_{\infty} = 3.0$, $\alpha = 0^{\circ}$

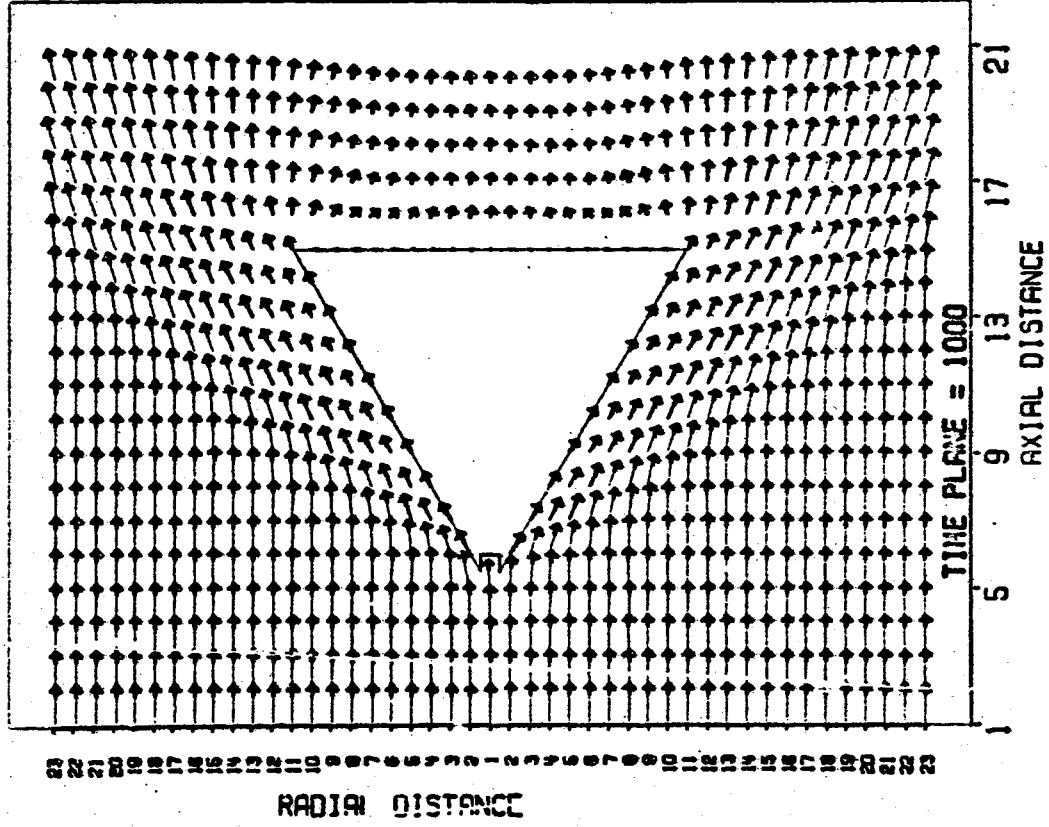


Figure 12. Windward/Leeward Velocity Vector Map,
 $M_\infty = 3.0$, $\alpha = 0^\circ$

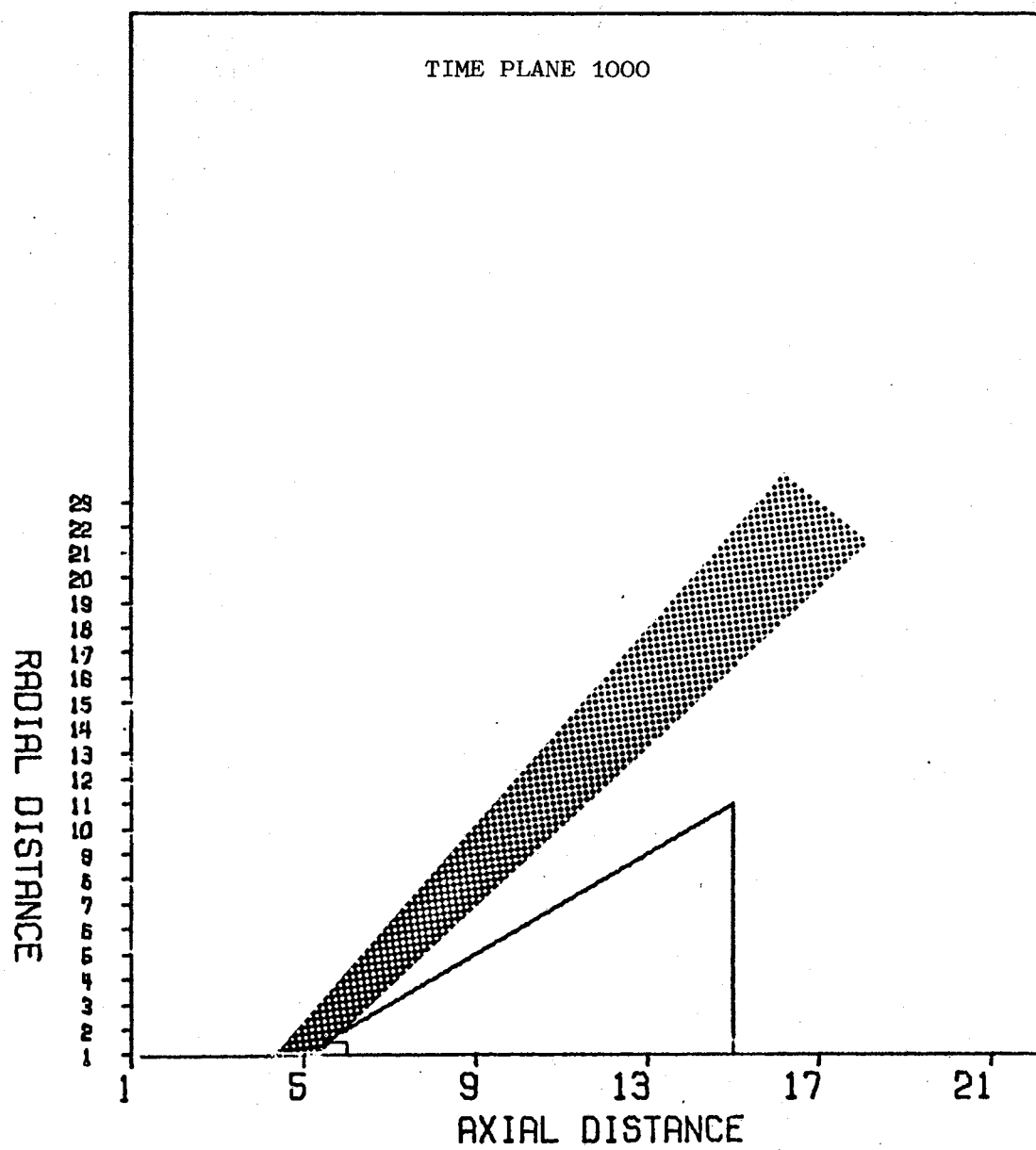


Figure 13. Wave Position from Velocity Map Microfilm, $\alpha = 0^\circ$

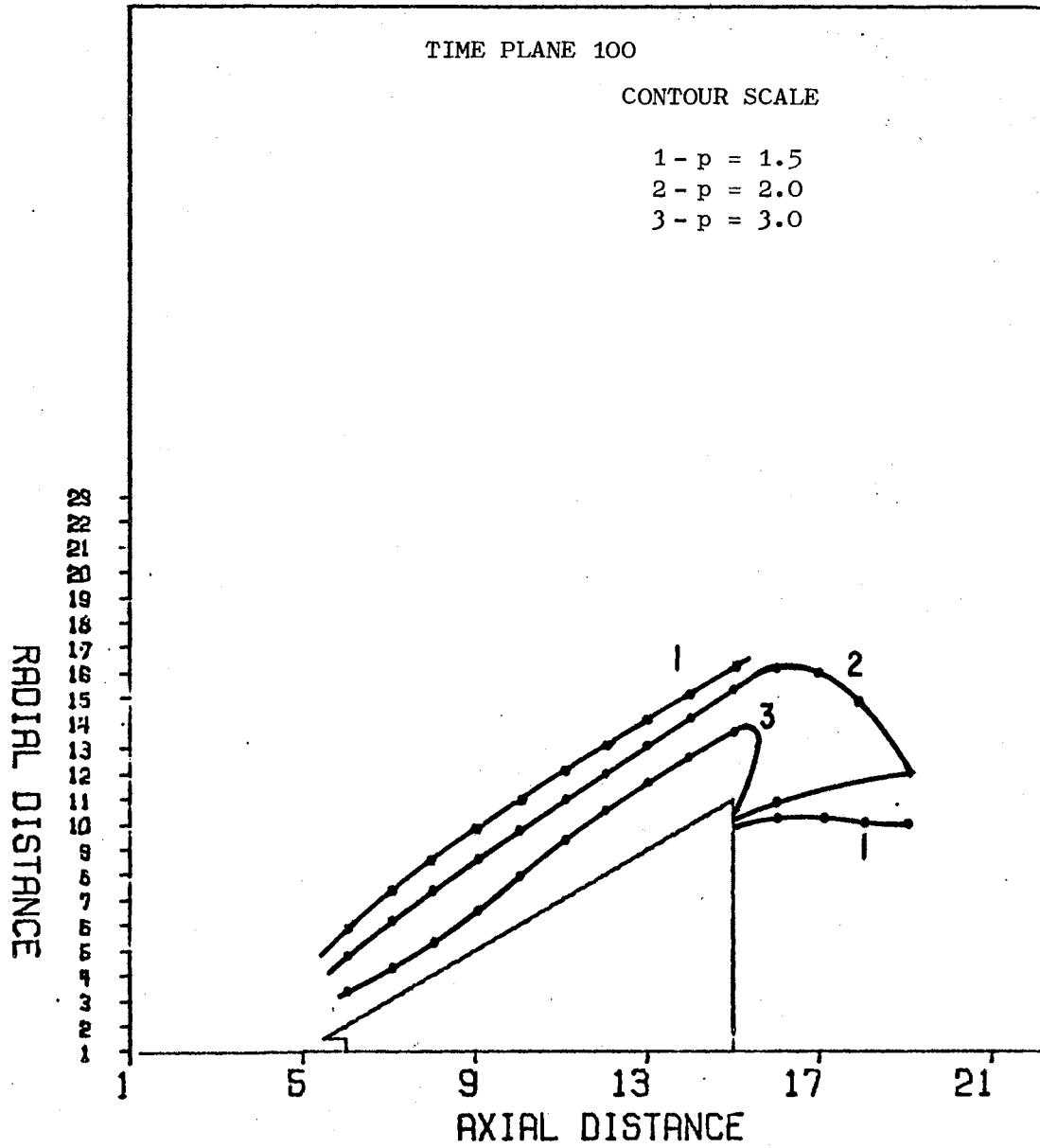


Figure 14. Pressure Profiles, $M_{\infty} = 3.0$, $\alpha = 0^\circ$

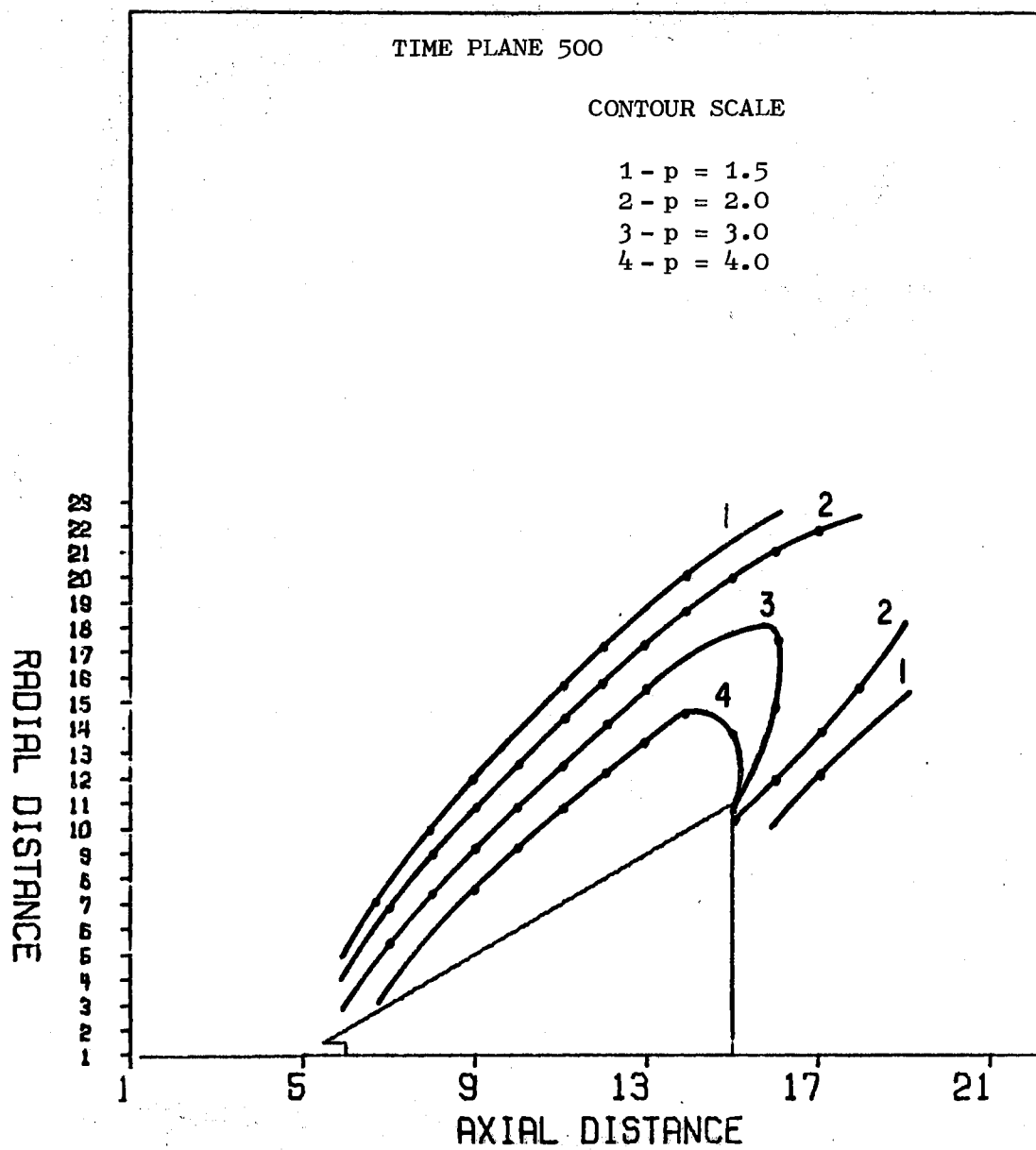


Figure 15. Pressure Profiles, $M_\infty = 3.0$, $\alpha = 0^\circ$

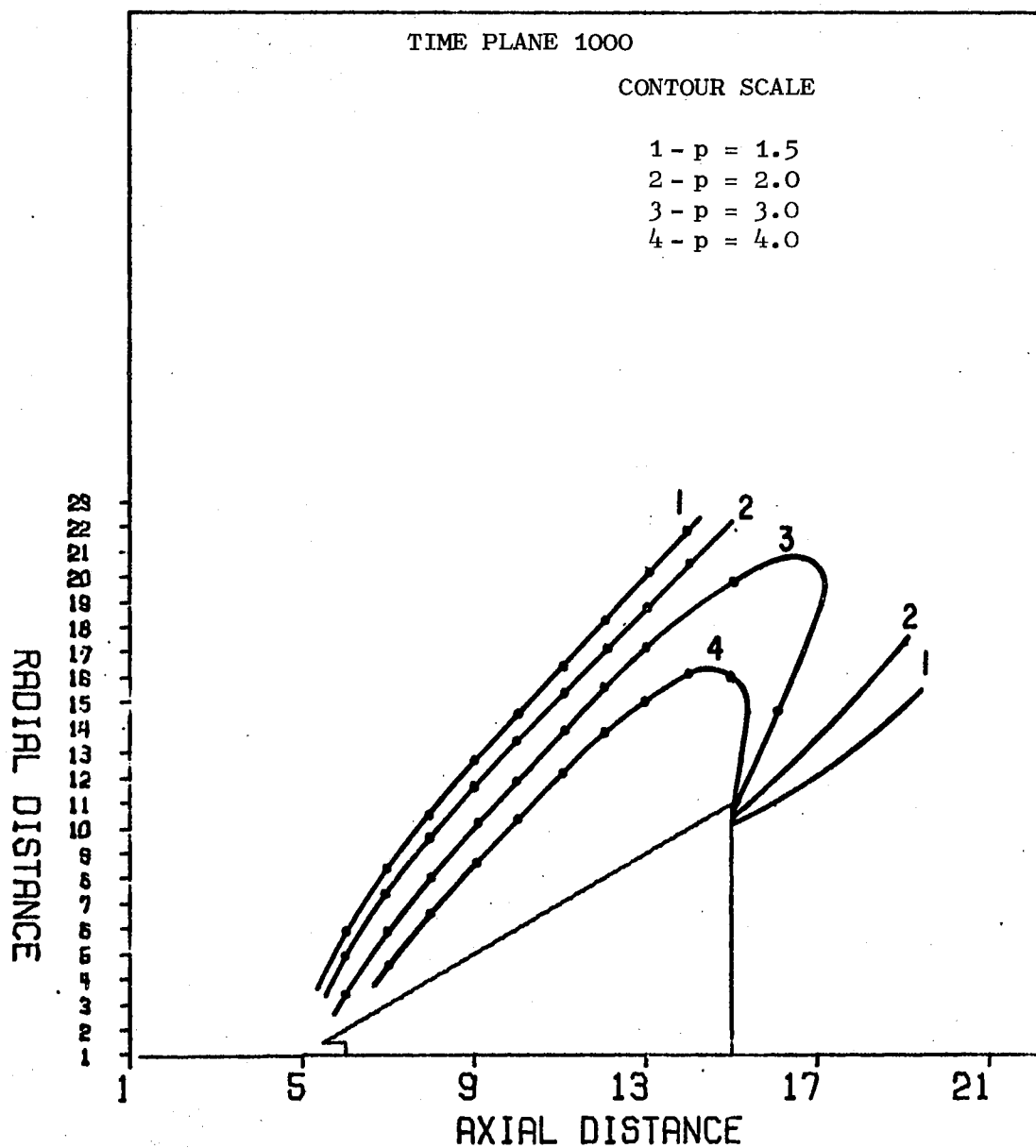


Figure 16. Pressure Profiles, $M_\infty = 3.0$, $\alpha = 0^\circ$

real time interval in seconds between initial immersion of the body in the flow and 1000 time planes is dependent on the ambient atmospheric conditions and the characteristic length of the body. The nondimensional time (t') at 1000 time planes was 9.356. The real time (t) from Equation (3-18) is given by:

$$t = \frac{t' H}{\sqrt{\frac{p_{\infty}}{\rho_{\infty}}}} ; \quad (5-1)$$

where

$$H = 1 \text{ ft.}$$

$$\rho_{\infty} = .002378 \text{ slugs/ft}^3$$

$$p_{\infty} = 14.7 \text{ lbs/in}^2$$

For the case outlined above, the real time to time plane 1000 was:

$t = 9.9$ milliseconds. Figure 13 is an estimation of the shock wave position as determined from the microfilm computer output of the velocity vector map. The size of the 16mm microfilm frame caused the vector arrowheads to assume an unnatural importance when viewed in such small scale. Where arrowheads are in close proximity compared to the over-all field, a "wave" is apparent. It is this apparent wave position that appears in Figure 13.

Nonzero Angle of Attack Solutions

Three nonzero angle of attack solutions are presented; 10 degrees, 20 degrees, and 30 degrees. Summary results are presented herein for each of the three angles of attack. Specifically, the results presented are:

- (1) Windward/Leeward Plane Velocity Vector maps ($\theta = 0/180^\circ$);
- (2) Transverse Plane Velocity Vector Maps (midway on cone axis);
- (3) Pressure Profiles for $\theta = 0, 90$, and 180° .

Data for the $\alpha = 10^\circ$ solution is presented in Figures 17 through 28; for $\alpha = 20^\circ$ in Figures 29 through 40; and for $\alpha = 30^\circ$ in Figures 41 through 52.

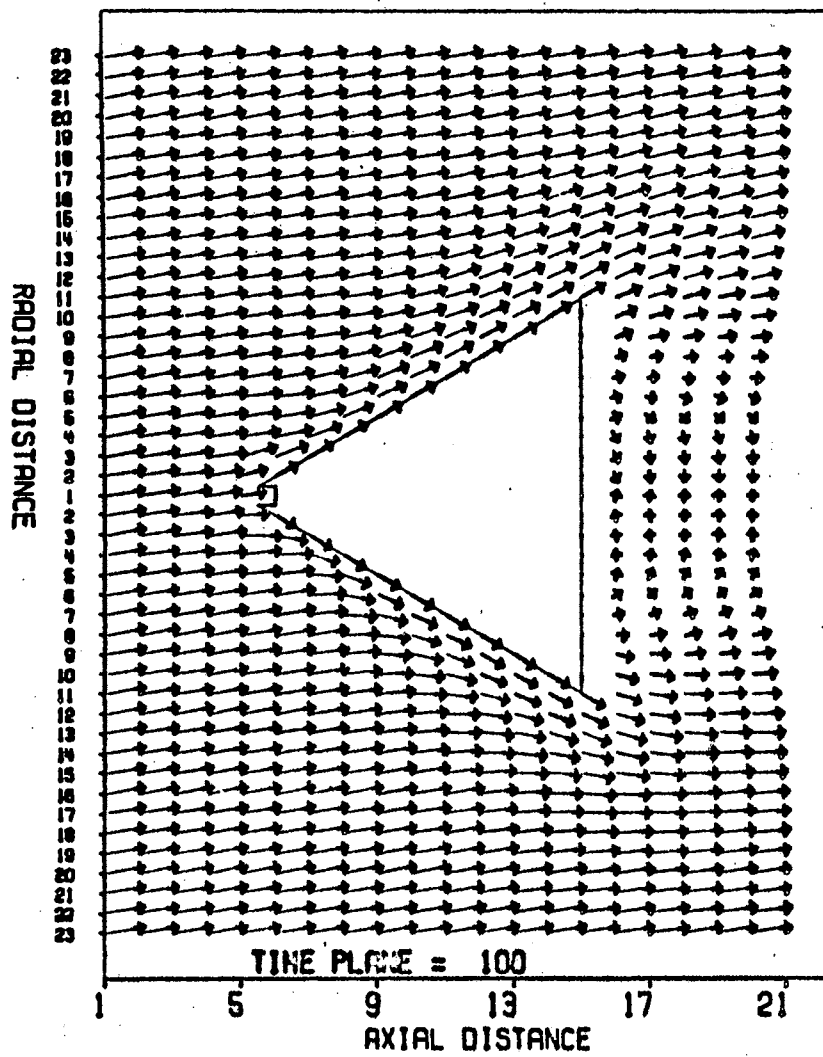


Figure 17. Windward/Leeward Velocity Vector Map,
 $M_{\infty} = 3.0$, $\alpha = 10^{\circ}$

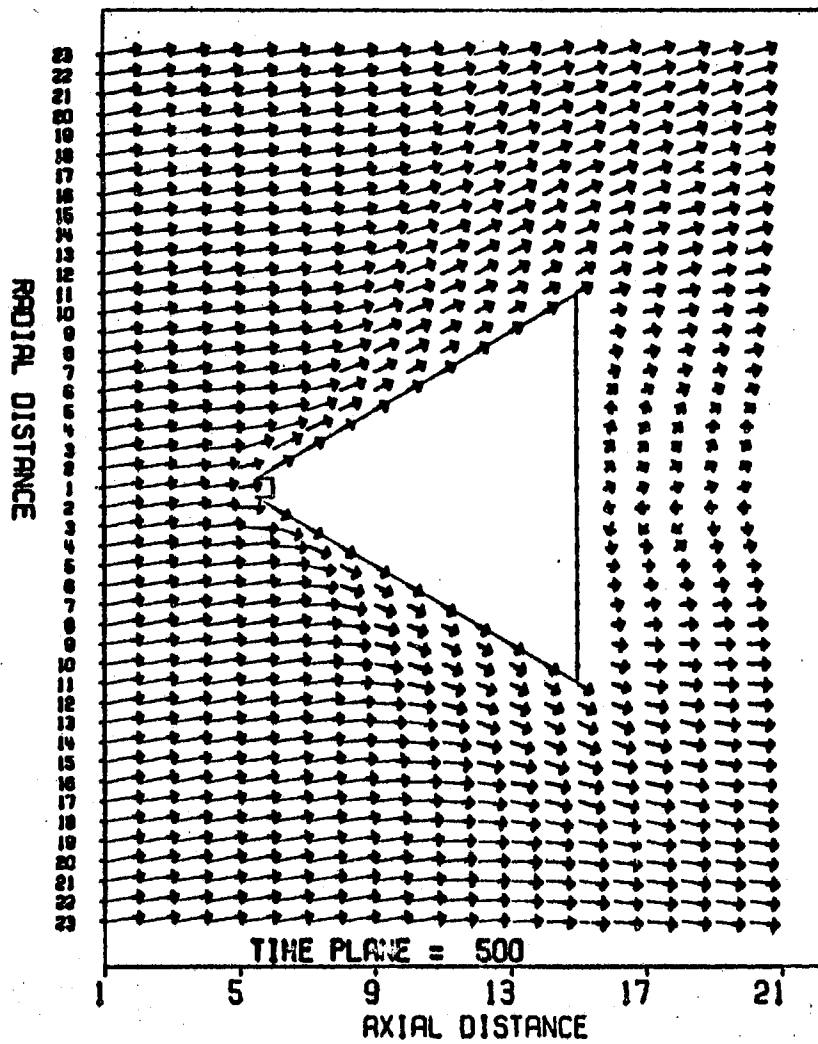


Figure 18. Windward/Leeward Velocity Vector Map,
 $M_{\infty} = 3.0$, $\alpha = 10^{\circ}$

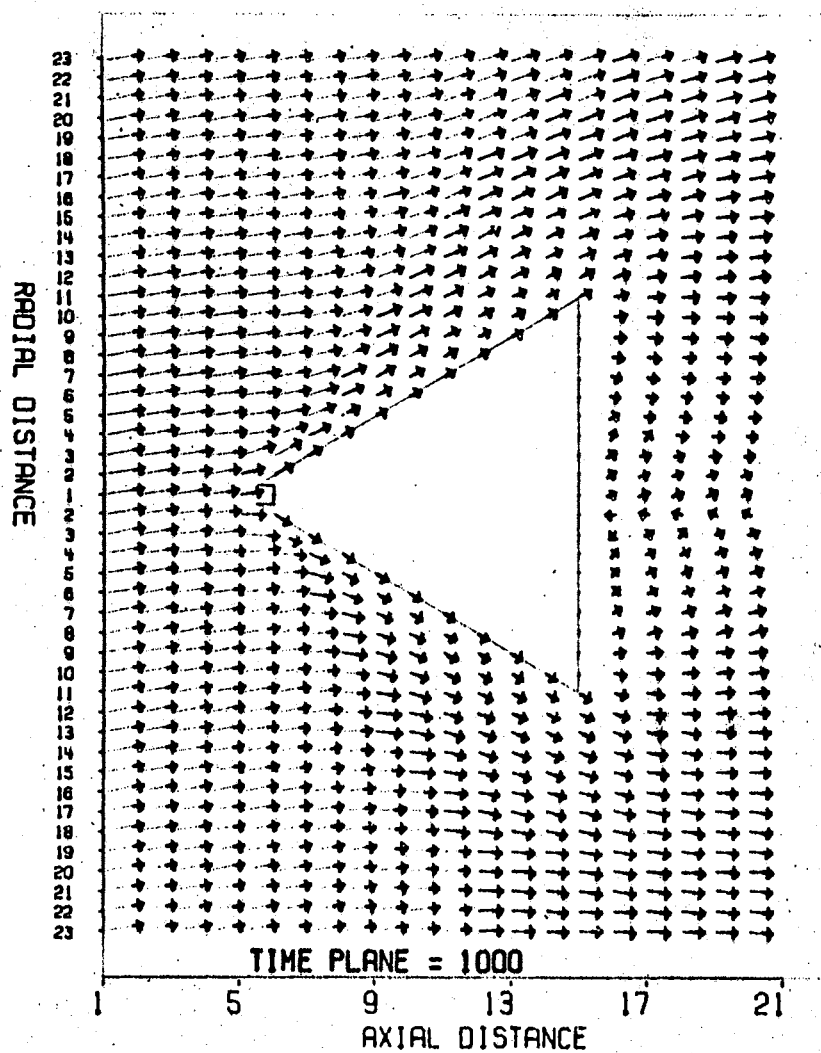


Figure 19. Windward/Leeward Velocity Vector Map,
 $M_{\infty} = 3.0$, $\alpha = 10^{\circ}$

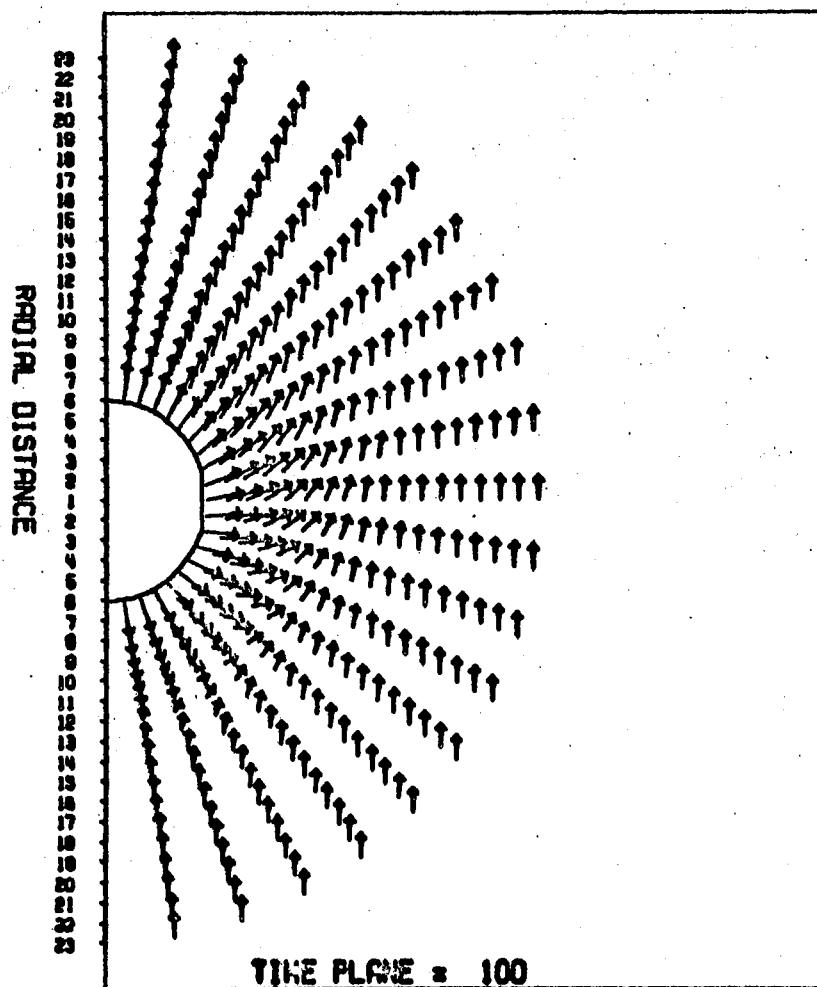


Figure 20. Transverse Velocity Vector Map,
 $M = 3.0$, $\alpha = 10^\circ$, $m = 10$
 (Midway on Cone Axis)

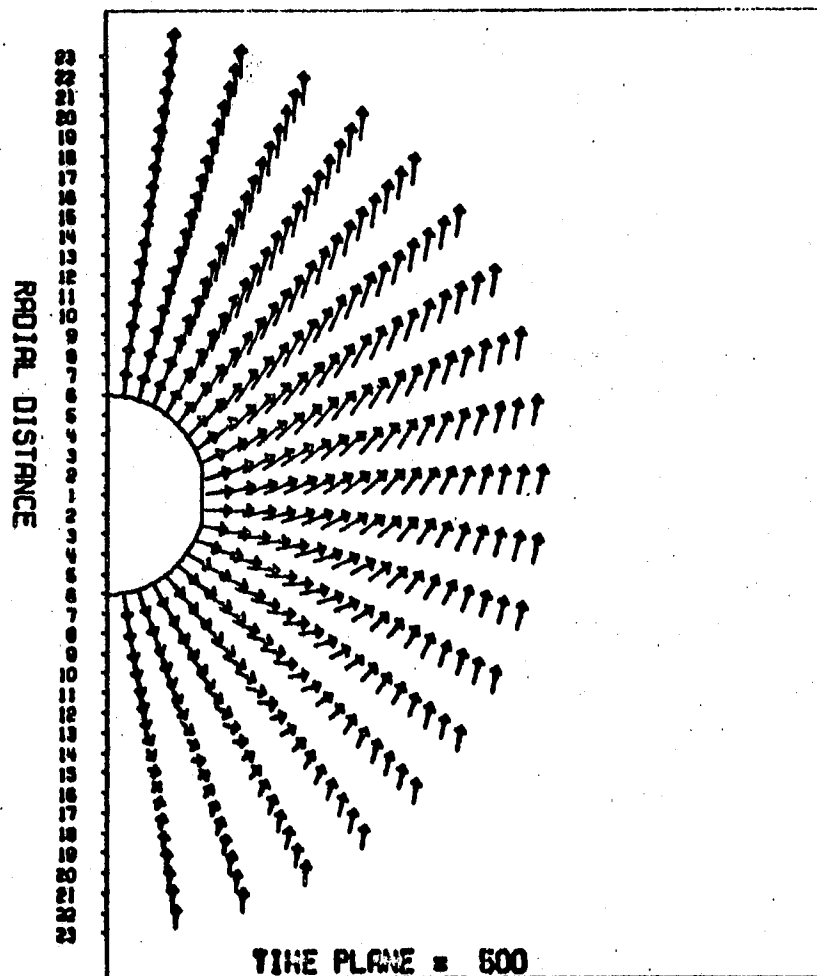


Figure 21. Transverse Velocity Vector Map,
 $M = 3.0$, $\alpha = 10^\circ$, $m = 10$
 (Midway on Cone Axis)

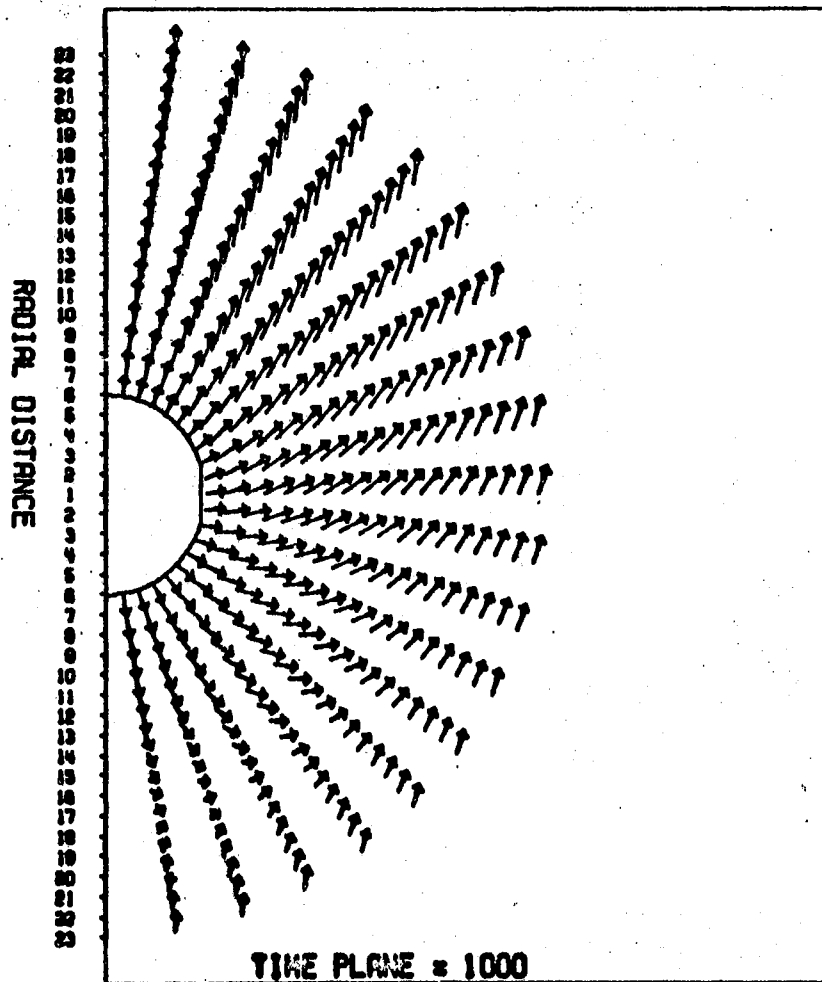


Figure 22. Transverse Velocity Vector Map,
 $M = 3.0$, $\alpha = 10^\circ$, $m = 10$
 (Midway on Cone Axis)

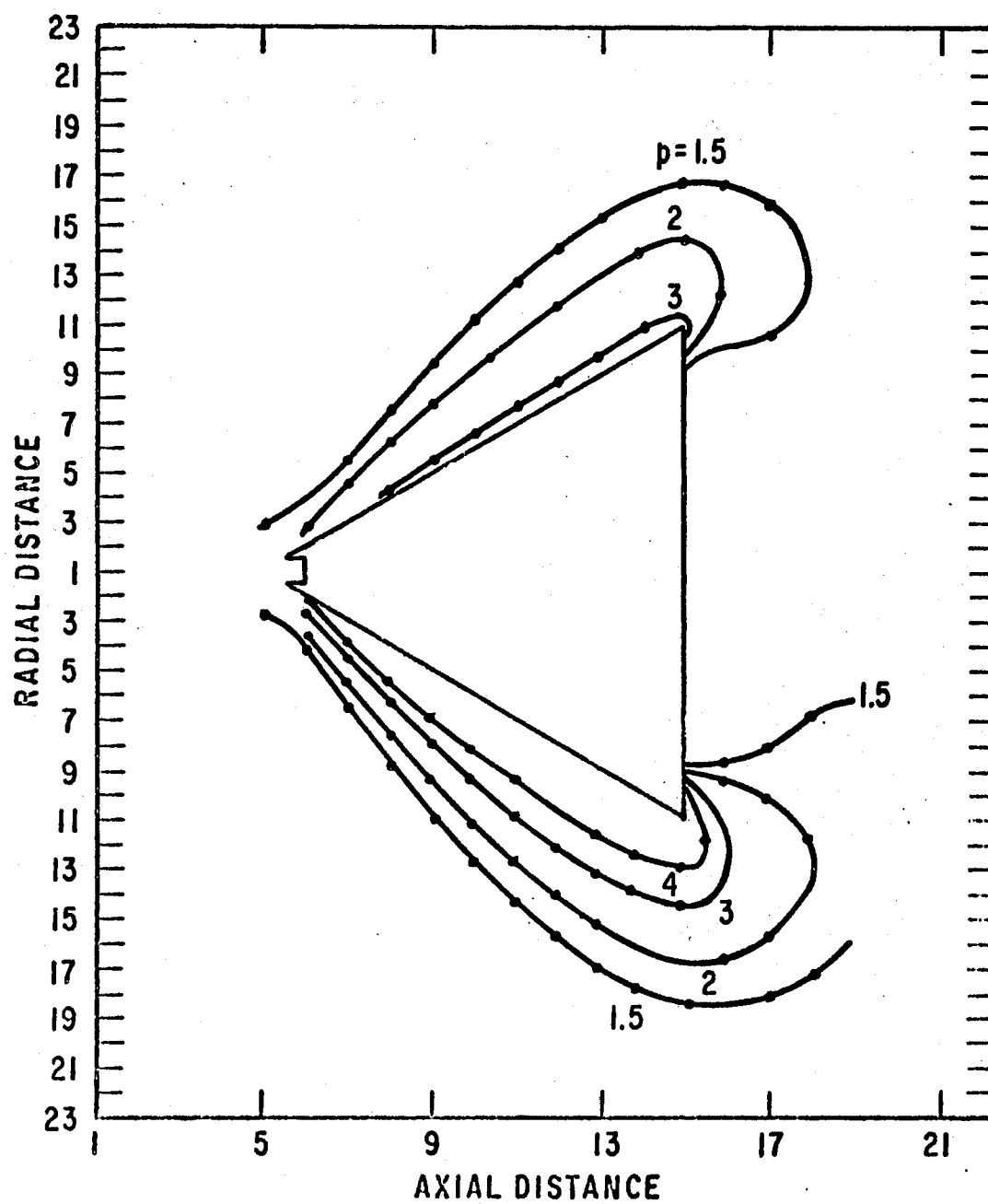


Figure 23. Pressure Profiles, $M_\infty = 3.0$, $\alpha = 10^\circ$, $\theta = 0^\circ, 180^\circ$

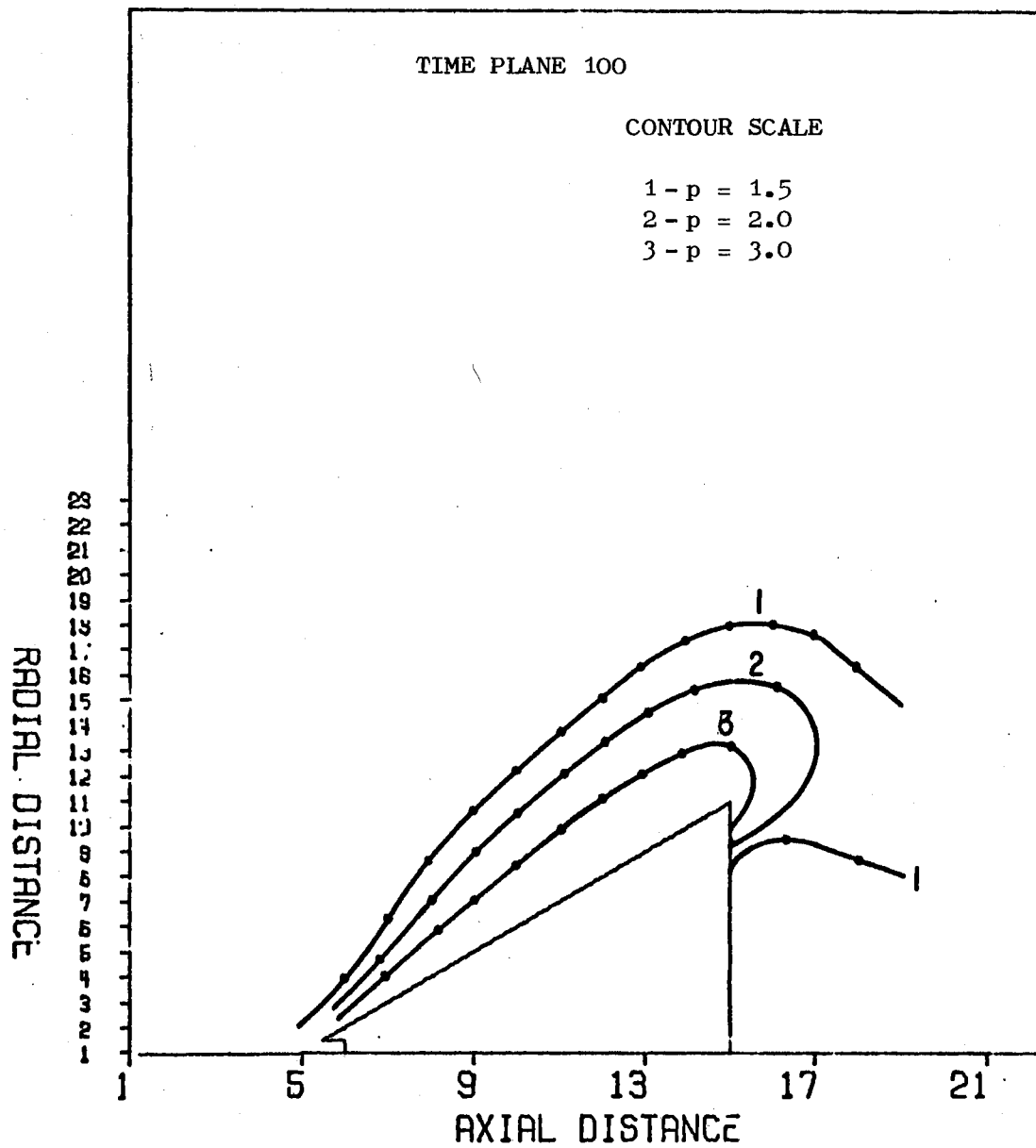


Figure 24. Pressure Profiles, $M_\infty = 3.0$, $\alpha = 10^\circ$, $\theta = 90^\circ$

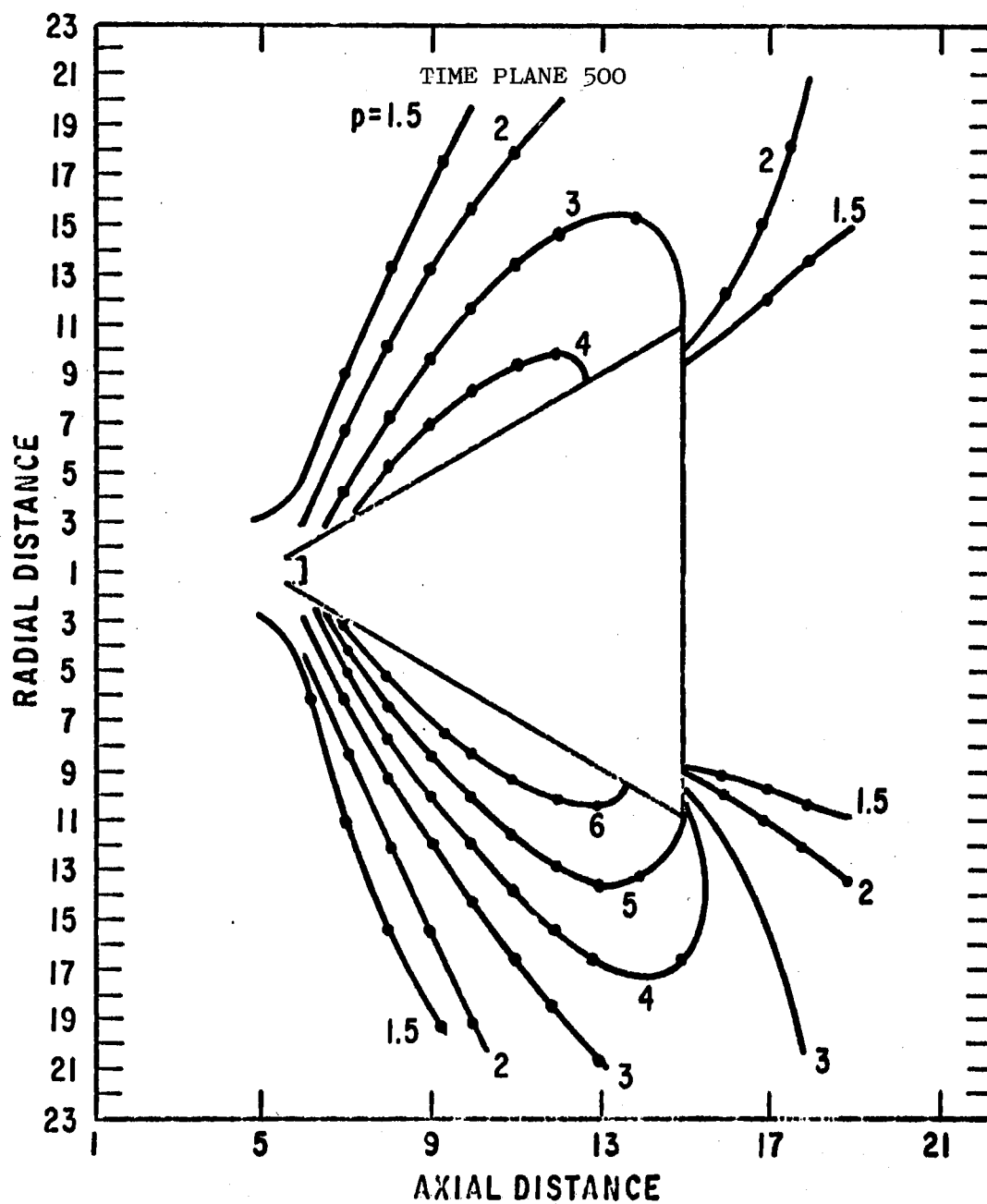


Figure 25. Pressure Profiles, $M_\infty = 3.0$, $\alpha = 10^\circ$, $\theta = 0^\circ, 180^\circ$

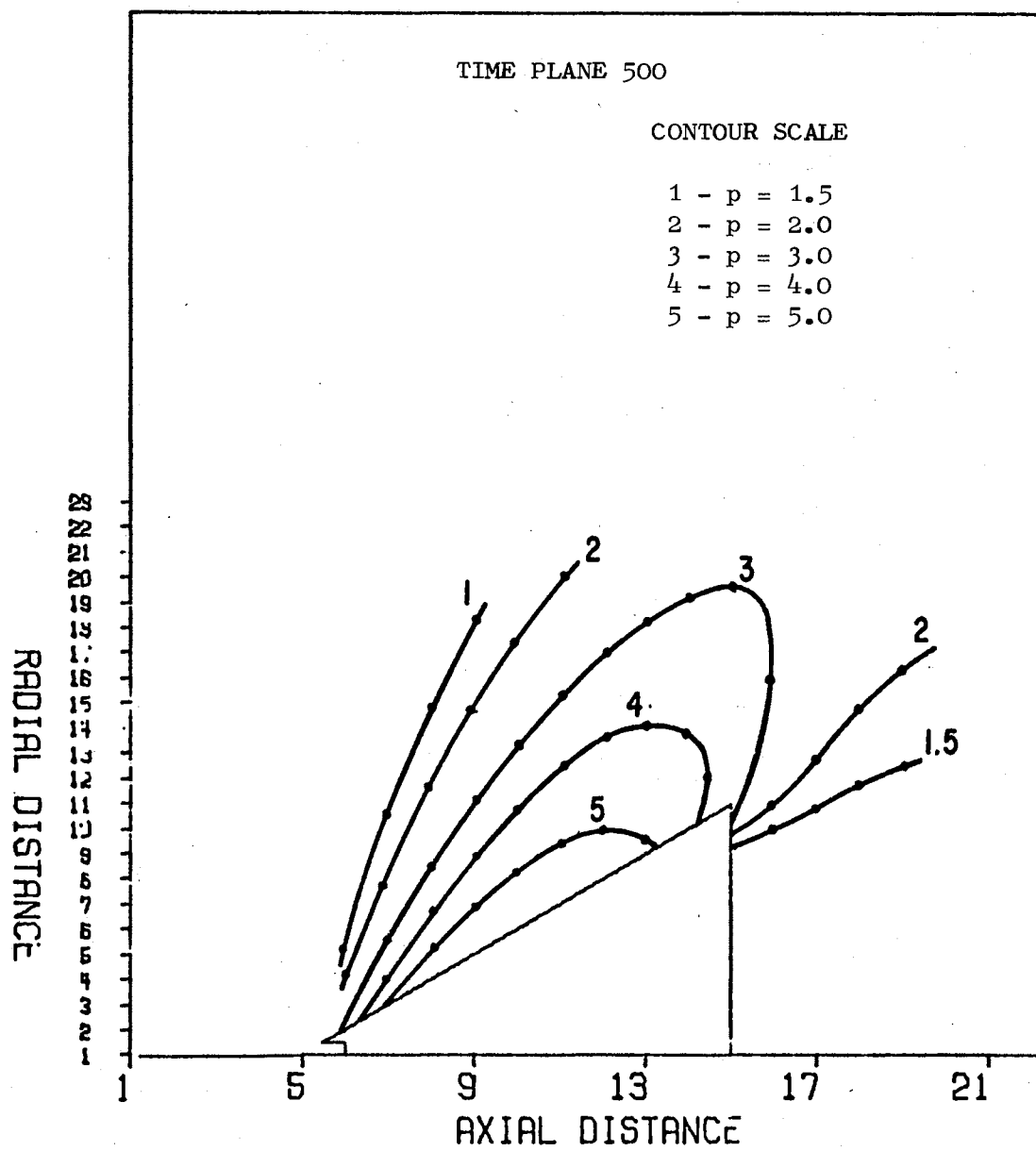


Figure 26. Pressure Profiles, $M_\infty = 3.0$, $\alpha = 10^\circ$, $\theta = 90^\circ$

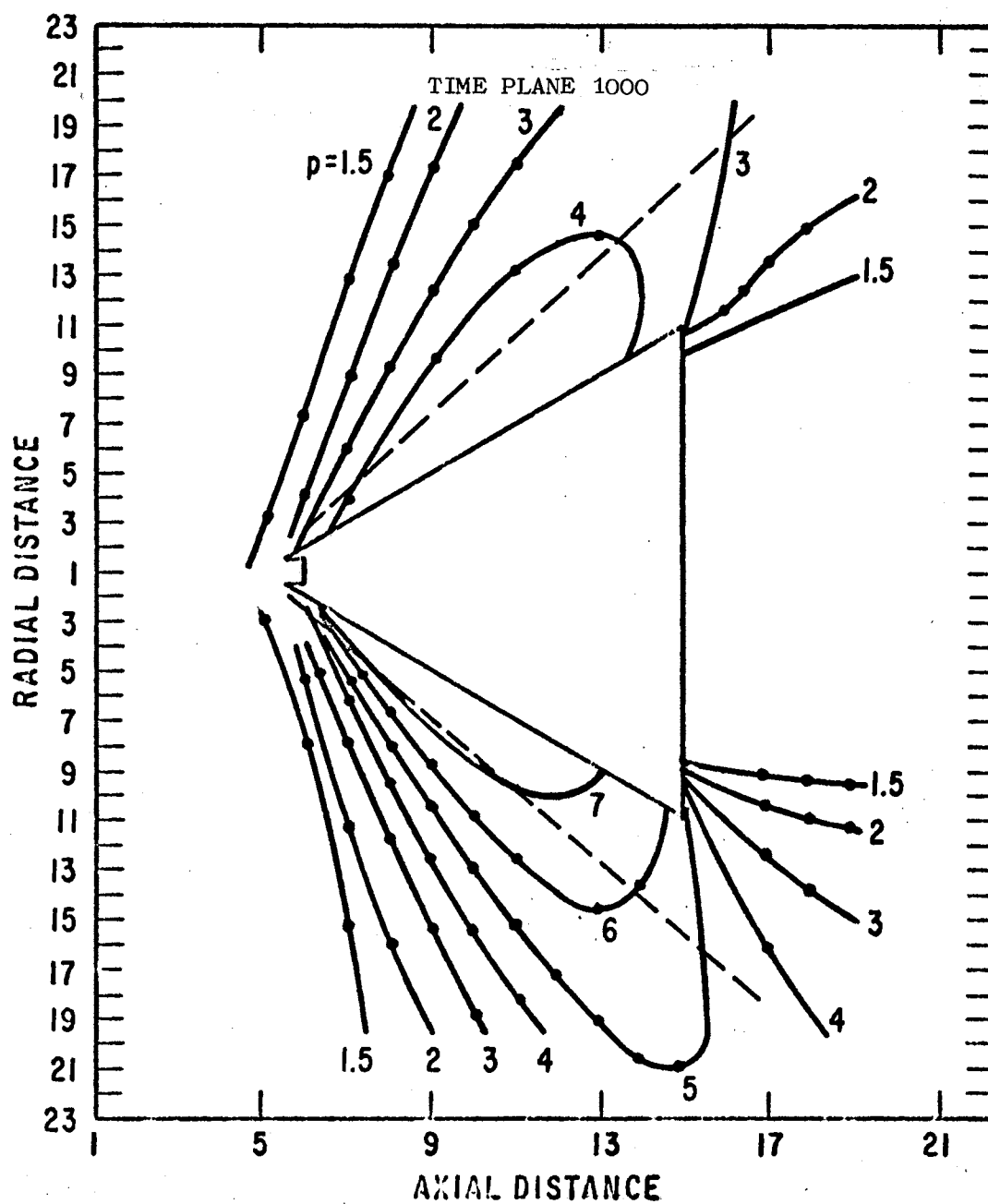


Figure 27. Pressure Profiles, $M_\infty = 3.0$, $\alpha = 10^\circ$, $\theta = 0^\circ, 180^\circ$

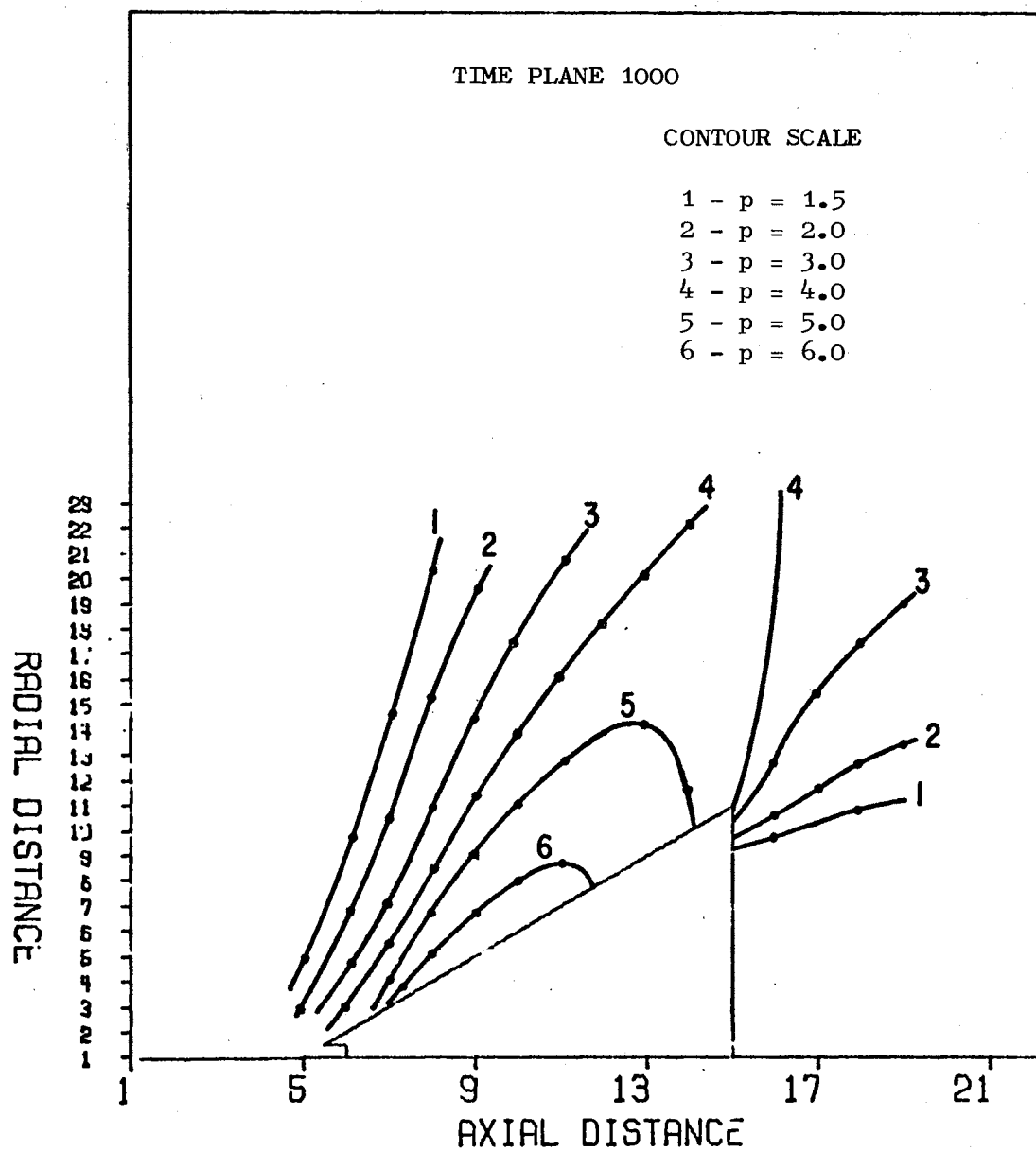


Figure 28. Pressure Profiles, $M_\infty = 3.0$, $\alpha = 10^\circ$, $\theta = 90^\circ$

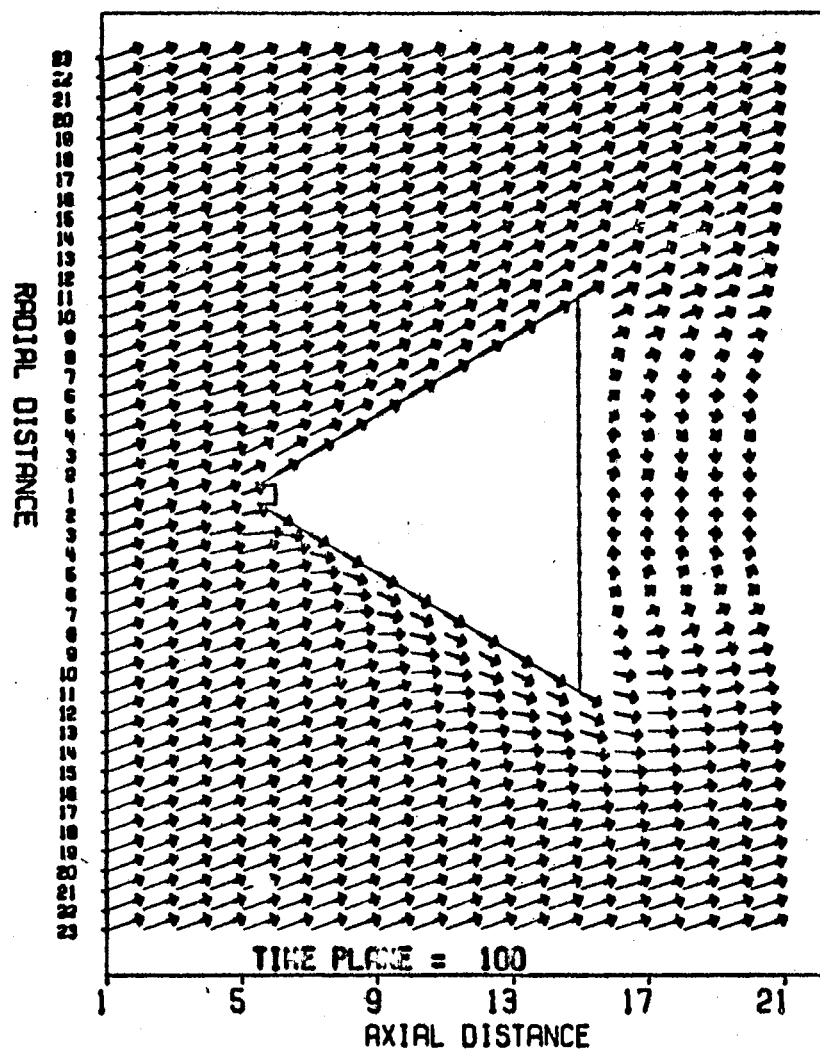


Figure 29. Windward/Leeward Velocity Vector Map;
 $M_{\infty} = 3.0$, $\alpha = 20^{\circ}$

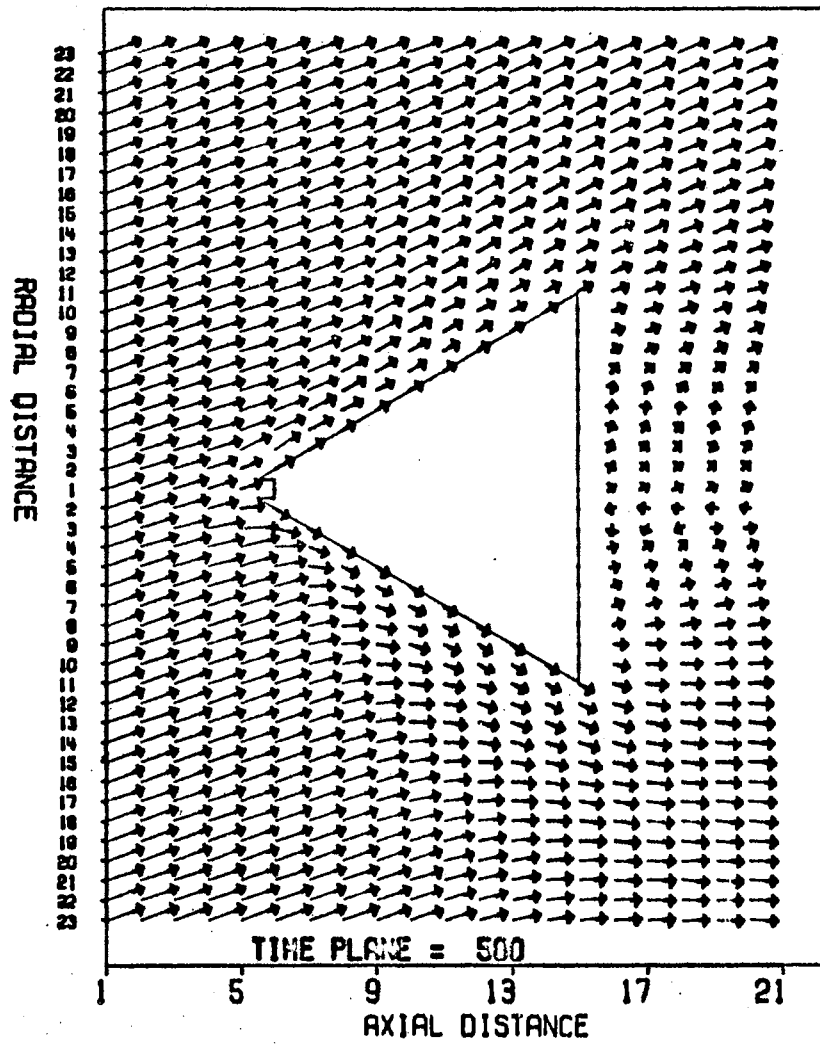


Figure 30. Windward/Leeward Velocity Vector Map,
 $M_{\infty} = 3.0$, $\alpha = 20^{\circ}$

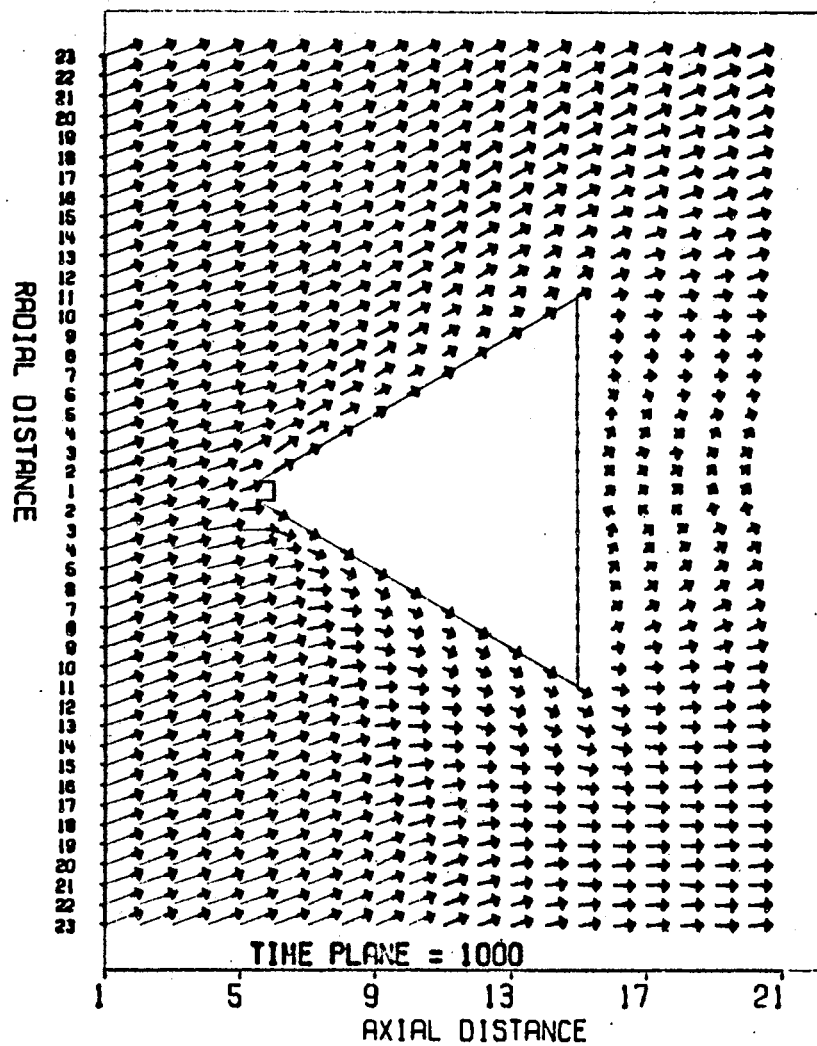


Figure 31. Windward/Leeward Velocity Vector Map,
 $M_{\infty} = 3.0$, $\alpha = 20^{\circ}$

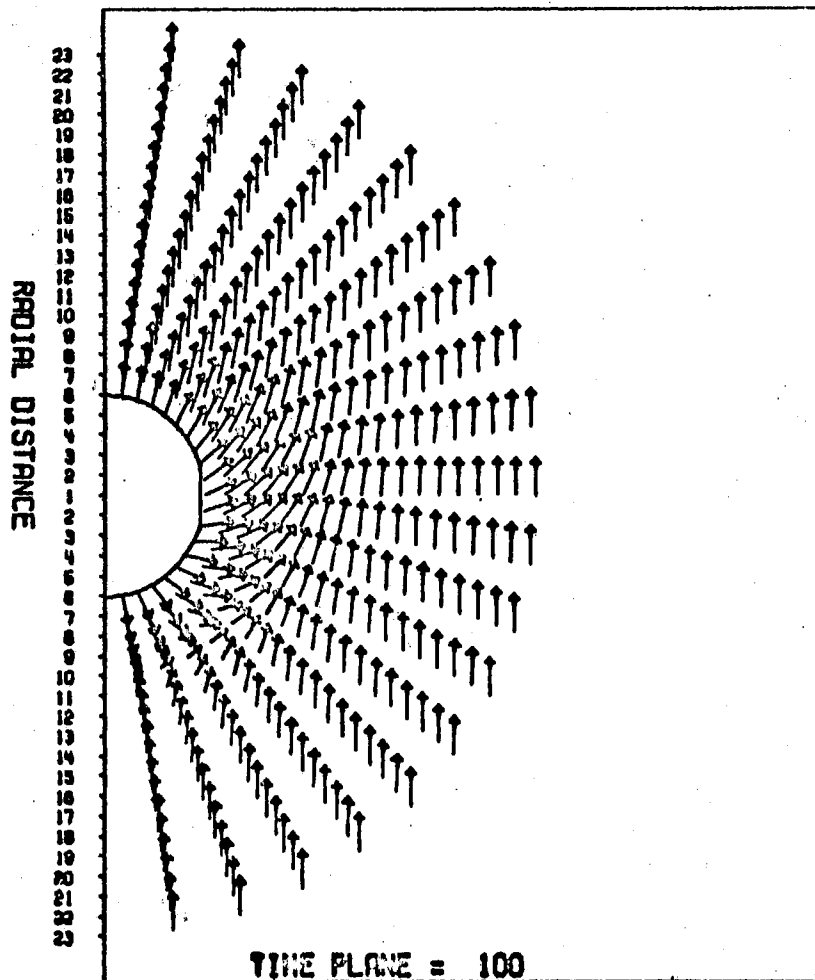


Figure 32. Transverse Velocity Vector Map, $M = 3.0$,
 $\alpha = 20^\circ$, $m = 10$ (Midway on Cone Axis)

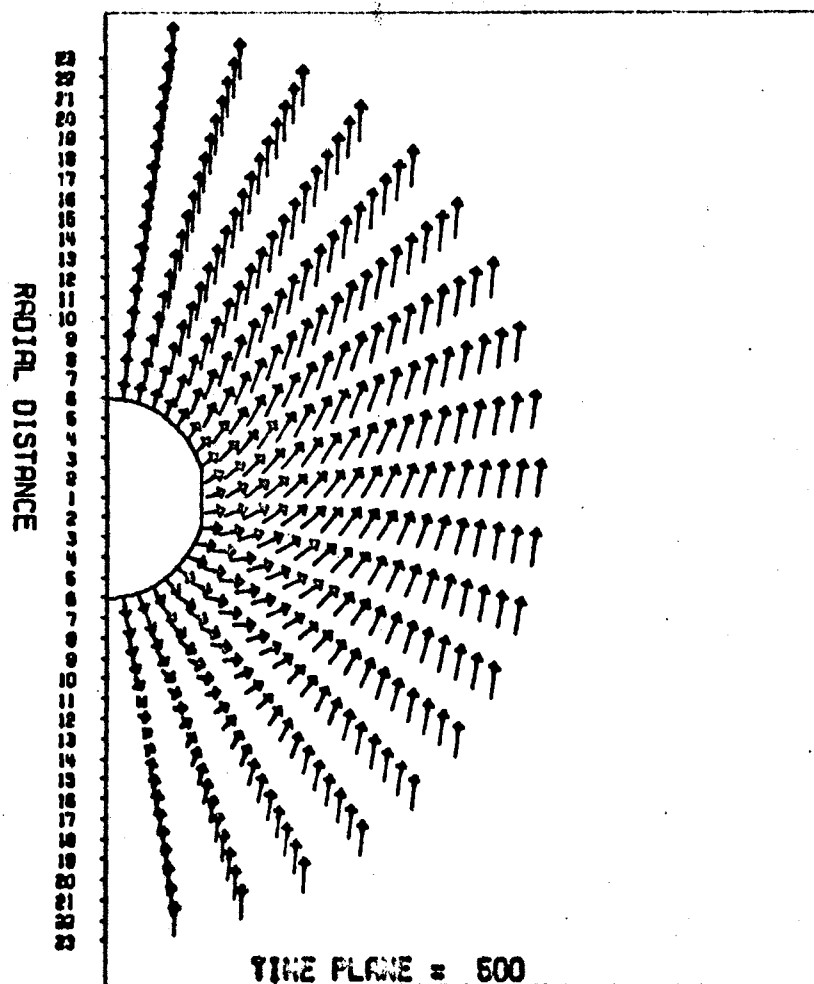


Figure 33. Transverse Velocity Vector Map,
 $M = 3.0$, $\alpha = 20^\circ$, $m = 10$
 (Midway on Cone Axis)

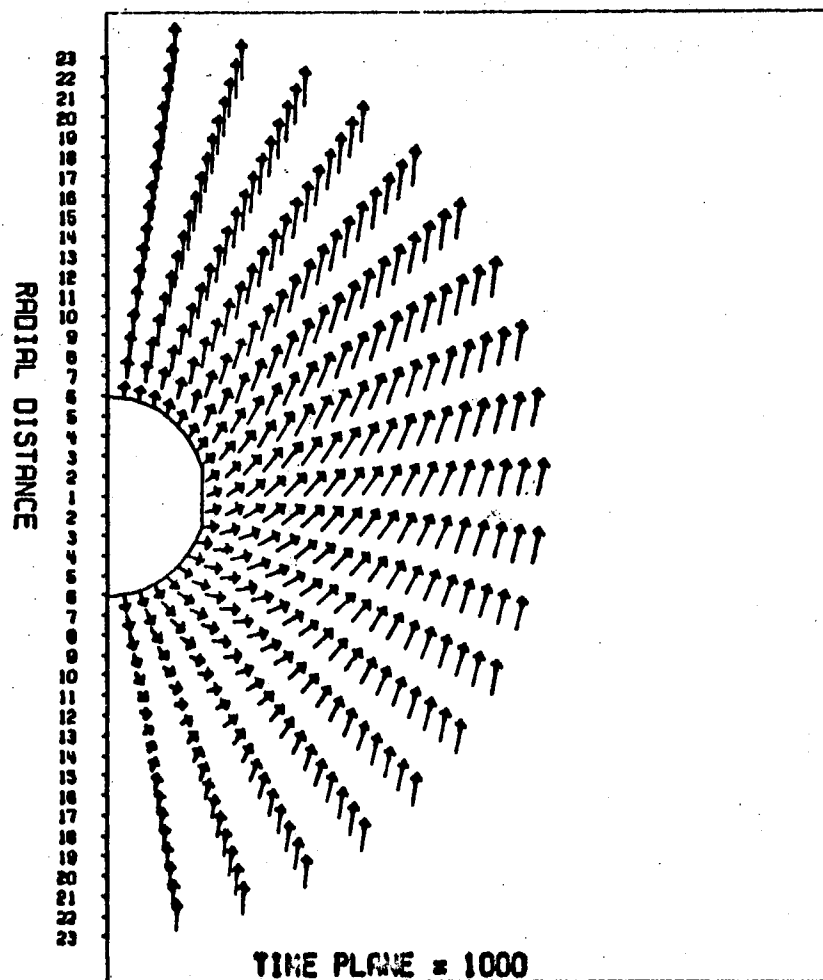


Figure 34. Transverse Velocity Vector Map,
 $M = 3.0$, $\alpha = 20^\circ$, $m = 10$
 (Midway on Cone Axis)

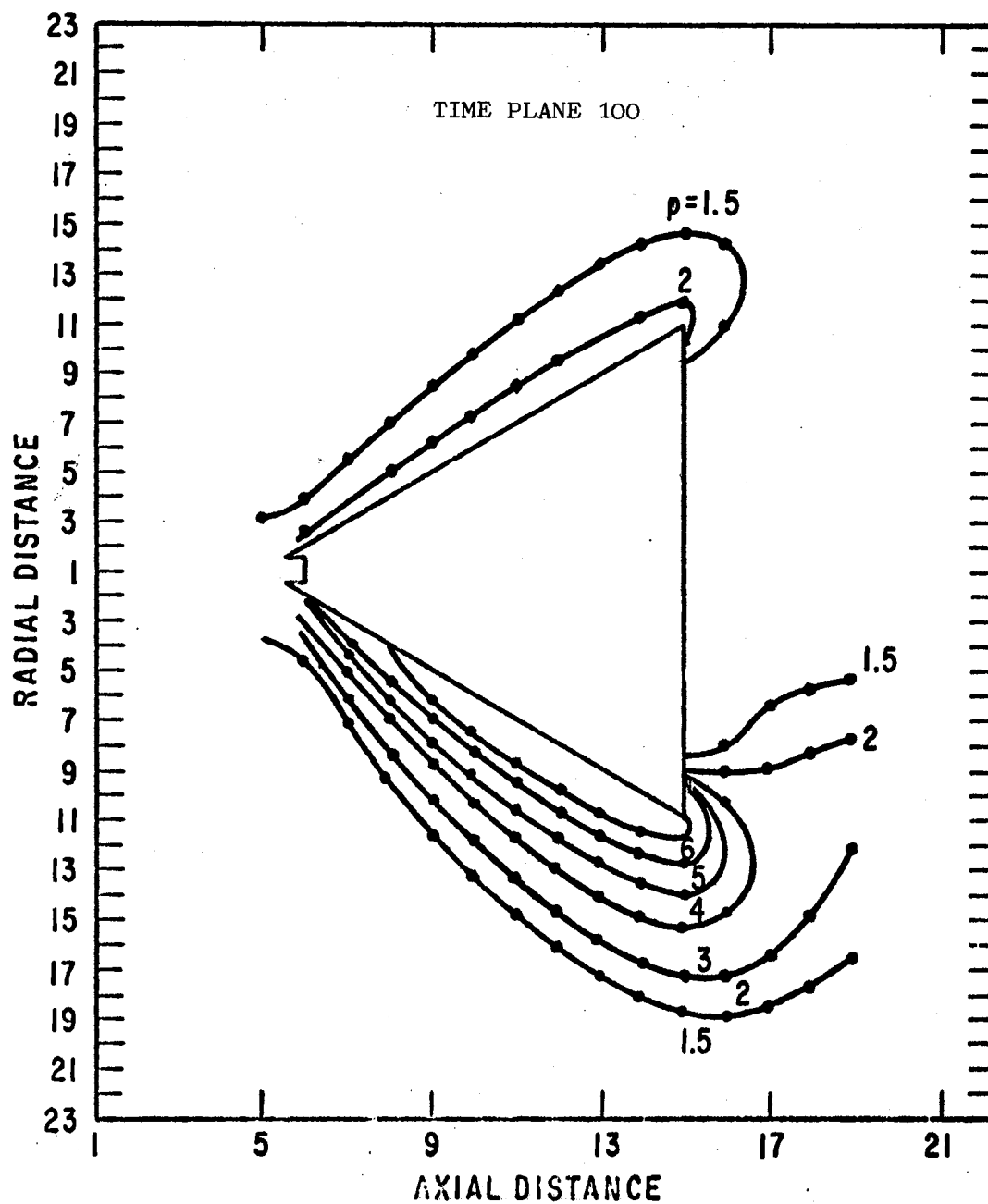


Figure 35. Pressure Profiles, $M_\infty = 3.0$, $\alpha = 20^\circ$, $\theta = 0^\circ, 180^\circ$

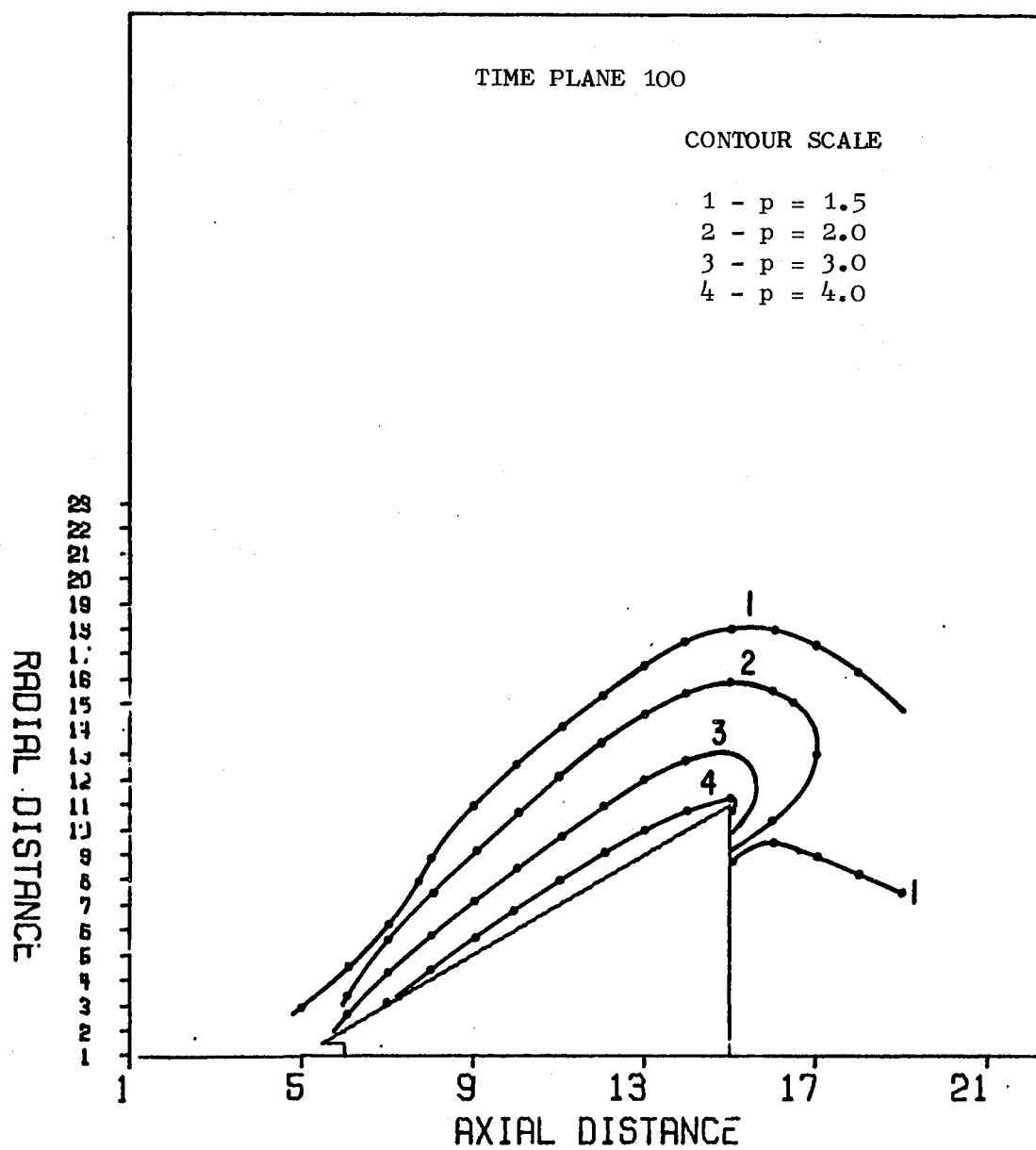


Figure 36. Pressure Profiles, $M_\infty = 3.0$, $\alpha = 20^\circ$, $\theta = 90^\circ$

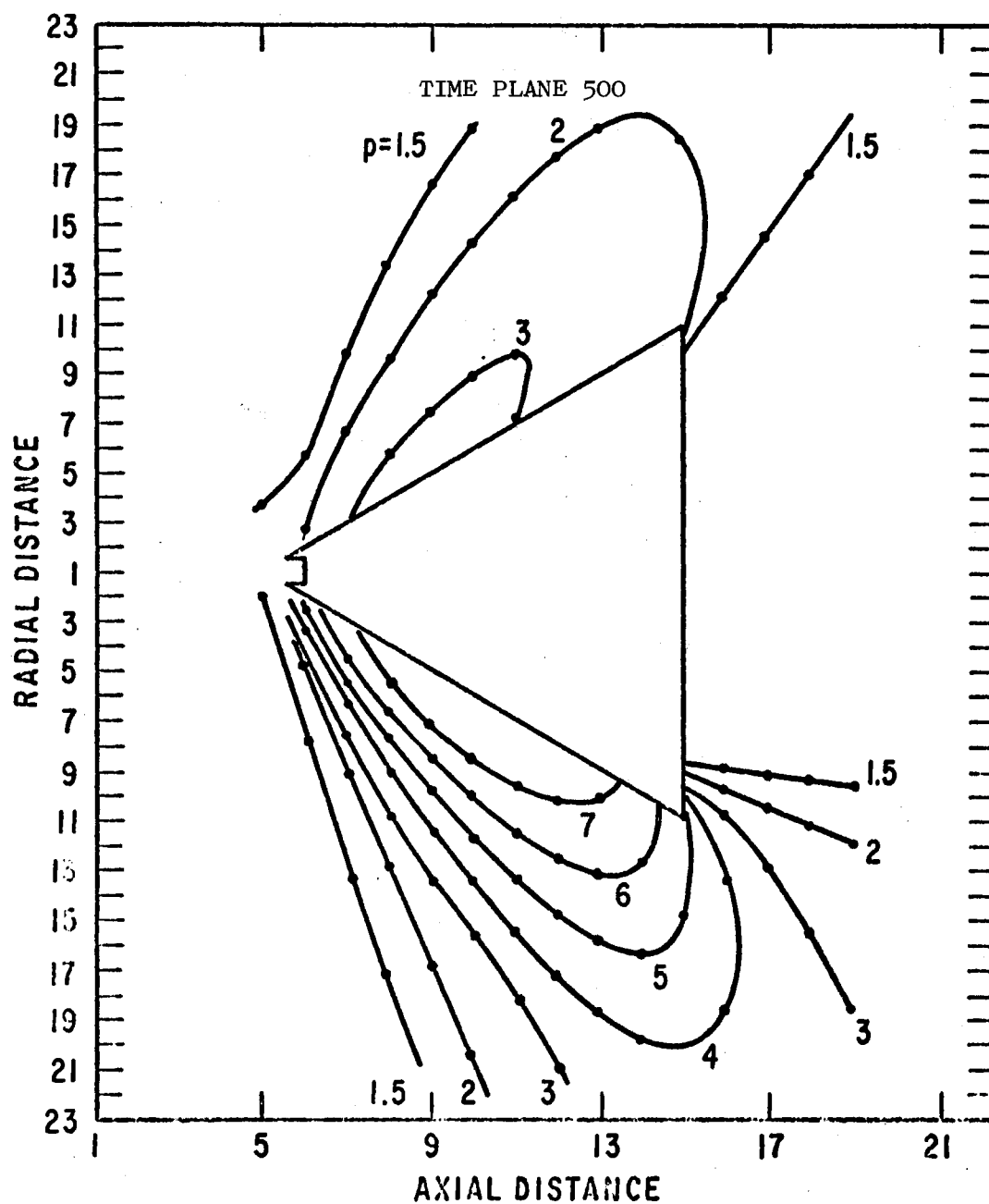


Figure 37. Pressure Profiles, $M_{\infty} = 3.0$, $\alpha = 20^{\circ}$, $\theta = 0^{\circ}, 180^{\circ}$

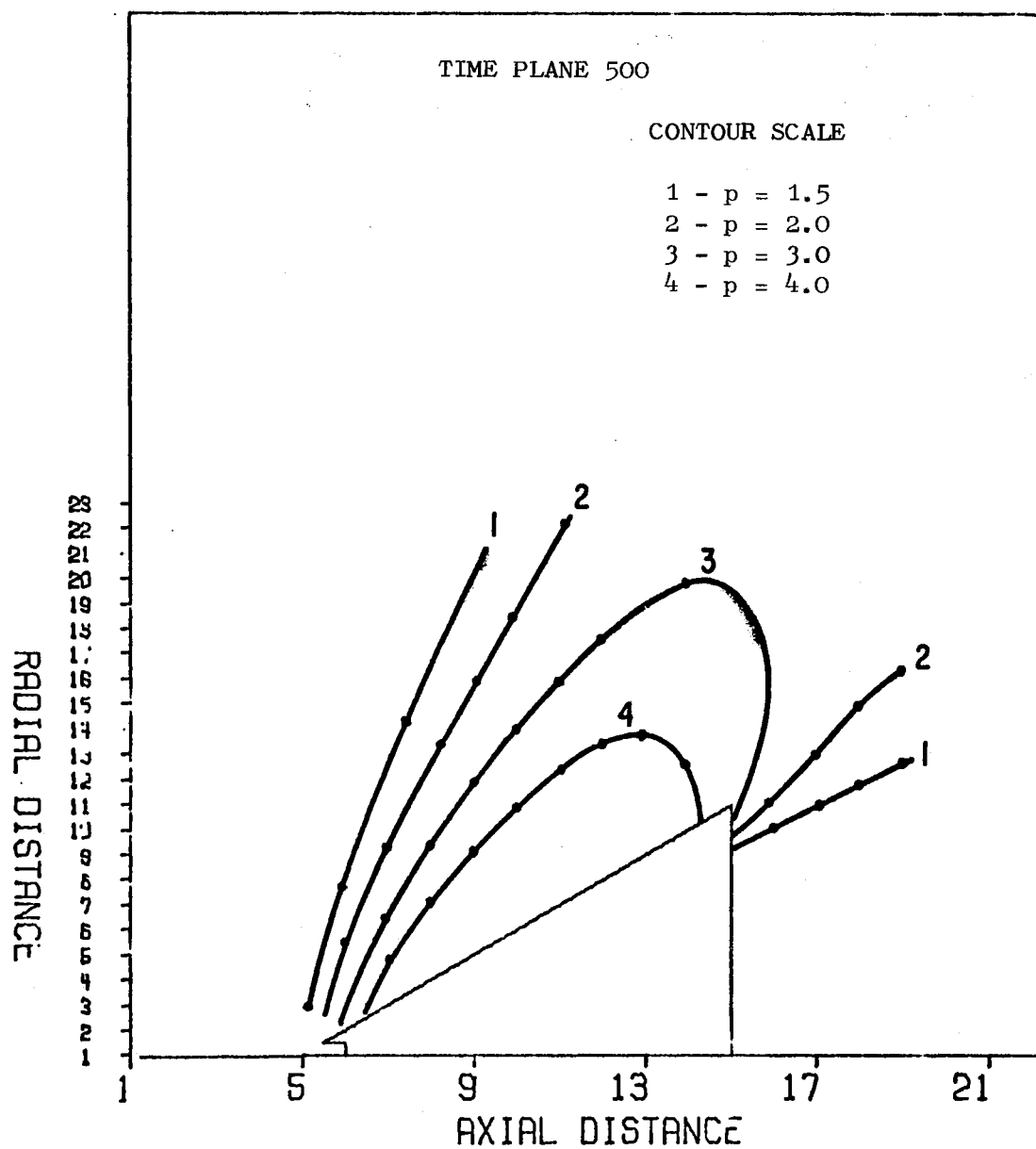


Figure 38. Pressure Profiles, $M_\infty = 3.0$, $\alpha = 20^\circ$,
 $\theta = 0^\circ, 180^\circ$

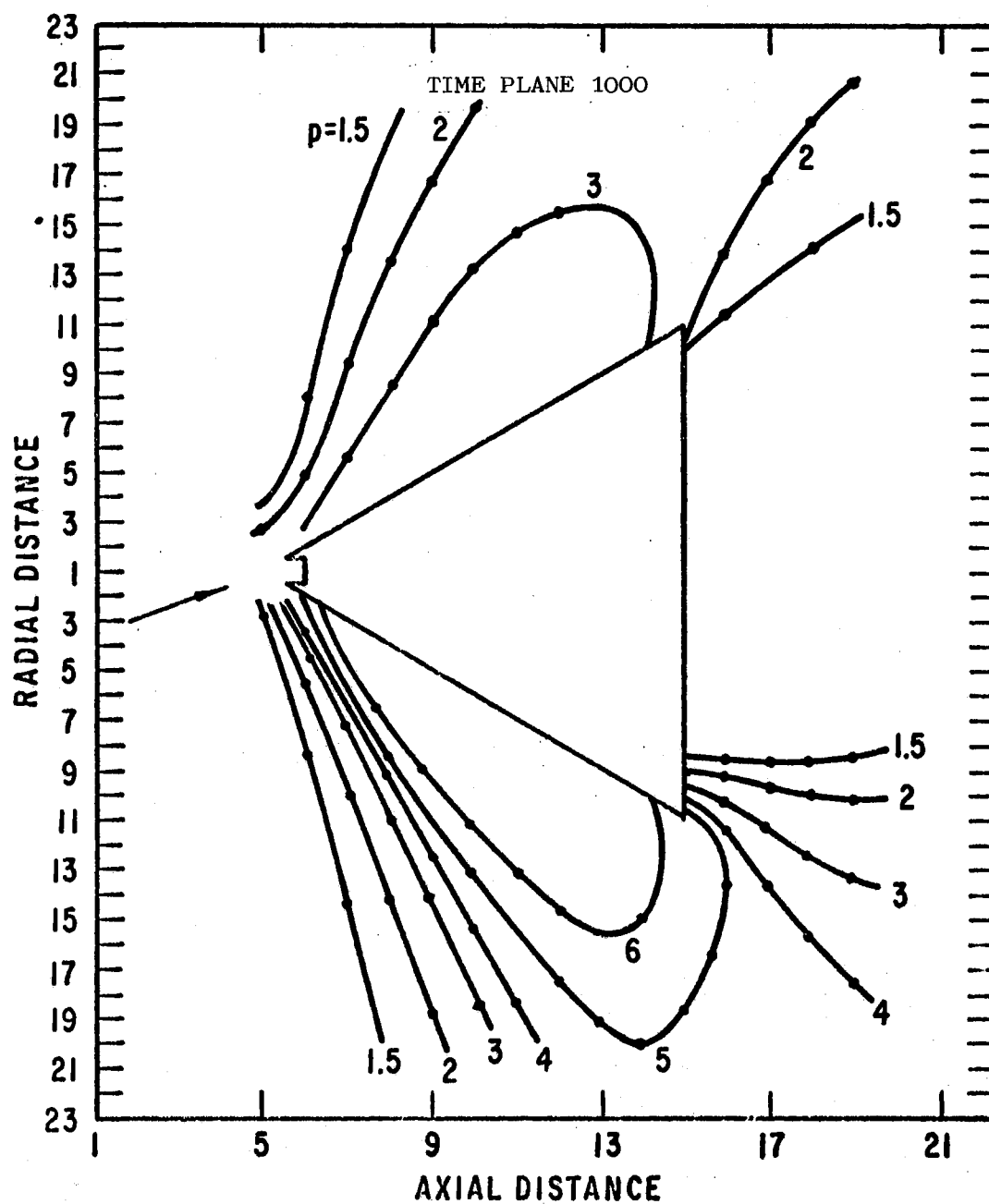


Figure 39. Pressure Profiles, $M_{\infty} = 3.0$, $\alpha = 20^{\circ}$,
 $\theta = 0^{\circ}, 180^{\circ}$

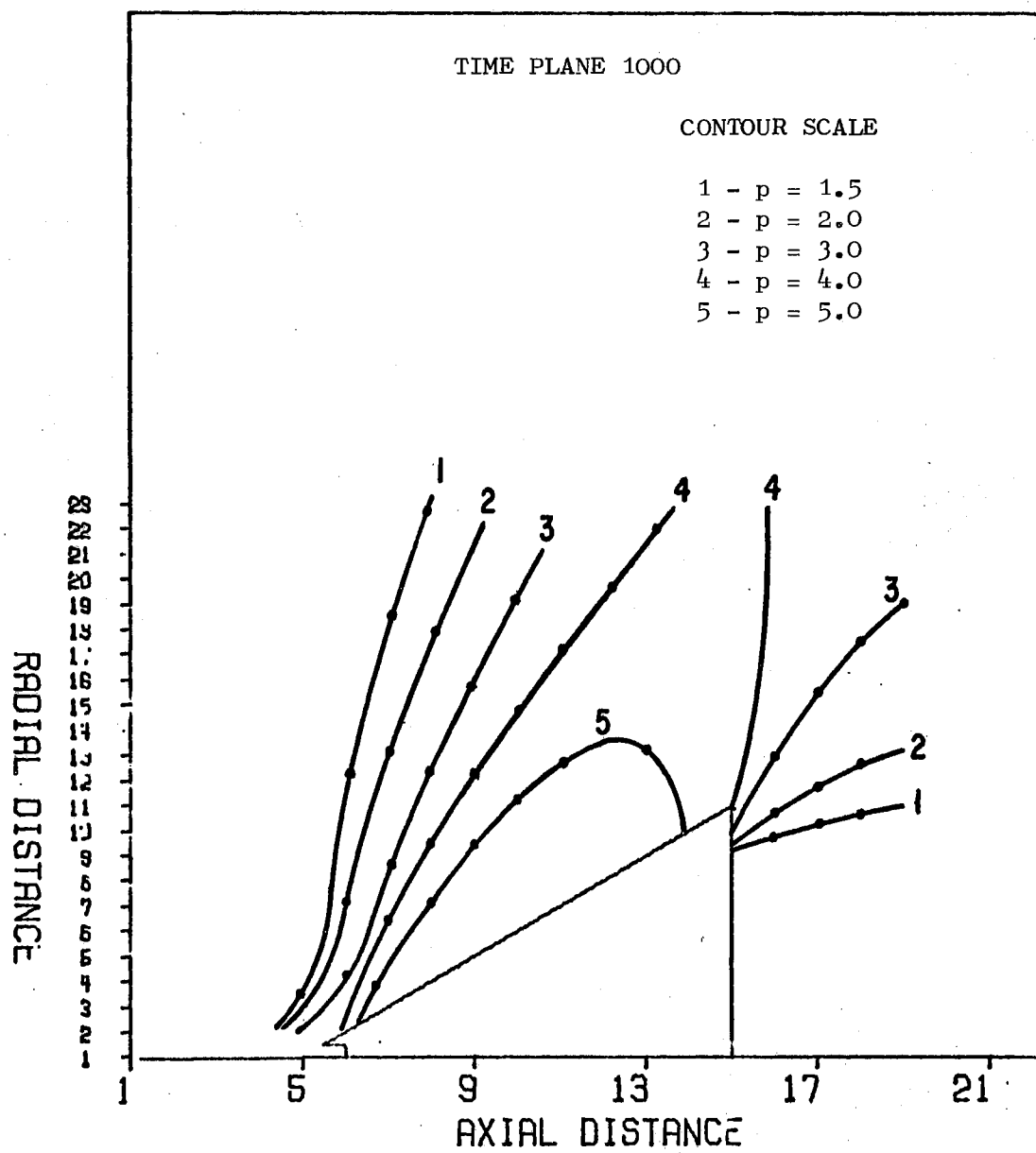


Figure 40. Pressure Profiles, $M_\infty = 3.0$, $\alpha = 20^\circ$, $\theta = 90^\circ$

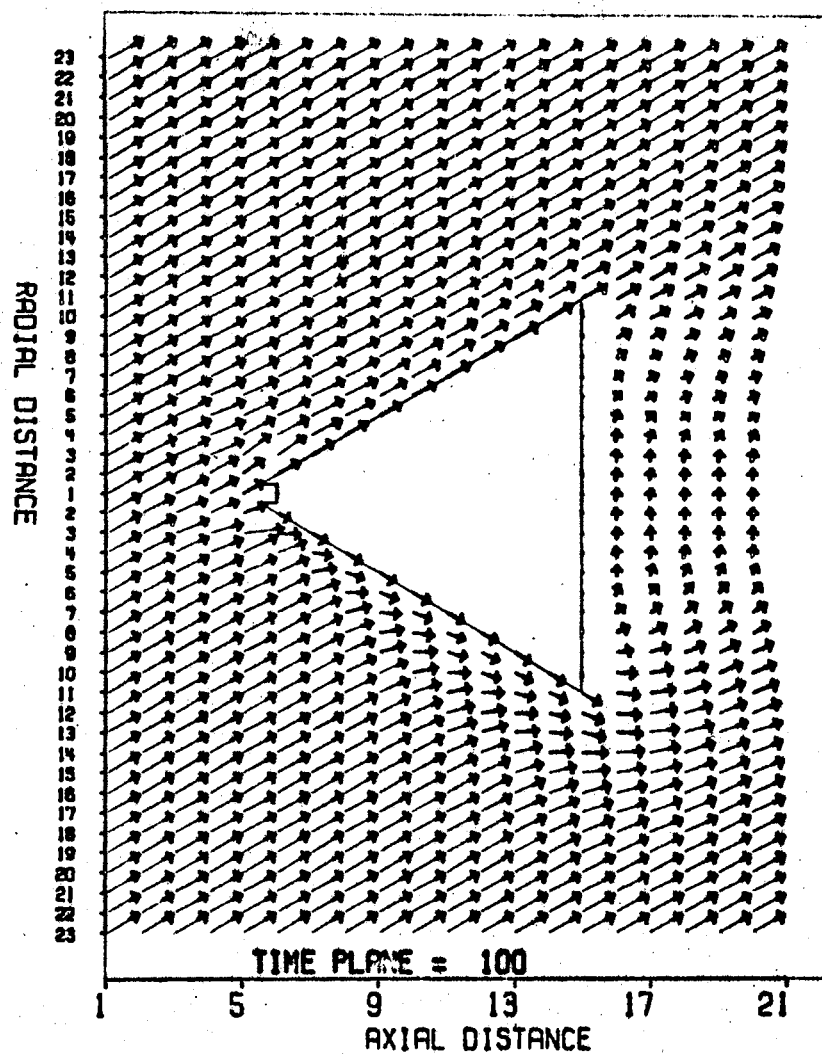


Figure 41. Windward/Leeward Velocity Vector Map,
 $M_{\infty} = 3.0$, $\alpha = 30^{\circ}$

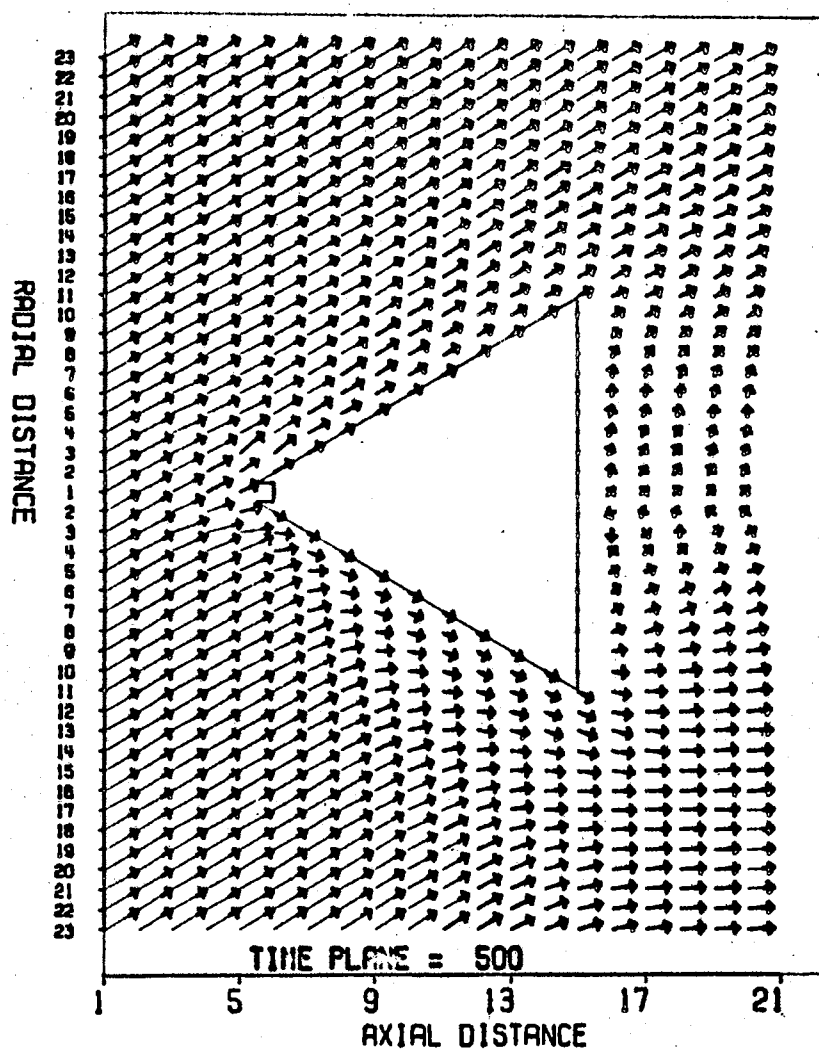


Figure 42. Windward/Leeward Velocity Vector Map,
 $M_{\infty} = 3.0$, $\alpha = 30^{\circ}$

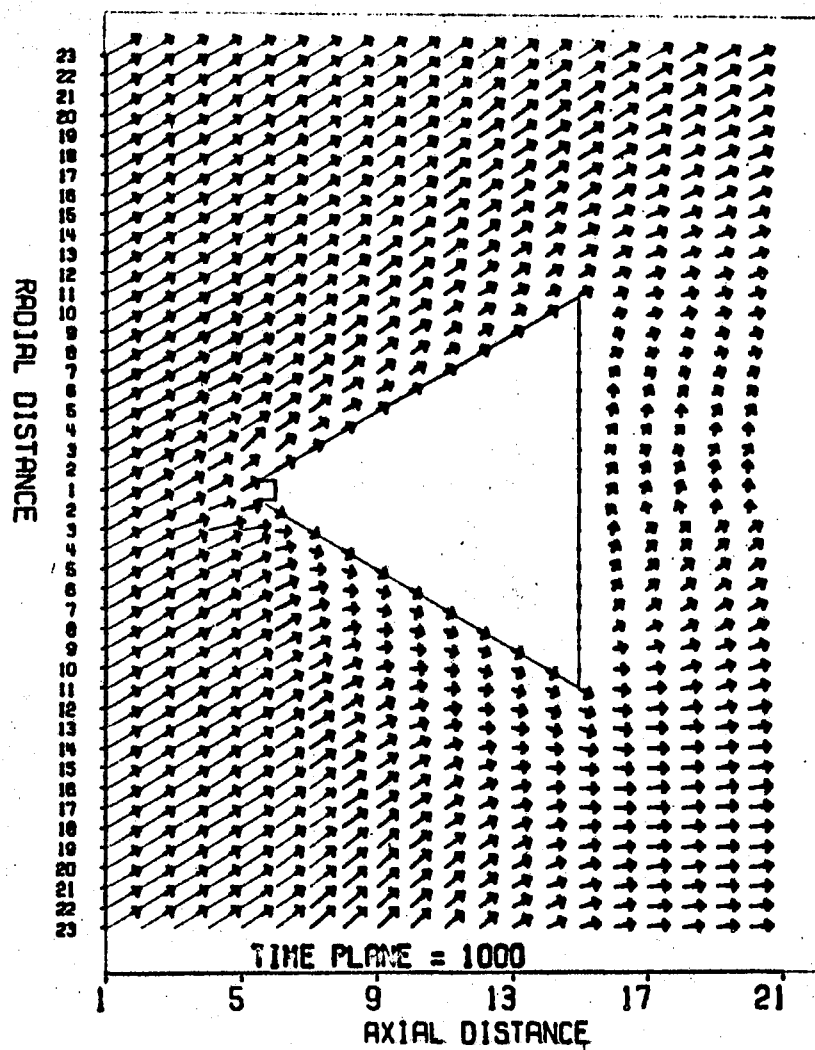


Figure 43. Windward/Leeward Velocity Vector Map,
 $M_{\infty} = 3.0$, $\alpha = 30^{\circ}$

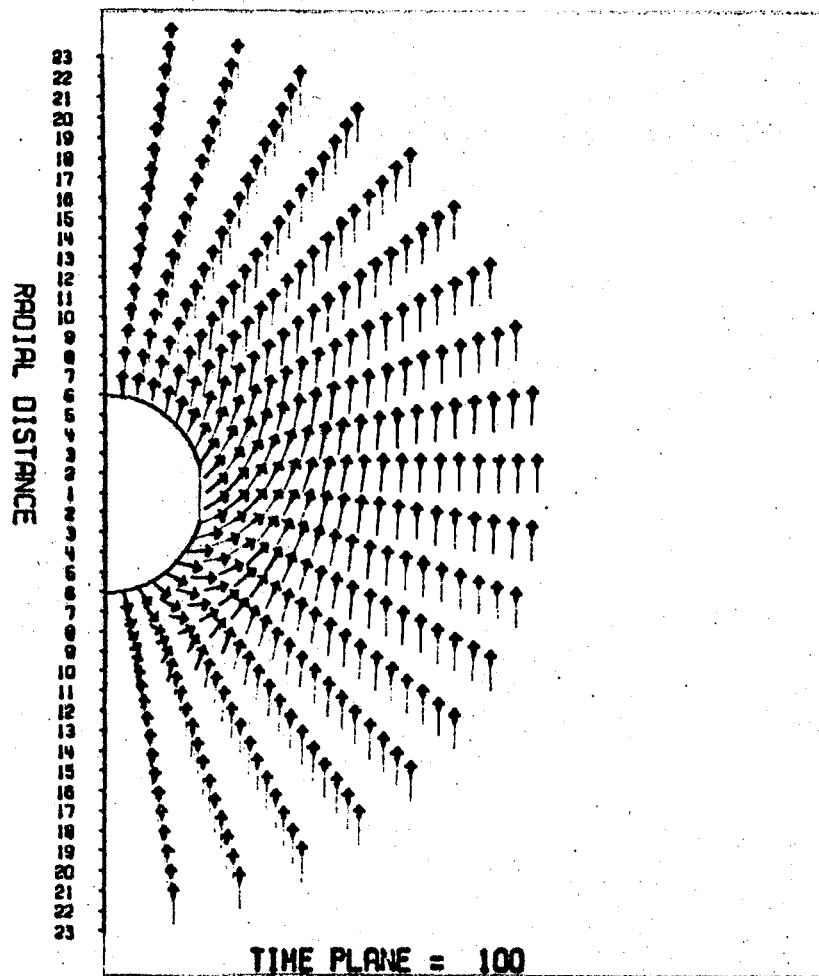


Figure 44. Transverse Velocity Vector Map,
 $M = 3.0$, $\alpha = 30^\circ$, $m = 10$
 (Midway on Cone Axis)

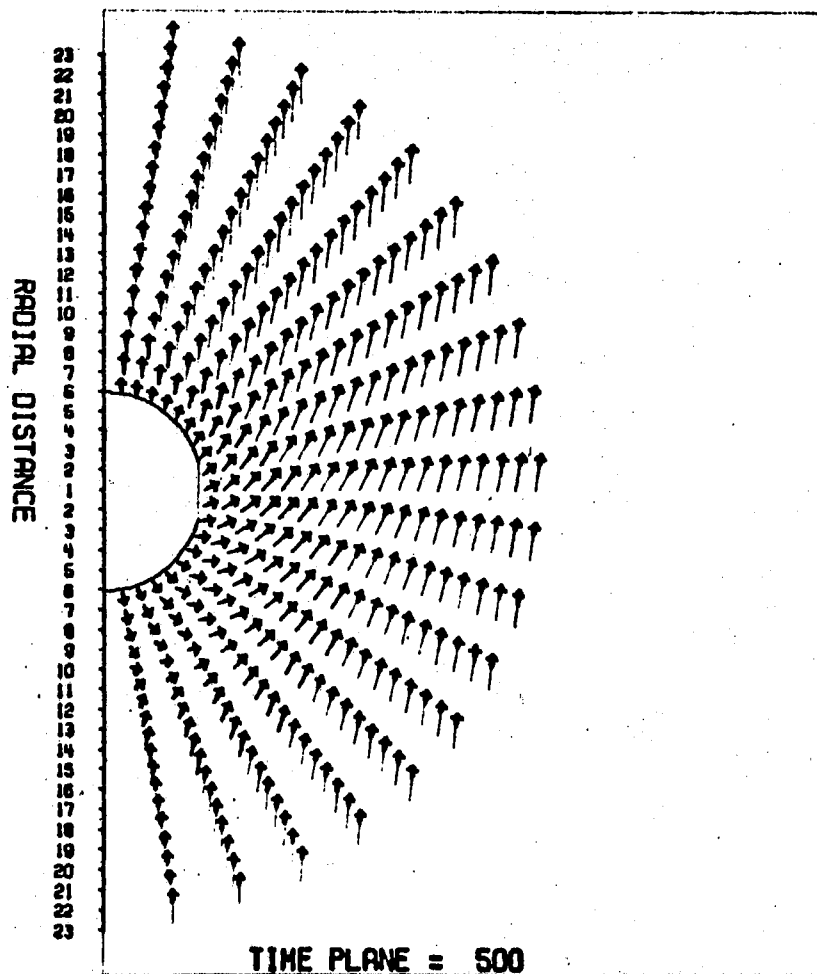


Figure 45. Transverse Velocity Vector Map,
 $M = 3.0$, $\alpha = 30^\circ$, $m = 10$
 (Midway on Cone Axis)

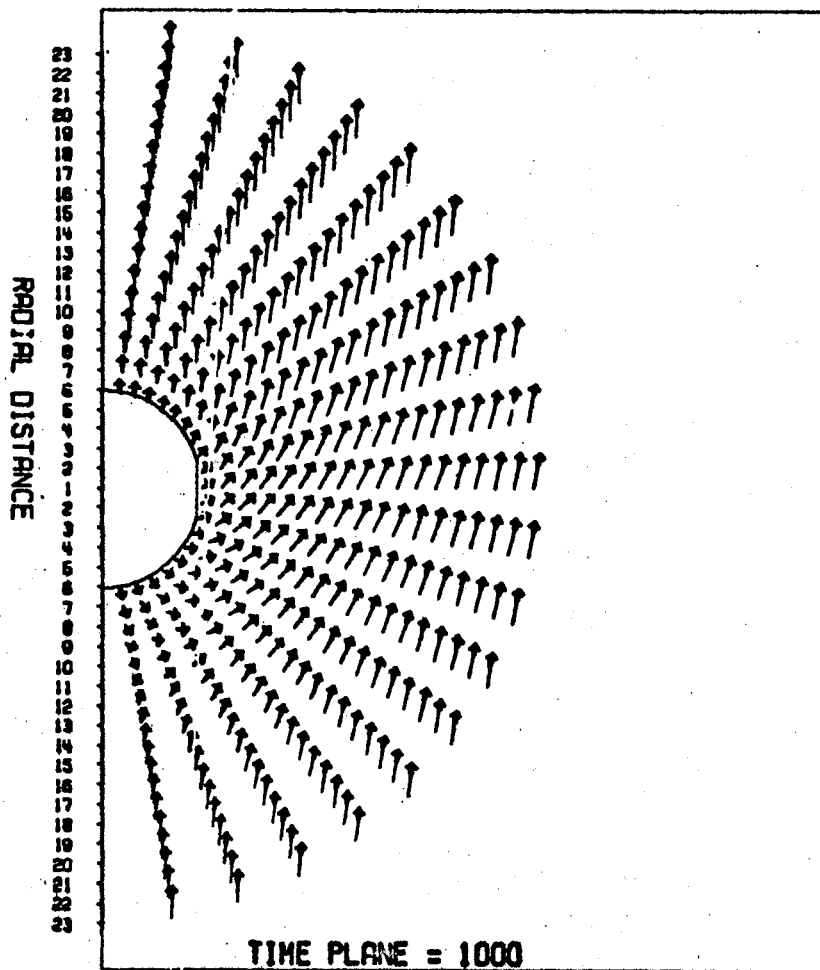


Figure 46. Transverse Velocity Vector Map,
 $M = 3.0$, $\alpha = 30^\circ$, $m = 10$
 (Midway on Cone Axis)

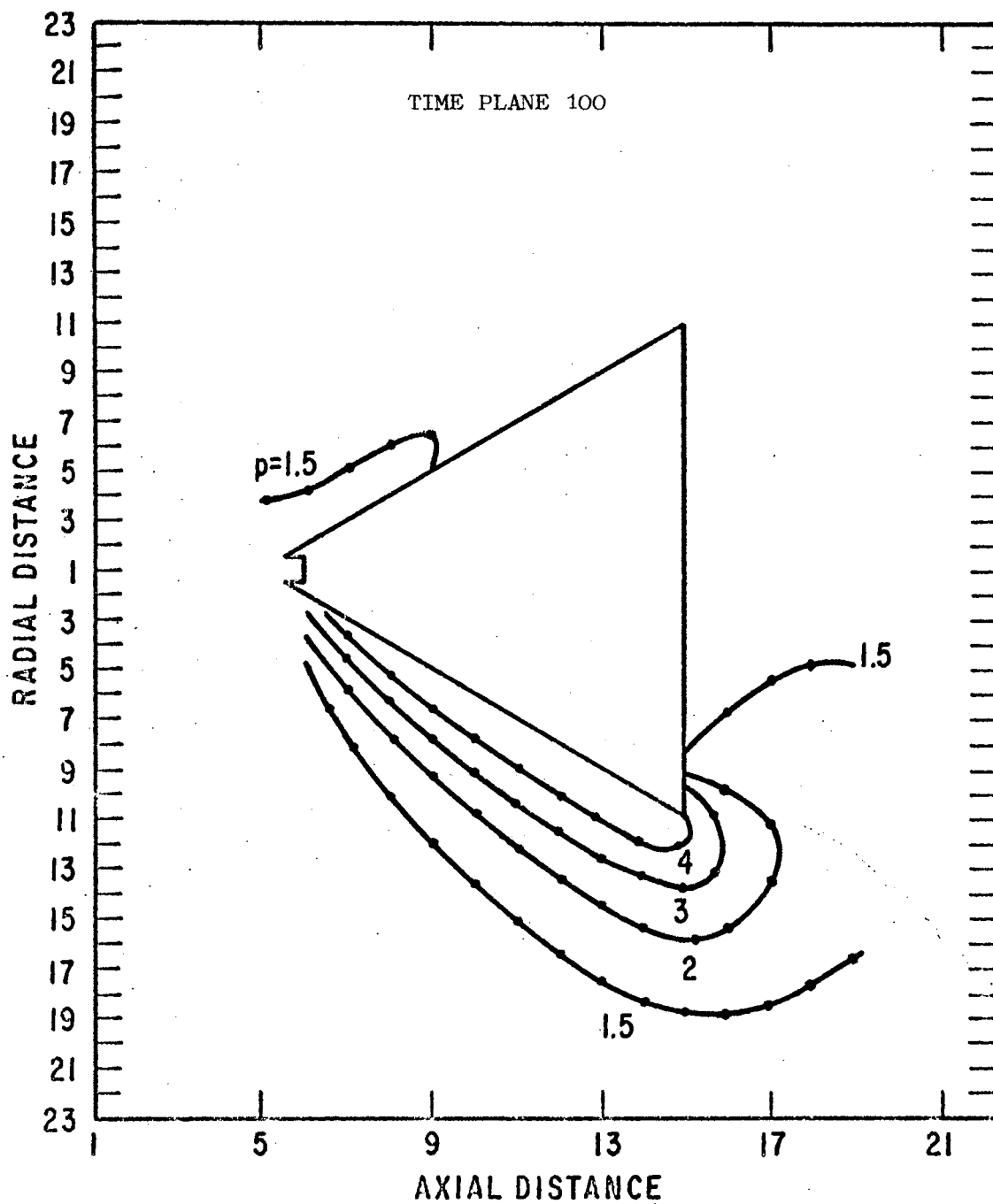


Figure 47. Pressure Profiles, $M_\infty = 3.0$, $\alpha = 30^\circ$, $\theta = 0^\circ, 180^\circ$

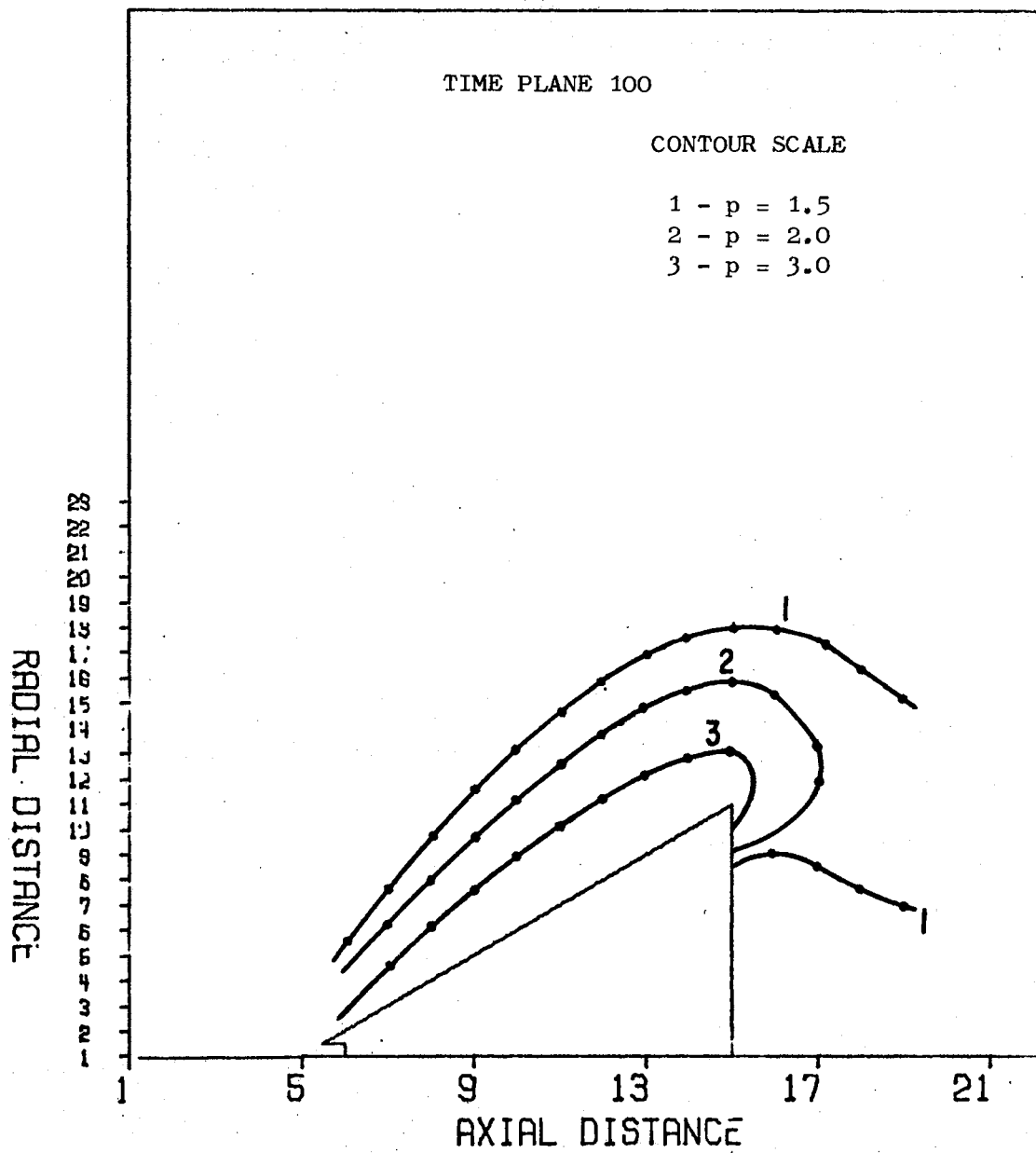


Figure 48. Pressure Profiles, $M_\infty = 3.0$, $\alpha = 30^\circ$, $\theta = 90^\circ$

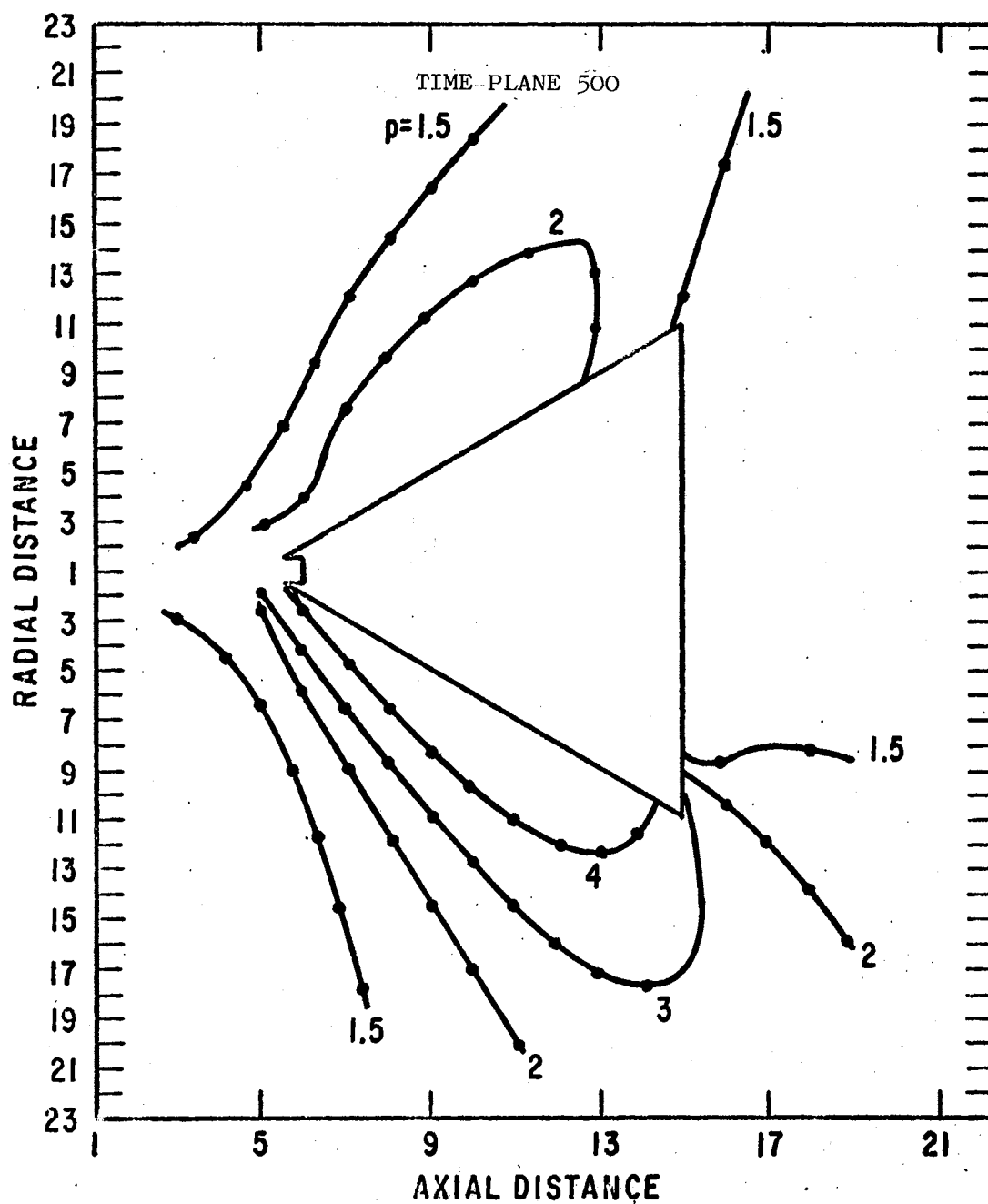


Figure 49. Pressure Profiles, $M_{\infty} = 3.0$, $\alpha = 30^\circ$, $\theta = 0^\circ, 180^\circ$

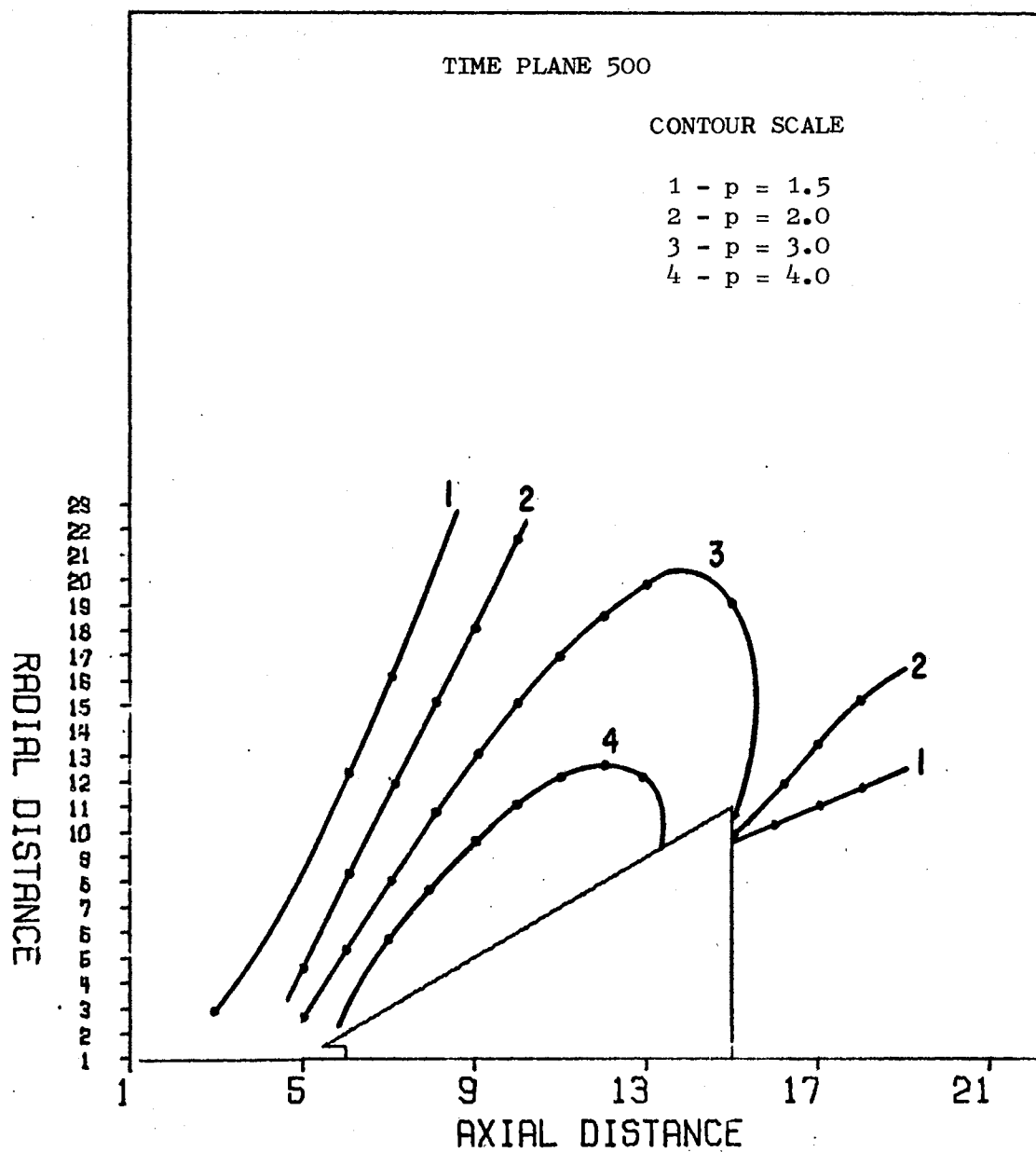


Figure 50. Pressure Profiles, $M_\infty = 3.0$, $\alpha = 30^\circ$, $\theta = 90^\circ$

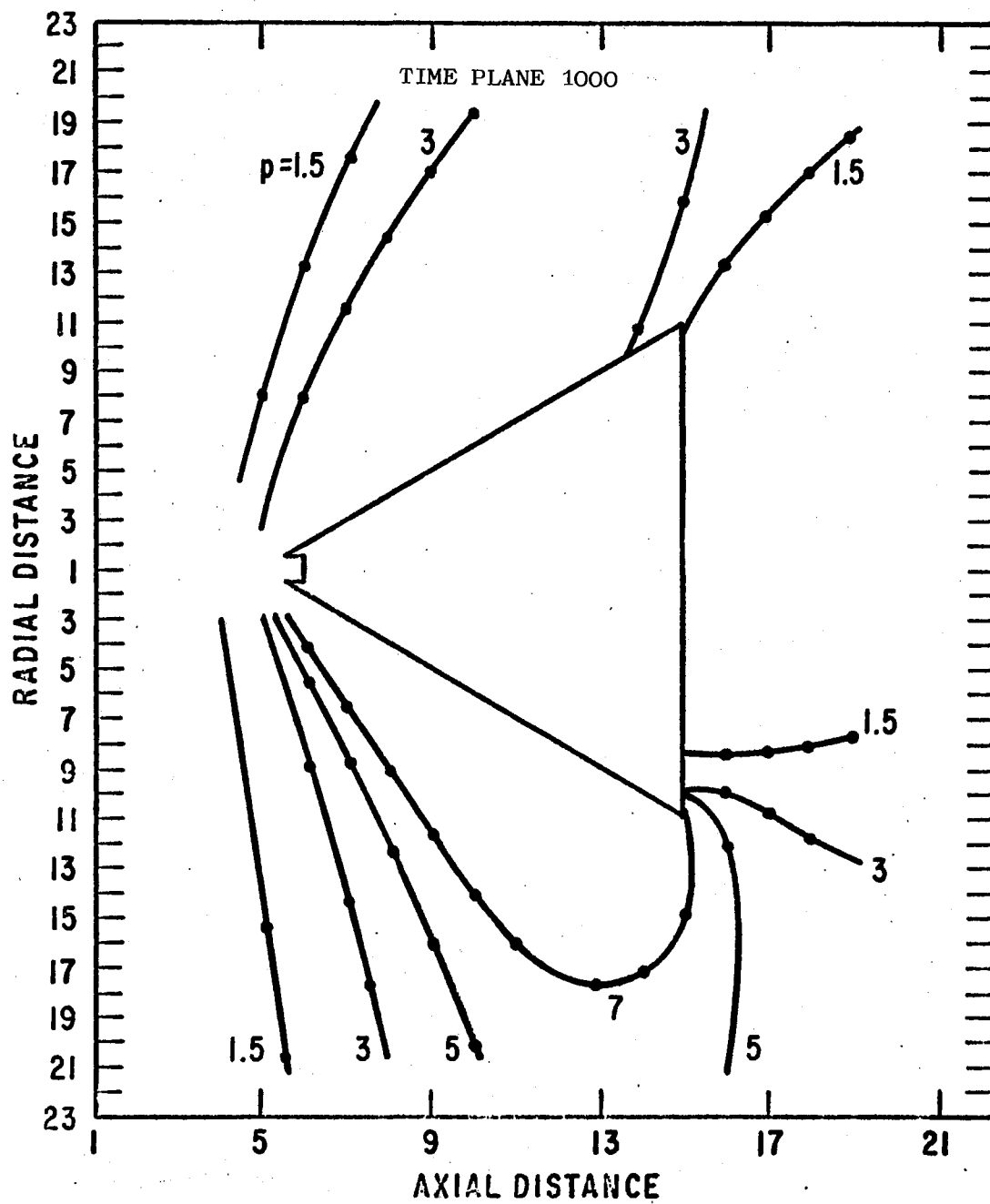


Figure 51. Pressure Profiles, $M_\infty = 3.0$, $\alpha = 30^\circ$, $\theta = 0^\circ, 180^\circ$

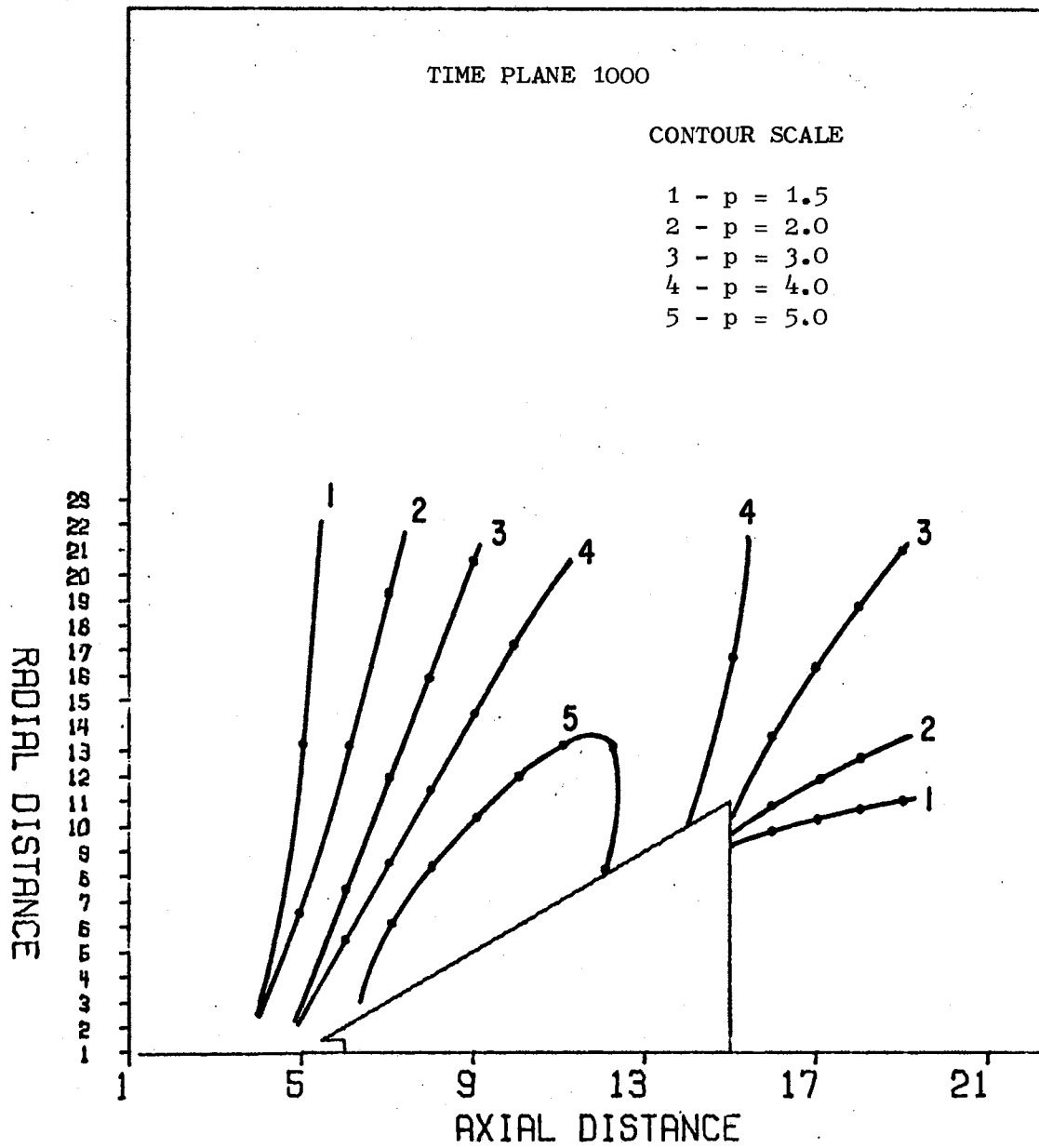


Figure 52. Pressure Profiles, $M_\infty = 3.0$, $\alpha = 30^\circ$, $\theta = 90^\circ$

CHAPTER VI

COMPARISON OF RESULTS WITH THEORY AND EXPERIMENT

The results of this study are compared with the sharp-nosed cone results of Jones (17) and Mosely (22). Because the body in this study is a blunted cone, it is expected that the stagnation point pressures of this study will be low in comparison; while the cone surface pressures will be higher than those of the reports chosen for comparison.

Stagnation Point Pressures

The stagnation point pressure calculated in this study was consistently low, despite efforts to alleviate the problem by altering the cone apex shape. A summary comparison is shown in Table II. For a zero angle of attack, the calculated stagnation point pressure is of the order of 20 per cent low; while for a 20° angle of attack, the stagnation pressure is low by 25 per cent when compared to pointed nose theory.

TABLE II
COMPARISON OF STAGNATION POINT PRESSURES

Angle of Attack (degrees)	Results of This Study	Ref. 17 (theory)
0	9.60	11.84
20	8.14	10.96

Cone Surface Pressure Distribution

The distribution of surface pressure as the cone is traversed from apex to base is shown in Figures 53 through 55 as a function of angle of attack. For nonzero angles of attack both leeward and windward surface pressure distributions are shown. The zero angle of attack comparison shows the results of this study to be in error on the high side when compared to pointed nose theory. The nose and base regions are discounted since both nose and base exert considerable influence on the surface. The discrepancy in this case is less than 20 per cent for all cone distances. Even less discrepancy exists between the results of this study and experimental data. For an angle of attack of 10° , the differences between the results calculated here and those of reference (17) are much more pronounced (see Figure 54). Even discounting the "bulge" at about 25 per cent of the cone surface the percentage difference on the lee side was of the order of 66 per cent, and on the windward side 20 per cent. For a 20° angle of attack, the difference between the results of this study and those of reference (17) are of the order of 100 per cent or less on the lee side, while on the windward side the percentage difference is only about six per cent, less at selected stations.

In summary, the surface pressure distributions agree with the theory to a varying degree, depending on the angle of attack and whether one considers the windward or leeward side. Discrepancies are consistently larger on the lee side. For all angles of attack, the proximity of the nose and/or base significantly affected the fore and aft station surface pressures.

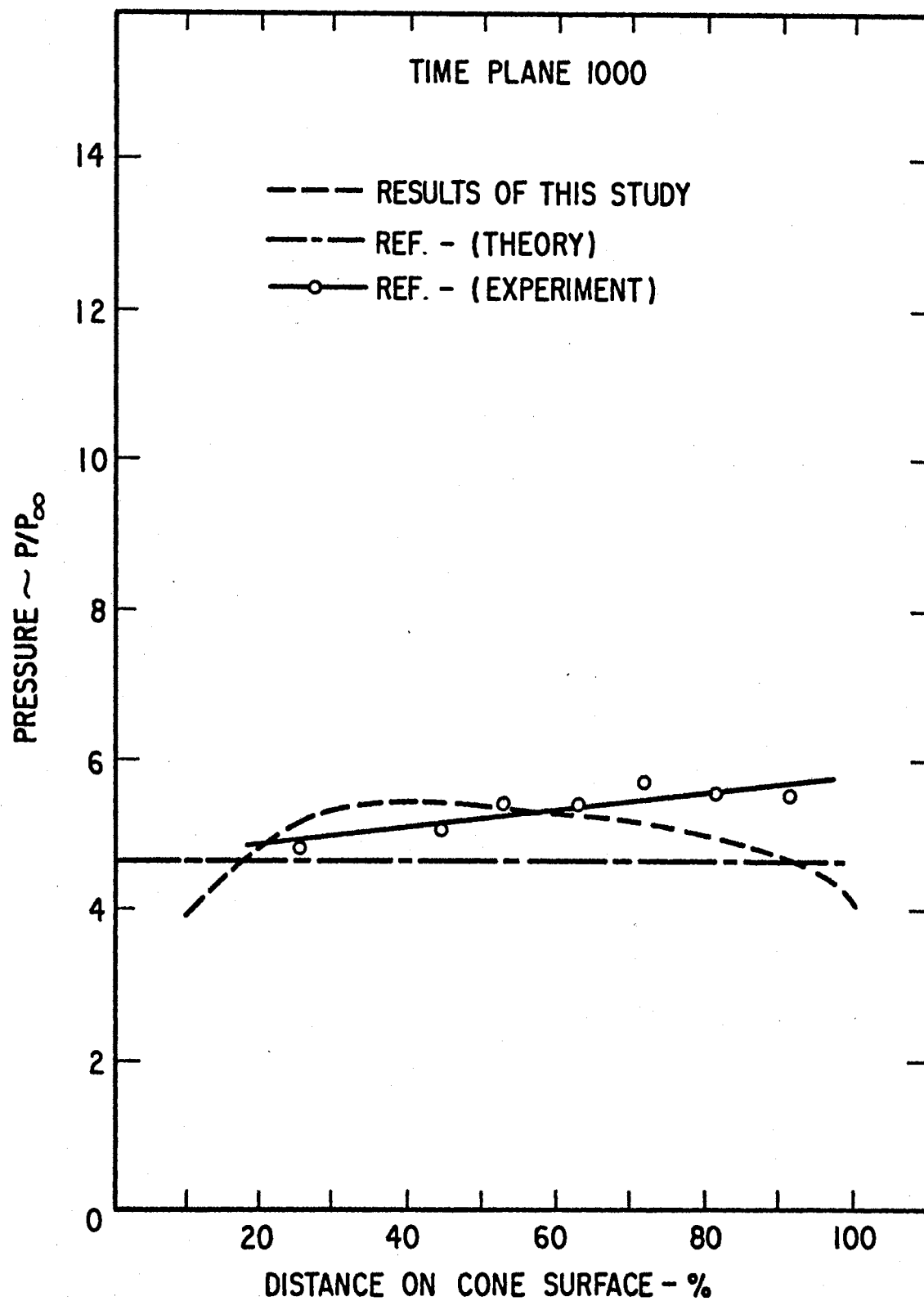


Figure 53. Cone Surface Pressure Distribution, $M_\infty = 3.0$,
 $\alpha = 0^\circ$

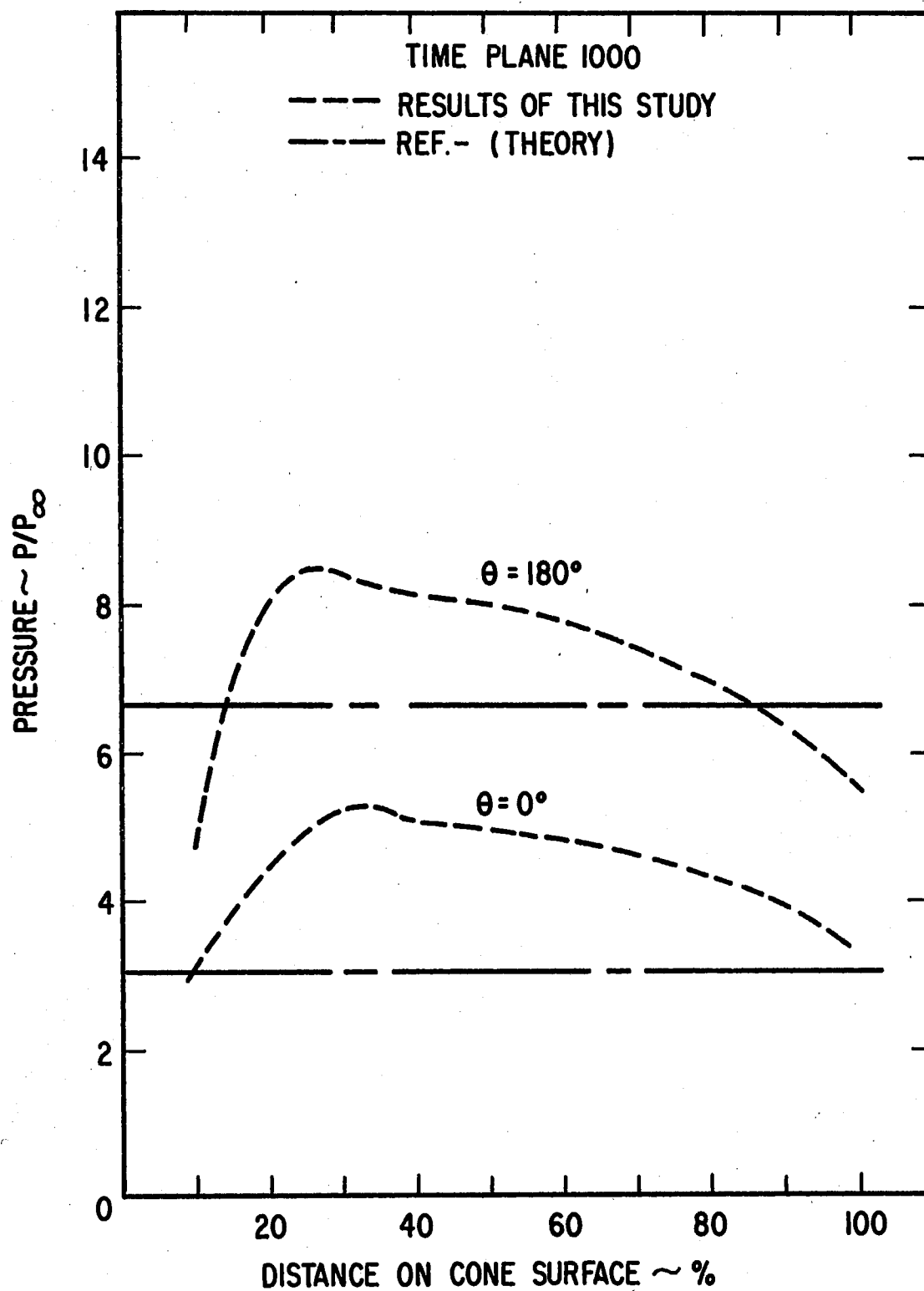


Figure 54. Cone Surface Pressure Distribution,
 Windward/Leeward Plane, $M_\infty = 3.0$,
 $\alpha = 10^\circ$

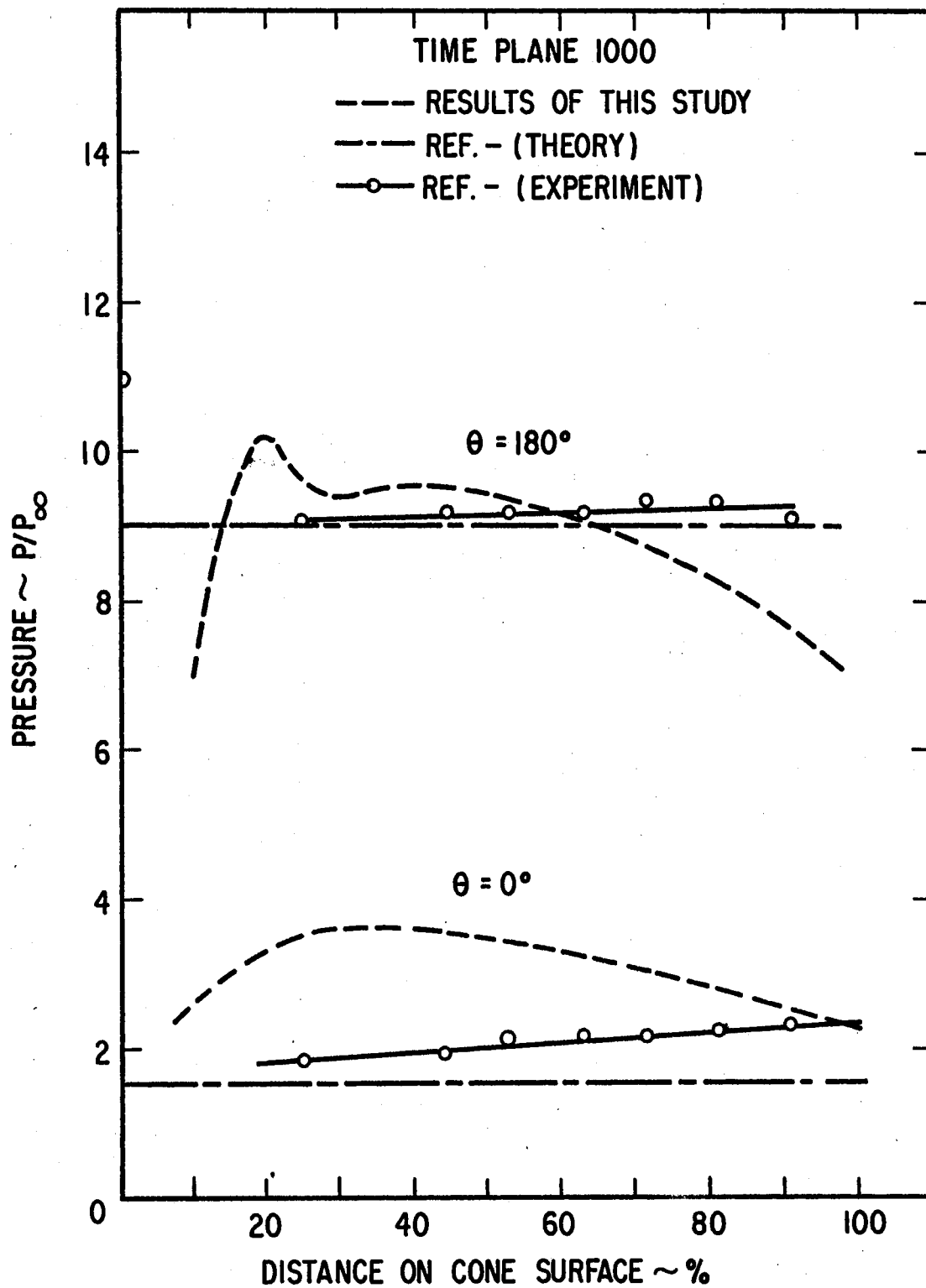


Figure 55. Cone Surface Pressure Distribution,
Windward/Leeward Plane, $M_\infty = 3.0$,
 $\alpha = 20^\circ$

Shock Wave Position and Downstream Pressures

The degree to which the computed flow field duplicates the theoretical results is indicated in Figures 56 and 57. Figure 56 duplicates Figure 16, showing the pressure profiles at time plane 1000 for an angle of attack of 0° . Superimposed on the pressure profiles is the theoretical shock wave position (reference (17)). It can be seen that the pressure profiles quite closely parallel the shock position. The pressure downstream of the shock, again from reference (17) is 4.14. The pressure, as computed in this study, at the same location is just over 4.0 for the major portion of the distance along the cone surface. Figure 57 gives the same data for an angle of attack of 10° for both the leeward and windward planes of flow. For the windward plane the shock wave angle is fairly well matched by the angle of its pressure profiles near the shock position. The pressure profiles indicate a downstream pressure in excess of 7.0; whereas, the theoretical downstream pressure is 5.91. Agreement in the leeward plane is less encouraging. The shock wave angle as given in reference (17) does not appear to coincide at all well with any of the pressure contours shown. The theoretical downstream pressure is 2.68; whereas, the computed results of this study indicate a downstream pressure in excess of 4.0.

Review of the data reveals that both density and pressure are high when compared to other theory, while velocities are low. The above combination suggests that the results of this study are tending to a strong-shock solution. The dependence of error on the angle theta (θ) suggests that the error-inducing influence originates with the technique used to determine the cone surface property values.

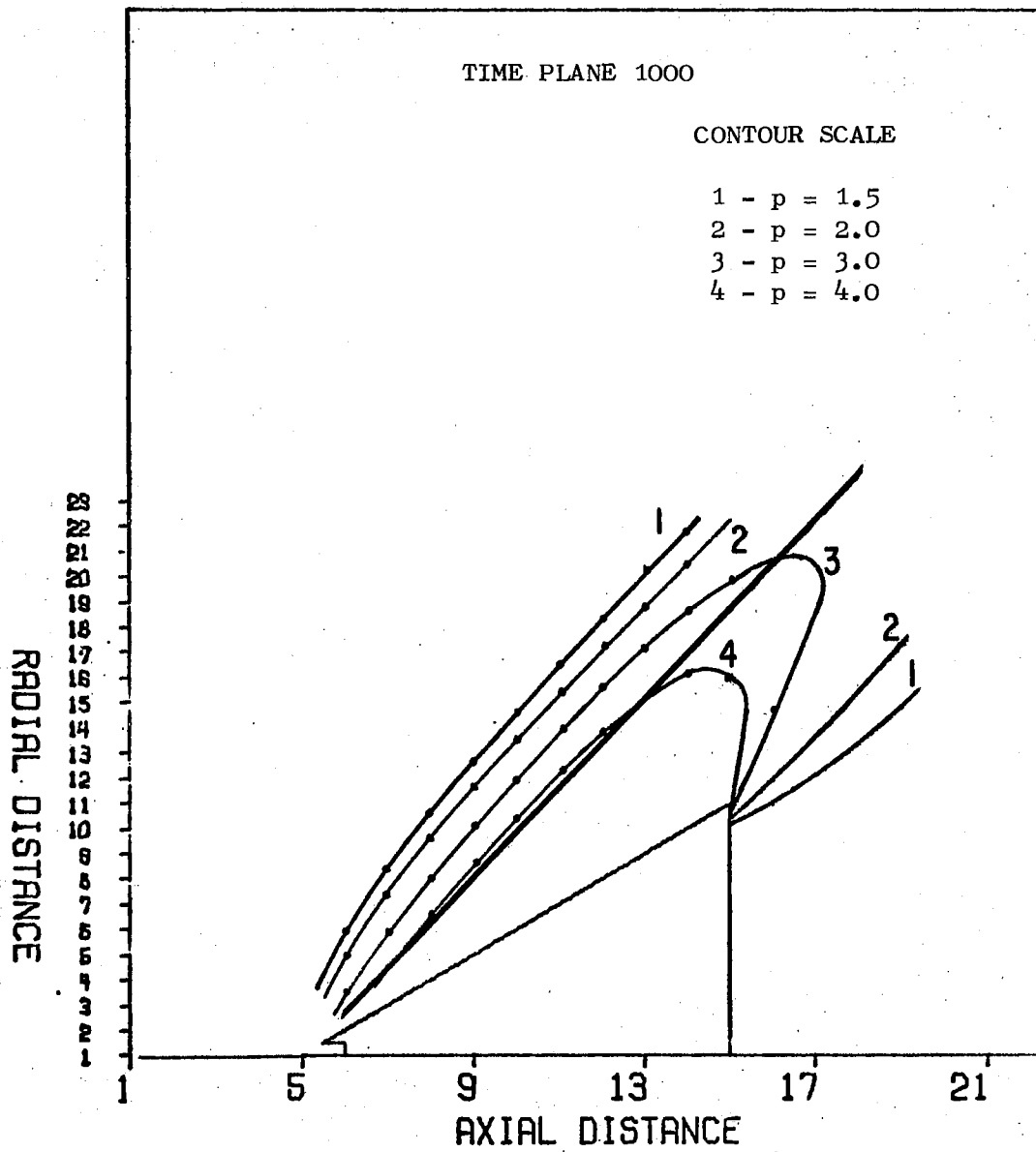


Figure 56. Comparison Between Computed Pressure Profiles and Theoretical Shock Wave Position and Downstream Pressure, $\alpha = 0^\circ$

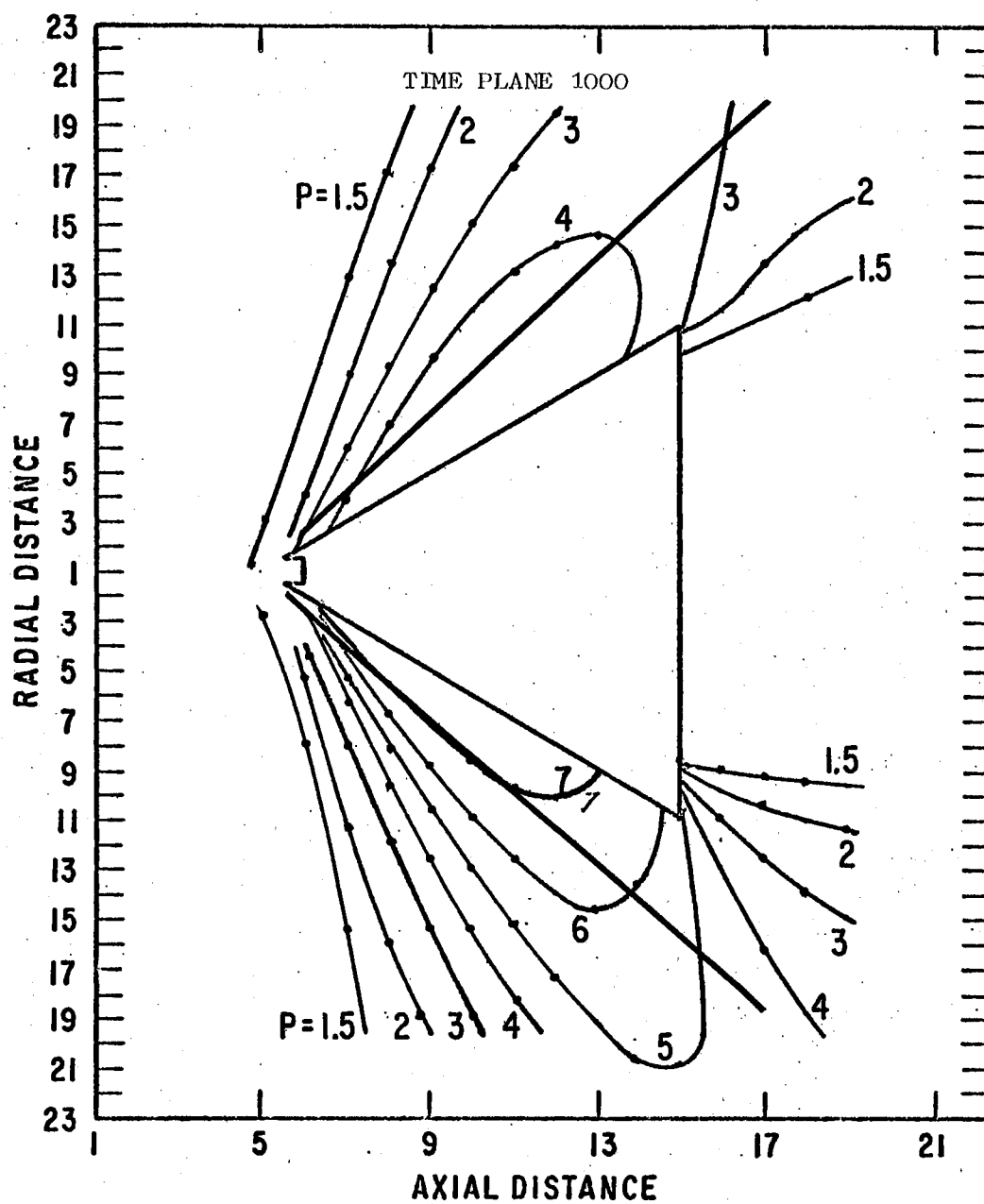


Figure 57. Comparison Between Computed Pressure Profiles and Theoretical Shock Wave Position and Downstream Pressure, $\alpha = 10^\circ$

CHAPTER VII

CONCLUSIONS AND RECOMMENDATIONS

Conclusions

- (1) A numerical technique has been developed for the description of the three-dimensional flow field surrounding a cone in supersonic flight.
- (2) The technique developed in this study is capable of giving reasonable first order approximations to the flow field property values of density, momentum, energy, and pressure for angles of attack up to 10° .
- (3) Certain of the computer output formats available as a result of this study can be useful tools for classroom type flow-visualization purposes.
- (4) The accuracy the computer code used to generate flow solutions appears to be currently limited by the accuracy of the method of determining the cone surface property values. Errors in the current study vary upwards from six per cent for cone surface pressures, depending on the angle of attack and the angle of rotation away from the windward plane.
- (5) High angle of attack solutions should not be generated with the computer code in its present form if the desired output is required to be highly accurate.

Recommendations

- (1) It is recommended that a spherical coordinate system be considered for the determination of cone surface property values. The representation of terms in neighboring theta (θ) planes which contribute strongly to crossflow calculations could be handled more accurately and more easily with spherical coordinates.
- (2) The flow field should be extended downstream a sufficient distance to allow for the full development of the wake.

A SELECTED BIBLIOGRAPHY

- (1) Abbett, Michael. "Inverse Computation of Supersonic Inviscid Flow Fields with Imbedded Shocks: Analysis and Users Manual," General Applied Science Laboratories (November, 1966), AD 655806.
- (2) Abbett, Michael. "Inverse Computation of Supersonic Inviscid Flow Fields with Imbedded Shocks," (addendum to TM #156) General Applied Science Laboratories (December, 1967), AD 664938.
- (3) Ames Research Staff, "Equations, Tables, and Charts for Compressible Flow," NACA 1135 (1953).
- (4) Babenko, K. I., et al. "Three-Dimensional Flow of Ideal Gas Past Smooth Bodies," NASA TTF-380 (April, 1966).
- (5) Benokraitis, Vitalius. "The Numerical Solution of the Eulerian Hydrodynamic Equations on Illiac IV," Dept. of Computer Science, University of Illinois (May, 1968), PB 180032.
- (6) Bird, R. B., W. E. Stewart, and E. N. Lightfoot. Transport Phenomena. New York: John Wiley & Sons, 1960.
- (7) Bohachevsky, Ihor O., Ephraim L. Rubin, and Robert Mates. "A Direct Method for Computation of Nonequilibrium Flows with Detached Shock Waves," American Institute of Aeronautics and Astronautics paper 65-24 (January, 1965).
- (8) Brainerd, Jerome J. "Numerical Analysis of a Method for Calculating Three-Dimensional Supersonic Flow Fields," University of Alabama Research Institute (August, 1967), AD 662775.
- (9) Calder, Kenneth L., "Concerning Similarity Analysis Based on the Use of Governing Equations and Boundary Conditions and Longs Method of Generalized Dimensional Analysis," Dept. of the Army (November, 1967), AD 664205.
- (10) Campbell, James F., and Dorothy T. Howell. "Supersonic Aerodynamics of Large Angle Cones," NASA TN D-4719 (August, 1968).
- (11) Chu, C. K. (Editor) "Computational Fluid Dynamics." American Institute of Aeronautics and Astronautics selected reprints, Vol. IV (July, 1968).

- (12) Damkevala, Rusi Jal. "A Technique for Studying Interactions Between a Supersonic Body and Blast Waves Approaching Obliquely." (Unpublished Ph.D. thesis, Oklahoma State University, May, 1967.)
- (13) Eaton, Roger R. "A Numerical Solution for the Flow Field of a Supersonic Cone Cylinder Entering and Leaving a Blast Sphere Diametrically." (Unpublished Ph.D. thesis, Oklahoma State University, May, 1967.)
- (14) Foster, A. D. "A Compilation of Longitudinal Aerodynamic Characteristics Including Pressure Information for Sharp and Blunt-Nosed Cones Having Flat and Modified Bases," Sandia Corp. monograph, SC-R-64-1311 (January, 1965).
- (15) Jackomis, W. N. "Transient Flow Field Analysis of a Plane Blast Wave Intercepting a Stationary Cone at Zero Angle of Attack." (Ph.D. Dissertation, Oklahoma State University, May, 1965; published as Eng. Res. Rpt. SBW-9 by Jackomis, W. N., and Zumwalt, G. W., August, 1965.)
- (16) Jenkins, Billy Z. "A Survey and Introduction to the Use of Finite Difference Methods in Fluid Dynamical Problems." U. S. Army Missile Command (March, 1968), AD 831438.
- (17) Jones, D. J. "Tables of Inviscid Supersonic Flow About Circular Cones at Incidence." North Atlantic Treaty Organization, Paris (1969), (AGARDograph 137).
- (18) Katskova, O. N., et al. "Numerical Calculations of a Supersonic Flow Past Ducted Bodies at an Angle of Attack." John Hopkins University (14 June 1968), AD 675338.
- (19) Lane, F., E. Lieberman, and H. Fox. "Analysis and Users Manual for Implicit Finite-Difference Computer Program for Laminar Compressible Boundary Layer Calculations," General Applied Science Laboratories TR No. 629 (November, 1966), AD 665681.
- (20) Moretti, Gino, and Gary Bleich. "Three-Dimensional Flow Around Blunt Bodies." American Institute of Aeronautics and Astronautics paper 67-222 (January, 1967).
- (21) Moretti, Gino, and Ricardo Bastianon. "Three-Dimensional Effects in Intakes and Nozzles," American Institute of Aeronautics and Astronautics paper 67-224 (January, 1967).
- (22) Mosely, W. C., Jr., and B. J. Wells. "Wind Tunnel Investigation of the Aerodynamic Pressure on the Apollo Command Module Configuration." NASA TN D-5514 (October, 1969).
- (23) Petri, Fred. "The Addition of Secondary Shock Capability and Modifications to the GASL Three-Dimensional Characteristics Program--Part I - Analysis and Results." U. S. Army Missile Command (August, 1967), AD 659808.

- (24) Petri, Fred. "Real Gas Effects in a Time Dependent Blunt Body Program and Cone at an Angle of Attack Program," General Applied Science Laboratories, U. S. Army Missile Command (August, 1967), AD 659809.
- (25) Rubin, Ephraim L., and Stanley Preiser. "On This Derivation of Three-Dimensional Second Order Accurate Hydrodynamic Difference Schemes," Polytechnic Institute of Brooklyn, PIBAL Report No. 68-24 (July, 1968), AD 676317.
- (26) Rusanov, V. V. "The Calculation of the Interaction of Non-Stationary Shock Waves and Obstacles." National Research Council of Canada Library, Ottawa, Canada, Tech. Translation 1027 by D. A. Sinclair, 1962. Translated from: Zhurnal Vychislitelnoi Fiziki, Akademiya Nauk, SSSR 1, Vol. 1, No. 2 (1961), pp. 267-279.
- (27) Rusanov, V. V. "Three-Dimensional Supersonic Flow Over a Blunt Body." Joint Publications Research Service (Department of Commerce) JPRS 47180 (6 January 1969).
- (28) Sims, Joseph L. "Supersonic Flow Around Right Circular Cones-Tables for Zero Angle of Attack." Army Ballistic Missile Agency, Rpt. No. DATR-11-60 (April, 1960), AD 234736.
- (29) Sims, Joseph L. "Supersonic Flow Around Right Circular Cones-Tables for Small Angle of Attack." Army Ballistic Missile Agency, Rpt. No. DATR-19-60 (April, 1960), AD 239029.
- (30) Tyler, L. D. "Numerical Solutions of the Flow Field Produced by a Plane Shock Wave Emerging into a Crossflow." (Ph.D. Dissertation, Oklahoma State University, May, 1965; published as Eng. Res. Rpt. SBW-10, by Tyler, L. D., and Zumwalt, G. W., 1965.)
- (31) Walker, W. F., and L. D. Tyler. "Literature Survey on Shock Wave Interactions with Shocks and Bodies," Oklahoma State University Rpt. SWB-7 (October, 1964).
- (32) Walker, W. F. "A Numerical Solution for the Interaction of a Moving Shock Wave with a Turbulent Mixing Region." (Unpublished Ph.D. Dissertation, Oklahoma State University, May, 1966.)
- (33) Weilerstein, G., E. Sanlorenzo, and F. Petri. "Programs for the Analyses of Flow Fields Around Spherically Capped Three-Dimensional Bodies at Angles of Attack." General Applied Science Laboratories TR #462 (October, 1964), AD 818354, 818353, 818247, (In 3 parts).
- (34) Von Neumann, J., and R. D. Richtmyer. "A Method for the Numerical Calculation of Hydrodynamic Shocks," J. Appl. Physics, Vol. 21 (1950), p. 232.

- (35) Xerikos, J., and W. A. Anderson. "A Time-Dependent Approach to the Numerical Solution of the Flow Field About an Axisymmetric Vehicle at an Angle of Attack." Douglas Aircraft Corporation, Santa Monica, N68-36114 (June, 1968).
- (36) Zumwalt, Glen W. "Studies in Time-Dependent, Eulerian, Explicit Numerical Fluid Mechanics." Unpublished Notes.

VITA³

John Joseph Prentice

Candidate for the Degree of

Doctor of Philosophy

Thesis: A NUMERICAL SOLUTION FOR THE FLOW FIELD SURROUNDING A
SUPERSONIC CONE AT AN ANGLE OF ATTACK

Major Field: Engineering

Biographical:

Personal Data: Born in St. Paul, Minnesota, January 2, 1934,
the son of John and Anna Krueger Prentice.

Education: Attended grade school in Minneapolis and Edina,
Minnesota; graduated from Edina-Morningside High School,
Edina, Minnesota in 1951; received the Bachelor of Aeronauti-
cal Engineering degree from the University of Minnesota in
June, 1956; received the Master of Science degree from the
Air Force Institute of Technology, with a major in Propulsion,
in August, 1961; completed the requirements for the Doctor
of Philosophy, with a major in Mechanical and Aerospace
Engineering, May, 1971.

Experience: Junior flight test engineer for Lockheed Aircraft
Corporation, Burbank, California from June to December 1956;
Project Officer for aerial flight test and environmental test
of conventional bombs and fuzes at Eglin AFB, Florida from
December, 1956 to January, 1959; Project Officer and Ordnance
Officer for the Blue Scout and Titan III missile systems at
Cape Kennedy, Florida from August, 1961 to August, 1964;
Assistant Professor of Ordnance (Analog Computers) at the
U. S. Military Academy, West Point, New York, from August,
1966 to July, 1969; Project Officer for Nuclear Survivability/
Vulnerability of Aeronautical Systems at the Air Force
Weapons Laboratory, Kirtland AFB, New York from July, 1969
to present.

Professional Organizations: Member, American Institute of
Aeronautics and Astronautics.